ISSN 0377-9416

PMAI

www.pmai.in

TRANSACTIONS OF POWDER METALLURGY ASSOCIATION OF INDIA

Vol. 43 No.1, June 2017

Chief Editor - P. Ramakrishnan

ISSN 0377-9416

PMAI

www.pmai.in

Vol. 43 No.1, June 2017

Chief Editor - P. Ramakrishnan

Powder Metallurgy Association of India

Office Bearers

President
Shri N. Gopinath

Vice President
Shri Aniket Gore
Shri Deepak Grover
Prof. Narendra Dhokey
Shri Rajendra Sethiya

General Secretary
Dr. Deep Prakash

Treasurer
Dr. Murli Gopal Krishnamoorty

Joint Secretary
Shri Sidharth Singhal
Shri Deepak Pattanayak

Price Rs. 500/-

Published by :
Powder Metallurgy Association of India (PMAI)
1002, B-Wing, Kingston, High Street, Hiranandani Complex, Powai, Mumbai - 4000076.
Tel. : +9122 25704588
E-mail : info@pmai.in

Editorial

PM-17, the International Conference on powder metallurgy and particulate materials & Exhibition and the 43rd Annual Technical meeting of PMAI was held at Hotel Pride Plaza, Aerocity, New Delhi during Feb. 2017. Trans. PMAI. Vol.43(1), 2017 features some of the selected papers from this successful event. The Grand Prize for the Best Student paper, an all expenses paid trip to attend the International Conference of APMA 2017 held at Sheriton Hotel of Hsinchu, Tiwan was won by Mr. Manoj Gautam. The details of his trip is reported in PMAI Newsletter, April 2017. A review of PM in Indian industry, opportunities and challenges is the first paper by President Gopinath. This is followed by an article on the dimensional response of standard Fe-Cu-C premixes, a widely used material in PM industry including VVT and the improvements that have been made to control variation. The next paper is on the grain boundary sliding assisted densification during the initial sintering stage of mechanically alloyed Co-Fe-Ni powders. The effect of mechanical alloying on microstructure and mechanical properties of liquid phase sintered Rhenium added Tungsten heavy alloys is discussed in the next article. This is followed by a paper on the investigation of wire-EDM characteristics on CP-Titanium powder metallurgy components using an experimental plan of Box-Behnken design based on Response Surface Methodology approach.

Powder metallurgy processing and properties for magnetic applications in sensors, actuators and motors of automotive including hybrid vehicles are discussed in the next paper. The grand prize winning paper is dealing with the development of a composite electrolyte material for intermediate temperature solid fuel cell. The next award winning paper is on band gap engineering in nano crystalline silicon powder by mechanical alloying which is used in solar, LED and switching applications. Fabrication of thermoelectric generator for high temperature application using unicouples made from p-type and n-type β-iron disilicide which has a potential as the energy source is the next article. This is followed by a paper on the synthesis and characterization of titanium oxycarbide ceramics which is an alternate anode material for intermediate temperature solid oxide fuel cell. The next article is on the effect of pH on synthesis of nano-crystalline magnesium aluminate spinel powder by Sol gel systhesis and the final product is important due to its mechanical properties at elevated temperatures. The final paper is on the investigation of poling parameters of piezoelectric properties of Lead Lanthanum Zirconate Titanate ceramics in order to obtain maximum piezoelectric properties.

P. Ramakrishnan

TRANSACTIONS OF
POWDER METALLURGY ASSOCIATION OF INDIA

Vol. 43 No.1, June 2017

CONTENTS

A REVIEW OF PM IN INDIAN INDUSTRY, OPPORTUNITIES AND CHALLENGES

N. Gopinath

President, Powder Metallurgy Association of India

Introduction:

Industrial growth of any country is linked to its economy, and in this context, it is worthwhile to suggest that the growth of PM market is India may be directly correlated to the size of its economy. A recent study by PWC (Price Waterhouse Cooper) suggests that currently (2016) India is ranked at No. 3 in GDP ranking, following China (#1) and USA (#2). However, the scenario is expected to modify in year 2050, where China would retain its top position whereas India may replace USA for the following position. A growing economy will surely follow more vehicles as well as consumer goods hence the expected growth in PM market.

Presently, India maintains its significant contribution in top vehicle producers in the world, such as:

- It is the largest Tractor manufacturer country.
- 2nd largest Two-wheeler manufacturer
- 2nd largest Bus manufacturer
- 5th largest Heavy Truck manufacturer
- 6th largest Car manufacturer
- 8th largest Commercial Vehicle manufacturer

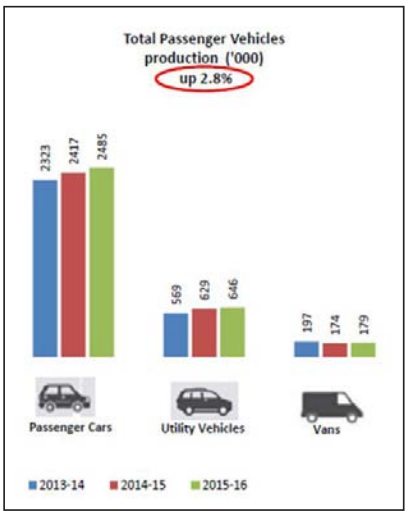

Fig. 1 (a) Vehicle Production in India

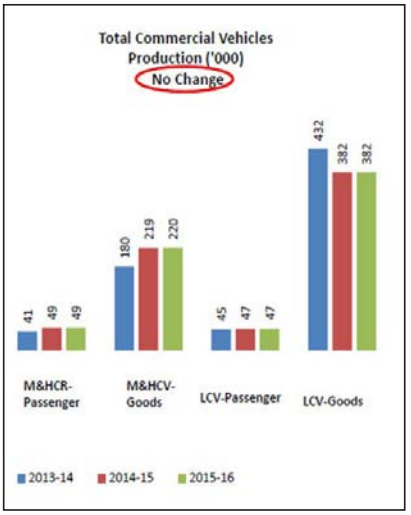

Fig. 1 (b) Vehicle Production in India

Fig. 1 (c) Vehicle Production in India

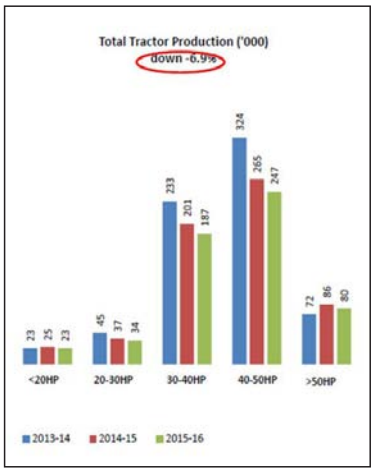

Fig. 1 (d) Vehicle Production in India

Fig.1 (a) – (d) show vehicle production in India from 2013-14 to 2015-16. There has been small increase (2.8%) in the production of total passenger vehicles as well as 2- and 3- wheeler production (1.6%), while no change was found in total commercial vehicles, and there was a moderate decline in the numbers of tractors manufacture. Nonetheless, expected industry patterns depend on various factors, and one very important aspect is large investments in the infrastructure related projects. As shown in Fig.2, in recent past India has attracted investment of more than US $ 850 bn in various sectors. This will surely fuel growth in manufacture of passenger as well as commercial vehicles.

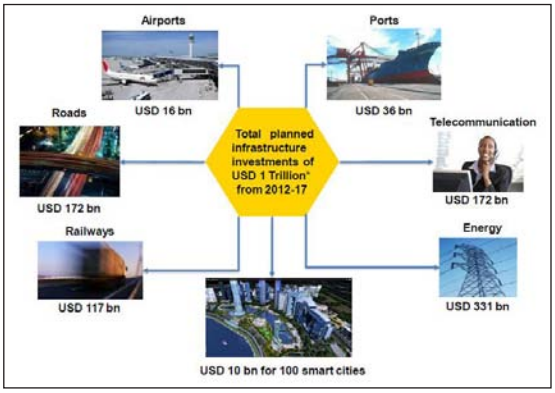

Fig.2: Infrastructure Investment in India

Moreover, most of the infrastructure projects are focused towards the lesser developed part, i.e. Eastern India (East UP, Bihar, Odisha, North Andhra), which in turn means that approximately 1.5 million vehicles may be added. Since automobile sector is a big consumer of PM, it is expected that this will give rise to good growth to the PM industry.

Powder Production:

Table - 1: Metal Powder Production in India

India Data -- All PM applications (estimate)								
	2009	2010	2011	2012	2013	2014	2015	2016
Production Weight:								
Iron-base	26,500t	31,200t	35,400t	37,000t	30,000t	37,000t	30,500t	30,000T
Copper-base	12,500t	13,700t	14,500t	14,500t	13,700t	12,100t	10,000t	6,000T*
Total	39,000t	44,900t	49,900t	51,500t	43,700t	49,100t	40,500t	36,000T

Table-1 shows ferrous and copper-base metal powder production in India from year 2009 – 2016. It may be noted here that non-PM copper-base powder has been excluded in 2016, which is the reason behind lower value. PM components made out of iron-base powders mainly cater to automobile applications (80%), followed by appliances, machinery and bearings, as shown in Fig. 3. Out of this, most of these, approx. 95% were manufactured by small – scale industries. On the other hand, copper – based powder metallurgical parts are used mainly in appliances (60%), followed by friction elements and diamond tools, as depicted in Fig. 4.

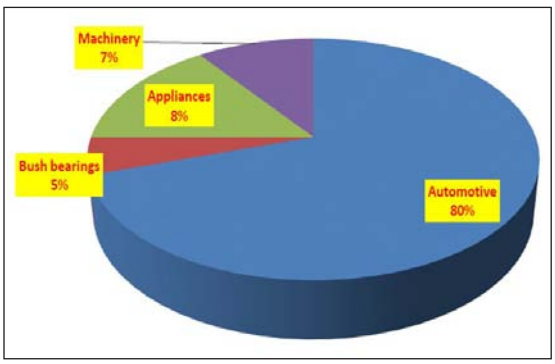

Fig.3: Indian Iron-based market for PM components

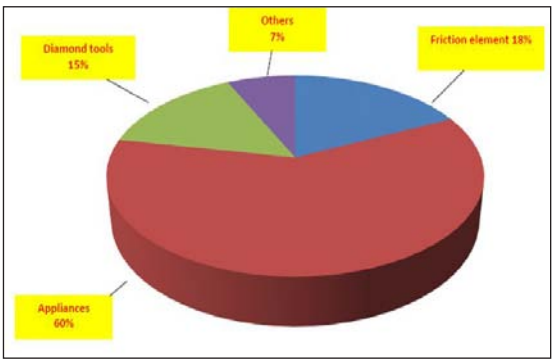

Fig.4: Indian Copper - based market for PM components

Opportunities of Indian PM:

With rising Indian economy and development, as evident from participation in various hi-tech areas such as aerospace and satellite applications, PM parts and their manufacturing is expected to increase significantly. In recent past, launching of record 104 satellites in a single mission is testimony to the prowess of home-grown engineering capability. This is perhaps one of the reasons why various multi-national technology – driven companies viz. Boeing, Bosch, Caterpillar, Cummins, Ford, GE, GM, Honda, Honeywell, Hyundai, Intel, Magna, Mercedes Benz, Microsoft, Renault, Suzuki, Valeo etc. open their R&D centers in India. In addition, environmental concerns have led to adaptation of more stringent vehicle emission norms e.g. Euro-6, Bharat-6 etc. by year 2020. This will also lead to manufacture of various auto parts such as VVT parts, cam lobes, synchro rings etc., as shown in Fig. 5.

Fig.5: Various PM parts for automotive applications

In addition, there has been recent interest in PM components of Al-based materials and composites, due to various process and materials advantages such as high corrosion resistance, lightweight, wear resistance and good thermal properties with high density and precision machinability. Al-based materials find their applications in parts of engine, transmission systems, compressor, hydraulics and electrical systems.

Other emerging areas are 'Metal Injection Molding' (MIM) and 'Additive Manufacturing'. Fig.6 shows some typical parts made by MIM process. In year 2015-16, total shipment of MIM components from India was of the value US $ 125 million out of global US $ 1900 million, which is expected to follow increasing trend. Fig.7 shows some parts manufactured by Additive Manufacturing technique, which is also a very robust fabrication method and finds applications in aerospace, automotive, tooling, medical and dental sectors.

Fig.6: Some PM components manufactured by MIM technique

Fig.7: Some PM components manufactured by AM technique

Challenges to Indian PM:

In spite of various growth opportunities, as mentioned above, Indian PM industry has to face a few challenges, as following:

- High cost of capital equipment and tooling in the face of inadequate initial volumes
- Availability of trained technical manpower for pre-production engineering activities and also to run critical shop floor operations like compaction and sintering
- Low awareness of PM technology and 'Think PM' approach of OEMs

Summary:

In summary, it can be said that due to growing Indian economy, industrial production is expected to get enhanced, which in turn creates various opportunity for Indian PM industry. Besides conventional iron-based and copper-based powders and their components, there is a vast scope to venture into newer areas such as Al-based materials and newer technologies such as MIM and AM.

DIMENSIONAL PRECISION OF Fe-Cu-C PREMIXES

Fran Hanejko and Peter Sokolowski

Hoeganaes Corporation, Cinnaminson, NJ, USA

Abstract : Iron-copper-carbon powder metallurgy steels are the most widely used materials in the PM industry because of their ease of processing, good mechanical properties and relatively low cost. Dimensional precision with these steels is a challenge, however, and is driven by the growth associated with copper. Admixed copper can segregate in the powder mixture and lead to significant variation in part sizes. The use of these steels in components with tight dimensional requirements, including VVTs, has driven powder producers to develop alternative alloying and processing methods to reduce the dimensional variation. This paper outlines the dimensional response of a standard Fe-Cu-C premix and improvements that have been made to control variation.

Keywords - dimensional precision; VVT; Fe-Cu-C

Introduction

Copper steels are the backbone material of the PM industry. They are used in nearly every automotive mega program with their overall usage surpassing other material systems used in powder metallurgy (PM) [1]. This is not to imply that other alloy systems are not important; however, the versatility and cost-effectiveness of iron-copper-carbon steels make them the alloy system of choice for many applications. One potential drawback of the iron-copper-carbon alloy system is the variability of the dimensional control from lot-to-lot and occasionally within lot of premixes. This often requires the need for secondary processing such as sizing or machining to control critical dimensions. A prime example of an automotive component having tight dimensional control is VVT components; they often require holding less than +/- 0.04% DC on the critical pump dimensions [2].

Sintered dimensional change of PM copper steels is influenced by the amount and type of premixed copper, the amount of graphite in the premix, green part density, and sintering conditions. [3, 4] The sintered growth results from the copper melting and subsequent copper diffusion into the iron through both particle and grain boundaries [5]. Figure-1 is a photomicrograph of a ~125 micron copper particle at the onset of copper melting (1083 °C) exhibiting the initial particle and grain boundary wetting. The copper particle shown in Figure-1 results in a non-uniform concentration of copper and relies on diffusion to homogenize the copper distribution. Conventional sintering times and temperatures will not produce a homogeneous copper distribution throughout the microstructure of the iron compact [6]. Increasing graphite additions up to 1% reduce the sintered DC by decreasing solid phase grain boundary diffusion of copper into the iron [7, 8].

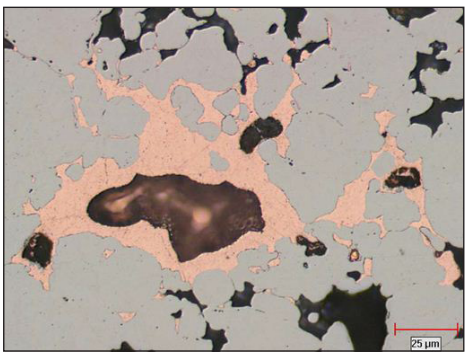

Fig. 1: Copper particle at the onset of melting (1083 °C), [6].

The majority of copper powders used in PM has a -150 micron particle size distribution; thus, when the large copper particles melt, they leave large porosity within the microstructure. It has been suggested that smaller copper particles (-15 microns) are potentially superior because these smaller copper particle sizes minimize / eliminate large pores resulting from copper melting. Shown in Figure 2 is an FC-0208 material that utilized a -15 micron particle size copper. The greater number of copper particles is dispersed uniformly throughout the structure and upon melting will exhibit improved copper homogeneity. Figures 3a and 3b show the resulting sintered pore morphology when using a -150 micron copper powder and a -15 micron copper powder. Assuming a -150 micron particle size has a D50 of ~35 microns, then a 2% addition has approximately 10 million copper particles per 100 grams of a FC-0208 premix. If a -15 micron particle size is used (assuming a D50 of 11 microns) the number of copper particles per 100 grams has increased to ~300 million. This greater number of iron-copper particle interfaces enhances copper diffusion into the iron prior to the copper melting [3, 6, 10]. A critical requirement for the reduced copper particle size is that they are uniformly dispersed throughout the premix. One methodology to prevent the fine copper from segregating is to 'bond' the copper to the iron. Diffusion bonding and chemical bonding prevent copper segregation but diffusion bonding adds additional cost to the raw material. Chemical bonding has proven effective at bonding these fine copper particles [11]. Ideally it should be advantageous to prealloy the copper in the iron powder. However, prealloying this amount of copper will have a deleterious effect on the compressibility of the resulting iron powder.

Fig. 2: Photomicrograph showing the distribution of -15 micron copper particles in FC-0208

Other considerations in the dimensional control of copper steels are the effect of varying part density, sintering atmosphere and particle oxides present on the powder surfaces. Higher part densities result in higher DC; for example, an FC-0208 at 6.8 g/cm³ green density will have a sintered DC of ~0.3%; whereas, at a green density of 7.3 g/cm³ the sintered DC will be ~0.5% [3]. This presents two problems; parts having multi-levels with varying density distributions require careful die design to accommodate the significant difference in absolute dimensional change. Additionally, achieving high sintered component density (>7.2 g/cm³) in copper steels requires the use of diffusion bonded copper additions to minimize growth at these high green densities [3]. Relative to sintering atmospheres and particle oxides, Bernardo and others demonstrated that a reducing atmosphere significantly lowers the contact angle of the copper during sintering [5]. Also, if copper powders are pre-alloyed with 2% silicon, these additions dramatically lowers the wetting angle in both inert and nitrogen hydrogen atmospheres. The silicon is thought to act as a type of 'getter' to help reduce the iron powder surface oxides.

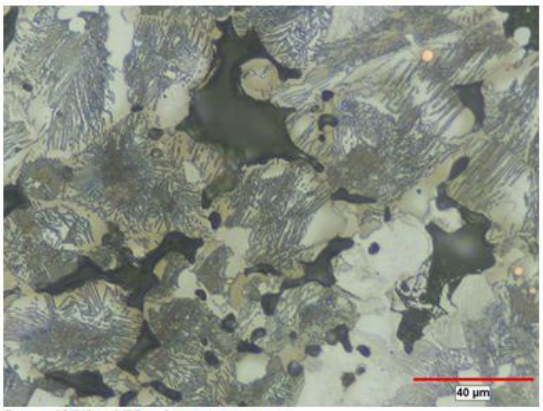

3a: With -150 micron copper

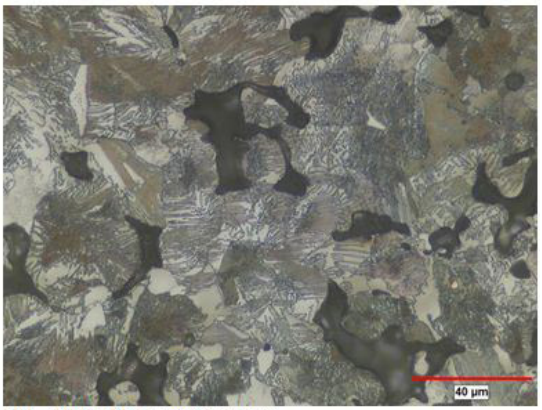

3b: With -15 micron copper

Fig. 3: Evidence of large pores from -150 micron copper and finer pores from a finer copper particle

This paper will detail the experimental methods used to achieve superior dimensional change consistency in an FC-0208 premix used in a VVT application. Part functionality required a +/- 40 micron tolerance on a 3.3 inch (84 mm) diameter. To achieve this level of dimensional precision, the part required sizing after sintering and the critical pump surfaces were ground to tolerance after induction hardening. Minor variations in DC were counteracted by adjusting both the sintering temperature and time at temperature. However, excessive variations could not be tolerated because it required excessive machining or, in the worst case, producing a part that was out of specification. Both instances resulted in significant negative cost implications. To address this issue, a study was undertaken to investigate the potential cause of the variations, what could be done to minimize these variations on a short term basis, and, most importantly, what could be done to ensure long-term stability of the process while minimizing rejections.

Experimental Procedure

The VVT part investigated was a three-level part having a major sprocket diameter of ~5.3 inches (134.6 mm) with an inner diameter of 3.3 inches (84 mm) and an overall height of ~0.8 inches (20 mm), see as shown in Figure 4. Part mechanical requirements necessitated that the sprocket flange region maintain a sintered density of ~6.9 g/cm³, while the specification of the major long hub was an overall green density of ~6.8 g/cm³ min. The major short hub is formed by a fixed step in the upper punch. Compaction was performed utilizing a mechanical press and sintering was done nominally at 2050 °F (1120 °C) for ~25 minutes at temperature in a 95% nitrogen / 5% hydrogen atmosphere. The MPIF FC-0208 powder was premixed using Hoeganaes' proprietary ANCORBOND® processing. Quality control testing of the premix evaluated each premix lot for sintered carbon, sintered copper, absolute DC, and DC as measured via difference from a standard lot (DFS) sintered simultaneously with the production lot. All dimensional change data was measured using MPIF standard TRS bars compacted to a 7.0 g/cm³ green density and sintered at 2050 °F (1120 °C) in a 75% hydrogen / 25% nitrogen atmosphere for 30 minutes at temperature.

Critical part dimensions on this VVT component are the major ID short hub OD and long hub OD as shown in Figure 4. As noted earlier,

both required a sintered diametrical tolerance of + / - 40 microns. To establish the required sintering parameters, sintering trials of an initial quantity of parts were done from each new lot quantifying the required temperature and time at temperature. However, only minor variations in these two parameters were permitted. Excessive variations resulted in parts that could not be properly sized.

Fig. 4: Photograph of VVT part showing major short hub OD on left and major long hub on right

Results

At the inception of this program, dimensional variations were resulting in unacceptable levels of rejected parts. Paretoanalysis showed that the major cause for part rejection was an under size condition on the critical 84 mm diameter dimension. As per the standardized QC testing of each premix lot, all lots produced met the established specification for both absolute DC and difference from standard. However, it was acknowledged that either the standard testing was inappropriate or a new specification and /or a new standard lot were required. To produce immediate results, production of the premix was modified to produce greater sintered dimensional change. This was initially accomplished by substituting ~10% of the standard size copper (-150 micron) with fine copper (-15 micron). This proved successful but required lot-to-lo adjustments of the amount of the fine copper addition, so as to produce the desired result. The second and final iteration on the premix evaluated the use of only fine copper to affect the dimensional change desired. This iteration was pursued vigorously because it offered the potential to chemically bond the fine copper, thus preventing potential segregation effects and it offered the possibility of a slight reduction in the total amount of copper added to achieve the same dimensional change.

Prior to any changes to the premix; the absolute dimensional change (DC) and difference from standard (DFS) of DC were monitored and recorded. The difference from standard (DFS) varied 0.06%before the change in copper type was applied, as seen in Figure 5. This value was well within the original specification jointly developed. As noted, analysis of the reject causes showed that the major cause was undersize on the critical 84 mm diameter. Thus, the change implemented was a transition to utilizing fine

copper (-15 microns). In doing so, the DC DFS was reduced from a max of 0.06% to a max spread of 0.04%. How this initial change affected the production experience is shown as Figure 6. Prior to the start of this effort, non-conforming parts comprised approximately 4.5% of the total production. This high rate of non-conformity had a pronounced impact on productivity and, ultimately, cost of production. After the implementation both resetting the specification limits and replacing the copper addition as fine copper, the non-conformity rate was reduced to about 0.51%.It was also rationalized that the use of the fine copper enabled more complete chemical bonding of the copper alloy addition to the iron powder. As such, this promoted greater uniformity of the copper distribution with a corresponding improvement in flow rates of the powder. Total production experience showed that this premix resulted in considerable enhancements in total part processing and reduced final inspection costs.

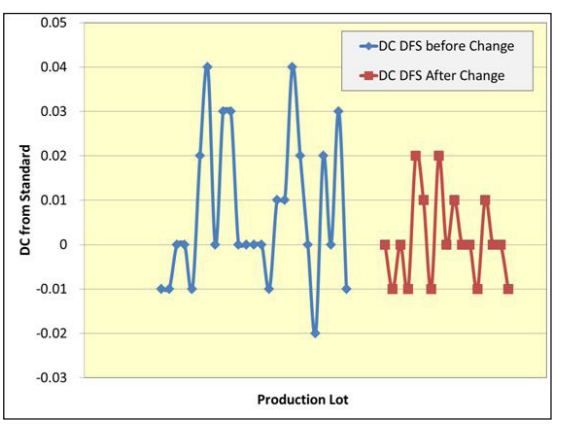

Fig. 5 : Dimensional control of FC-0208 premix used for VVT, using TRS bars compacted to a 7.0 g/cm³ green density.

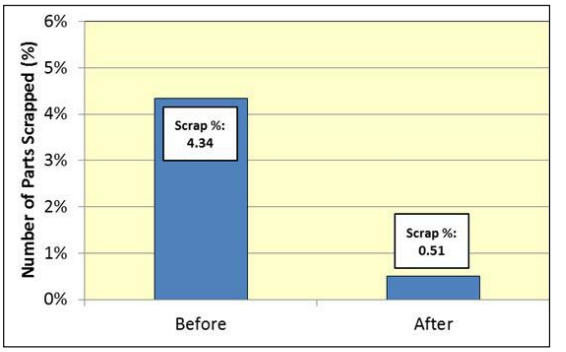

Fig. 6 : Reject rates before and after the various changes

Laboratory studies focused on the sintering response of coarse vs. fine copper additions to the FC-0208 premix. Shown in Figure 7 is the sintering response of two production lots, TRS bars were compacted to 6.6 g/cm³ and 7.0 g/cm³ green densities. These two lots were specifically chosen because they represented material that showed a 0.08% difference in DC in both QC testing and in actual part production. The data presented in Figure 7 utilized 100% of the -150 micron copper powder. Nearly 100% of the dimensional change variation occurred after the copper melted. Unfortunately no differences in particle size analysis, powder morphology or particle surface oxides were found to explain this difference in behavior.

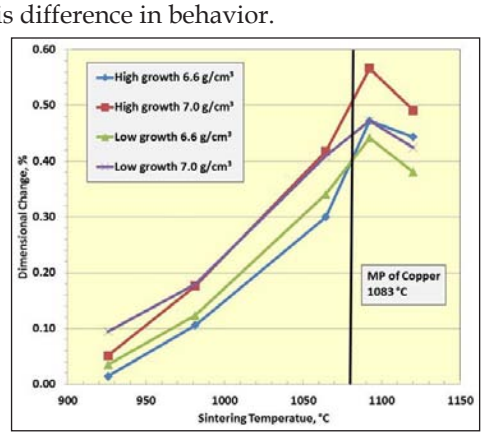

Fig. 7 : Dimensional change of two premixes with DC +/- 0.4 of the nominal value

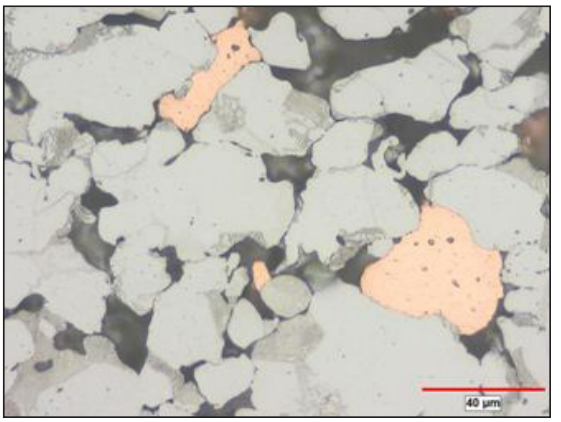

Fig. 8a : Sintered at 845 °C

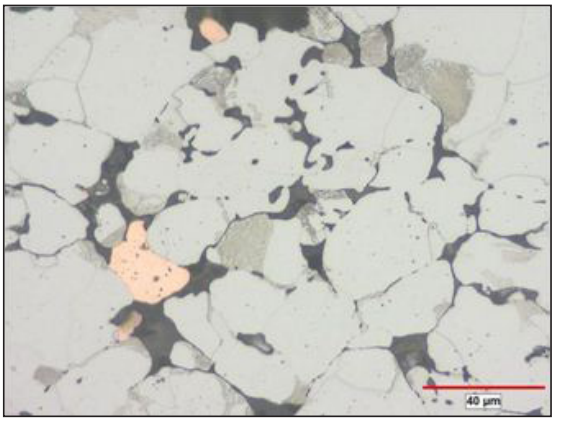

Fig. 8b : Sintered at 870 °C

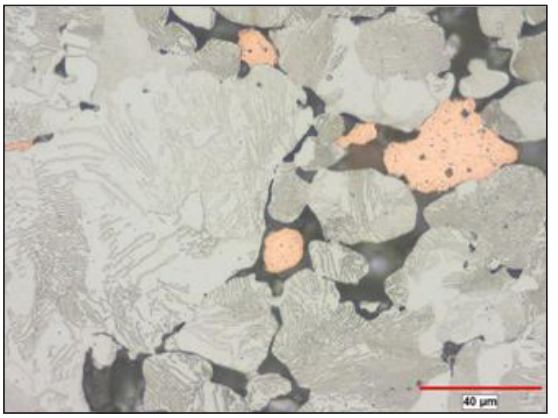

Fig. 8c : Sintered at 980 °C

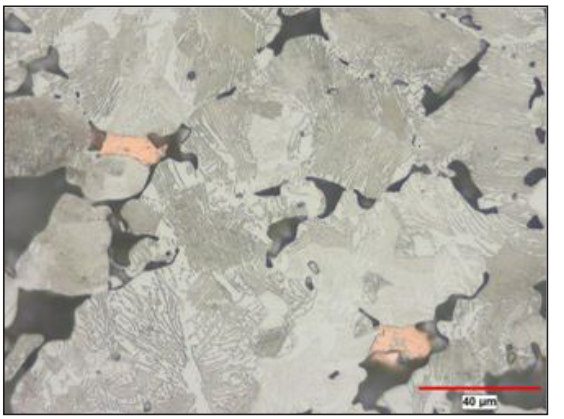

Fig. 8d : Sintered at 1065 °C

Fig. 8 : Photomicrographs showing the carbon diffusion at temperatures ranging from 845 °C to 1065 °C.

A metallographic analysis of the conditions presented in Figure 8 showed that the onset of graphite diffusion is about 1550 °F (843 °C) and 100% of the graphite is in solution at approximately 1750 °F (954 °C), Figure 8c. Thus the dominant variable associated with the copper growth is the melting and diffusion of the copper. Smaller particle size copper did not alter the graphite going into solution. Even with the fine copper addition, the copper particles are readily apparent at temperature up to 1065 °C. Murphy has reported that just below the melting point of the iron, the fine copper particles show significant solid state diffusion [6]. This would explain the higher growth associated with the smaller copper particle sizes.

As noted above, fine copper additions have the disadvantage of giving higher growth for an equivalent weight percentage addition. This experimental work suggested that a 1.85% fine copper addition gave the same growth as a 2.1% addition of the regular copper. This 1.85% addition is within the specification limits for an FC-0208 and a minor reduction in TRS strength

was observed; however, the TRS strength met the nominal limits established in MPIF Std. 35 for FC-0208.

One final comment, as with all fine particle additions, additions of the fine copper are best added via high shear mixing techniques. This promotes greater copper uniformity throughout the premix and minimizes potential agglomerates of the fine particle sizes. Either metallurgical or chemical bonding is advantageous to prevent potential segregation of the fine particle additions.

Summary

As a result of the experimental work performed during this study, the following observations were made:

1. It is extremely important to specify the correct standard and specification limits for any PM part. Choosing an inappropriate standard can lead to potentially high rates of non-conforming parts.
2. Careful design of the tooling is necessary to compensate for the differences in dimensional change resulting from varying part densities. This is particularly valid in copper steels.
3. Utilizing smaller particle size copper additions reduce or eliminate large pores resulting from copper melting. This has the potential advantage of improved mechanical properties.
4. Using a -15 micron copper particle size vs. a -150 micron particle size necessitates that lesser amounts of copper be used. The fine copper addition has a significant large number of copper-iron particle contacts; thus, promoting greater copper diffusion into the iron.
5. With careful control of the premixing and utilizing the proper standards, it is possible to maintain a + / -40 micron tolerance on an 84 micron diameter.
6. Significant reductions in non-conforming parts were realized with a corresponding reduction in inspection costs and improvements in part productivity.

References

1. D. Schaefer, C. Trombino, "State of the North American P/M Industry – 2005", *Int. Journal of Powder Met.,* **48**(4), 27- 32 (2005)
2. Peter Johnson, "2008 PM Design Excellence Awards Competition Winners", *Int. Journal of Powder Met.,* **44**(4), 21 -35(2008).
3. M. Marucci, F. Hanejko, "Effect of Copper Alloy Addition Method on the Dimensional Response of Sintered Fe-Cu-C Steels", *Advances in Powder Metallurgy and Particulate Materials*, M. Bulger and B. Stebick, Metal Powders Industry Federation, Princeton NJ, 11 - 21(2010).
4. I.Cristofolini, M Pilla, A. Molinari, C. Menapace, M. Larson, "DOE Investigation of Anisotropic Dimensional Change During Sintering of Iron-Copper-Carbon", *Int. Journal of Powder Met.,* **48**(4), 33-44 (2012).
5. E. Bernardo, R. de Oro, M. Campos, J. Torralba, "New Findings on the Wettability and Spreading of Copper on Iron-Base Substrates", *Int. Journal of Powder Met.*, **51**(4), 29 36 (2015).
6. T. Murphy, "The Investigation and Evaluation of Sintered Ferrous PM Materials Using Metallographic Techniques", MPIF Sintering Seminar, September 23 – 24, 2008, Cleveland Ohio.

7. R. Lawcock, T. J. Davies, "Effect of Carbon on Dimensional and Microstructural Characteristics of Fe-Cu Compacts during Sintering", *Powder Met.*, **33** (2), 147-150 (1990).

8. B. Lindsley, T. Murphy, "Dimensional Control in Copper/Nickel-Containing Ferrous Powder Metallurgy Alloys", *Int. Journal of Powder Met.*, **43**(1), 17-26 (2007).

9. T. Murphy, M. Baran, "An Investigation into the Effect of Copper and Graphite Additions to Sinter Hardening Steels", Advances in Powder Metallurgy and Particulate Materials—2004, W. James and R. Chernenkoff, Metal Powders Industry Federation, Princeton NJ, 266 - 274 (2010).

10. U. Engstrom, "Copper in PM Steels", *Int. Journal of Powder Met.*, **39** (4) 29-39 (2003).

11. F. J. Semel, "Processes Determining the Dimensional Change of PM Steels", Advances in Powder Metallurgy and Particulate Materials—2001, W. Eisen and S. Kassam. Metal Powders Industry Federation, Princeton NJ, 31 – 42 (2001).

GRAIN BOUNDARY SLIDING ASSISTED DENSIFICATION DURING INITIAL SINTERING STAGE OF MECHANICALLY ALLOYED CoFeNi POWDERS

Rahul B. Mane, Bharat B. Panigrahi

Department of Materials Science and Metallurgical Engineering,
Indian Institute of Technology Hyderabad, Kandi, Sangareddy, Telangana, India

Abstract : A multi-principal-element alloy with simple solid solution gives the unique combination of properties, which has led to the development of medium and high entropy alloys (HEA). Because of its elevated temperature phase stability and good oxidation resistance; they have potential for various applications such as aerospace, nuclear, automobile etc. The mechanical alloying method is known for its capability for extending the solid solubility limits and making the alloys of those metals which are difficult to form through conventional method. Sintering can be done to get high density products from as-milled powders. Densification is dependent on many things, out of which diffusivity is one of the important parameter. However, till date there is no clarity about densification behavior of HEA powders; and hardly there has been any study on their sintering kinetics. The present investigation aims to study the densification behavior of mechanically alloyed CoFeNi medium entropy powders through the help of dilatometer. It was observed that when the green compact was heated, sample expanded slowly, as result of thermal expansion behaviour of the material. While continuous heating, in the temperature range of about 250 to 450 ^{o}C, sample exhibited noticeable shrinkage. After this temperature, on further heating, sample started expanding again till about 800°C. Above this, sample shows continuous shrinkage, attributed to the diffusion based sintering. However, the shrinkage anomaly observed during 250 to 450°C range, could not be attributed to the diffusional process. It appears that this densification could be related to grain sliding phenomenon. To understand in details, the data was analyzed through the available diffusional-creep based models;which states that the sliding of grains can occur due to the movement of dislocations, i.e., dislocation gliding, climbing, and annihilation. Many of the school believe that such process may occur during sintering of particles. Activation energy of densification shows extremely low value, much smaller than activation energies of any diffusional mechanisms; indicating possibility of grain sliding process. This process lasts until the permanent and rigid neck form between the grains.

Keywords: Sintering, High entropy alloy, Grain boundary sliding, Dilatometer.

Introduction

Generally grain boundary sliding occurs during creep or super plasticity in ultrafine or nano size grain materials, it happens at higher temperature (lower than homologous temperature) [1]. Dislocation gliding, climbing and annihilation are the reasons for GBS, higher the dislocation density in a system more are the chances of GBS [2]. GBS mechanism mechanically distinguished in two separate types, one is Rachinger sliding[3], due presence of dislocations under applied load; another one is Lifshitz sliding, which occurs in Nabarro Herring and Coble diffusion creep[4]. It has been reported that during creep deformation, three principle mechanisms are responsible for plastic flow in material in the range of intermediate to high temperature (>0.6Tm, Tm is melting temperature) slip, grain boundary sliding (GBS) and diffusional flow. But slip generally dominates at high stresses and in fine grain material at intermediate stresses [1]. In

polycrystalline solid materials, GBS occurs when grain slides over each other or vicinity of their mutual interface under the external stresses. Langdon Terence G. has reported a model for separate rateequations for Rachinger GBS in power-law creep and during superplasticity[2].

The grain boundary sliding (GBS) andgrainboundary rotation (GBR) during sintering was rarely observed in nanocrystalline powders. Hellstern et al. studied the evolution of nanostructure formation in mechanically milled AlRu compound [5].It was reported that with milling time, dislocation density increases. As a consequenceheavily strained regions form which leads to disintegration of grains into sub-grains. These sub-grains are often in the range of 20 and 30 nm. On further processing, the grain size decreased steadily and the small-angle grain boundaries were replaced by higher angle grain boundaries [5]. Very high angle gain boundaries create favourable condition for grains to rotate. Grain boundary sliding was observed during sintering of W-Ni-Fe, where heavy tungsten particles tend to settle down due to gravity. During settling grains rotate in presence of liquid phase [6]. Grain boundary migration and grain boundary rotation have been projected simultaneously during molecular dynamic simulation, it has been also reported that rate of grain boundary rotation increased with decreasing grain size [7]. The shrinkage behavior under compressive hydrostatic pressure was related to the grain boundary sliding by Kim et al. When the neck grows very large, particles become rigid and rotation becomes difficult. Further shrinkages is only because of diffusion mechanisms [8]. The effect GBR, GBS or grain boundary migration occur in material during sintering because of elastic anisotropy at the grain boundary region [9]. The applied stress during sintering and bending moment between particles center to center approach act independently. During pressureless sintering only bending moment acts as driving force for GBR [10]. Heterogeneous structures, such as inhomogeneous initial density distribution, external stress [11], gravity and temperature gradient also deform components.

There is a relatively new class of alloy called high entropy alloy; becomes interesting filed for researches because of its unique combination of properties. Two independent publications [12,13] reported the concept of high entropy alloys or multiprincipal element alloys, last three to five years extensive research conducted on HEA's [14].HEA's defined by the configurational entropy: alloys having high configurational entropy (more than 1.5R, where R is universal gas constant). If the configurational entropy falls in the range of 1.5R to 1R then it is called as medium entropy alloys. CoFeNiis one of medium entropy alloy [15]. It is important to know sintering behaviour of CoFeNi and other high entropy alloys. Present investigation aims to study the densification behavior of mechanically alloedCoFeNimedium entropy alloy powders. Attempts have been made to understand the densification mechanism through the help of diffusional-creep based sintering models, to evaluate the possibility of operating grain boundary sliding process.

Experimental

Fe and Co powders with mesh size -325 and about 99% purity were procured from Alfa Assar and nickel powder with mesh size -325 and about 99.5% purity was procured from Sigma-Aldrich. Powders were taken in equi-molar ratio to form CoFeNi alloy and kept in high energy planetary ball mill system (Fritsch P-5) for mechanical alloying. Milling was carried out for 15 hours. The vials and ball were made of

tungsten carbide. Toluene was used as a process control agent to avoid oxidation of powder and to minimize the heat generation. Ball to powder weight ratio was 15:1 and milled at a speed of 300 rpm. The small amounts of powder were taken for x-ray diffraction study (PANalytical, Model: X'Pert PRO with Cu k_α radiation of wavelength 1.54A^0). Differential scanning calorimetry (DSC-NETZSCH) of as-milled powders were done up to 600 ^{0}C at a heating rate of 10^{0}C/min and same sample was reheated in DSC. About one gram of CoFeNi as-milled powder was pre-compacted by using steel die and punch of 7 mm diameter at low pressure (70 MPa). The one pellet was sintered in dilatometer (Theta Industries, USA, vertical dilatometer) at about 1150 ^{0}C held for 60 min, another sample was sintered nonisothermally in tubular furnace for 800 ^{0}C, and characterized by XRD for phase estability. All experiments were done under high purity argon atmosphere; heating rate was 10^{0}C/min. The powder morphology and the microstructures were characterized using a field emission scanning electron microscope (FESEM; Carl-Zeiss, Model: Supra 40). The particle size was analyzed using Delsa Nano system.

Results and Discussion

XRD analysis

Fig. 1 show X-ray diffraction profiles of as-milled, nonisothermally sintered samples at 800 ^{0}C, and isothermally sintered at about 1150^{0}C. X-ray diffraction profile of the mechanically alloyed powder shows (Fig. 1) major peaks are identical to the patterns of FCC crystal, indicating the formation of CoFeNi alloy, as a major phase. This was further confirmed with the reported XRD patterns of same alloy [16]. However, few smaller peaks were also observed, indicating the presence of small amount of impurity. Crystallite size of FCC phase estimated through the Williamson–Hall method, was found to be in the range of about 25 nm; whereas powder was found to contain residual strain of about 9.62*10^{-2}. XRD profile of nonisothermally sintered sample at about 800 ^{0}C shows broadening of FCC peaks slightly decreased. XRD profile of isothermally sintered sample at about 1150 ^{0}C shows peak positions of all peaks are shifted towards higher angle, it confirms that lattice stabilization. Crystallite size of sintered CoFeNi isothermally at about 1150 ^{0}C was found to be 1602 nm, whereas strain reduced to 1.07 * 10 $^{-3}$.

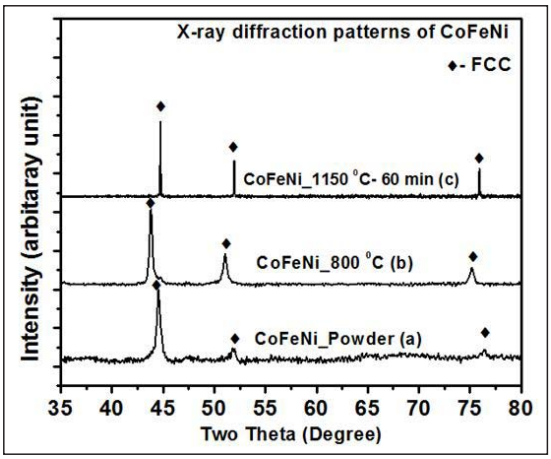

Fig.1: X-ray diffraction patterns for CoFeNi, as-milled, nonisothermally sintered at 800 ^{0}C and isothermally sintered at 1150 ^{0}C

SEM micrographs of CoFeNi as-milled powder (Fig.2.a) shows irregular shapes and highly agglomerated particles which range up to about 10μm, few particles observed to be in the nanometer range. SEM images of fractured surface of sintered sample at 1150 ^{0}C held for 60 min has been shown in Fig.2.b, showed abnormal grain growth.

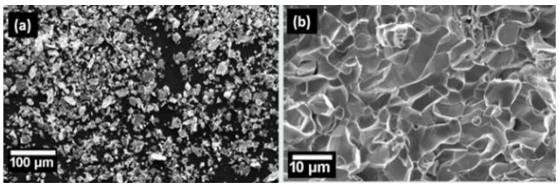

Fig.2: Scanning electron microscope image of a) as-milled b) siintered isothermally at about 1150 ^{0}C

The particle size analysis of the powder shows (Fig. 3) size of particles are in the range of 200 nm to 1500 nm.

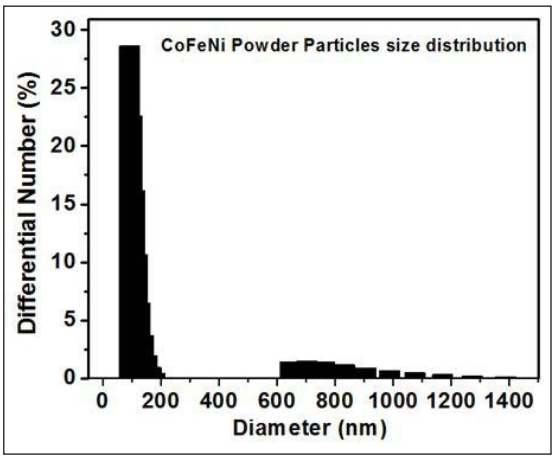

Fig.3: Particle size distribution of as-milled CoFeNi powders

Dilatometric analysis

A dilatometer curve for as-milled CoFeNi powders sintered at about 1150°C as a function of time and temperature has been shown in Fig. 4. Three heating sequences could be seen, namely, a) constant rate heating, b) isothermal holding, and c) cooling. Dilatometer curve shows variations in the expansion and shrinkage behavior of the samples at various temperatures. The curves could be divided in to six different regions, as:

(1) Initial expansion (up to about 250°C): Once the initial level of stabilization is over, the sample expanded almost linearly, due to the thermal expansion property of material, which continued up to about 250°C.

(2) Transient shrinkage (250°C to 450°C): Above 250°C, expansion slows down significantly and line started moving downwards and stopped at about 450°C, and at this range it shrank by about 1.6%.

(3) Slow thermal expansion (450°C to 600°C): Sample tends to expand again. Thermal expansion still dominates in this region while sintering continues slowly.

(4) Slowshrinkage (600°C to 800°C): At about 600°Cexpansions of the sample stops and on further heating sample started shrinking. Slow shrinkage rate is observed.

(5) Accelerated shrinkage (1000°C to 1150°C): At around 1000°C, sintering seemed to be accelerated significantly, and exhibited a large shrinkage. Sintering continued during isothermal periods; however, sintering slows gradually as time progresses during isothermal period.

(6) Thermal contraction (1150°C to RT): When the furnace was stopped after isothermal holding, sample was allowed to cool in the furnace. Sample exhibits thermal contraction down to room temperature.

Density was found to be increased from about 64% (relative green density) to about 86% (relative sintered density) at 1150°C, while considering the theoretical density of this alloy to be 8.5 g/cm^3.

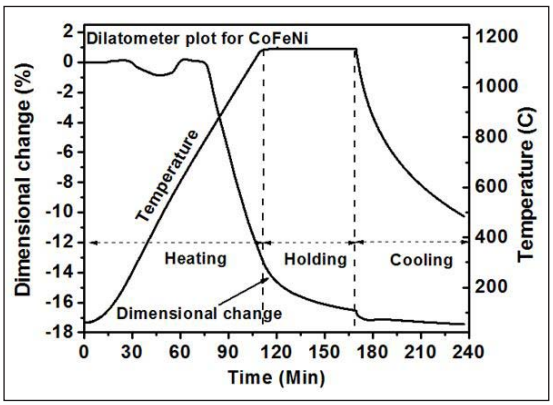

Fig.4: Dilatometer plot for as-milled CoFeNi powder

Evaluation of shrinkage data

The shrinkage observed during 250^{0}C to 450^{0}C seems to be abnormal and usually not reported. This unusual shrinkage is of particular interest in the present context; which has been taken for detailed analysis in the current work. If the diffusional sintering has to cause densification, the sample would have continued shrinking, and it would not have resumed expansion (above 450^{0}C). It appears that some other factor is also contributing in densification. Similar shrinkage anomaly was reported during sintering of nanocrystalline titanium powder which was attributed to the grain rotation [17]. Thus the observed shrinkage at early period in present work, could be attributed to the grain sliding induced particle re-packing phenomena. During heating, current mechanically alloyed HEA powder tends to undergo recovery and recrystallization processes where crystallites tend to adjust the lattice orientation to a favorable state. As a consequence, localized elastic anisotropy develops around grain boundaries which act as driving force for grain sliding. As a result, particle packing density further improves. These processes involve significant amount of energy release which could also be seen during the DSC analysis (Fig. 5). Small exothermic peak at about 320 0C observed, which might be due to stabilization of lattices, on reheating the same sample; no any peak observed in reheated sample.

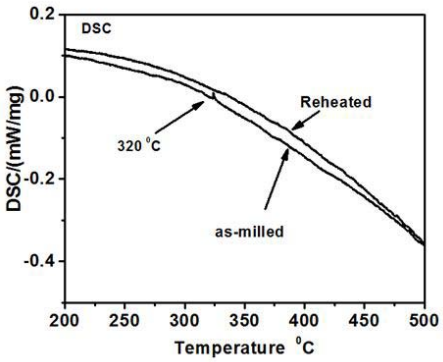

Fig.5: Differential scanning calorimetry of as-milled and reheated sample of CoFeNi

Two different models were used for analysis, grain boundary sliding based creep flow equation (1) [18].

$$\epsilon_{gbs} = \frac{(ADGb)}{kT}\left(\frac{b}{d}\right)\left(\frac{\sigma}{G}\right)^2 \quad (1)$$

Where, D= diffusion coefficient, A=10, d= grain size (crystallite size in current work =20 nm), b= burger vector, G=shear modulus, k= Boltzmann constant. $\varepsilon_{-gbs} = (dl/l0)/dt)$,

Nonisothermal sintering model (Young and Cutler model) [19]

$$\ln\left(T^p \frac{dY}{dT}\right) = -\frac{Q}{((n+1)RT)} + \ln C \quad (2)$$

Where, Y is $\Delta L/L_0$, T is the temperature, R constant, C is a constant depending on material parameters, P has the value of 3/2 for VD and 5/3 for GBD. The values of n are 1 and 2 for VD and GBD respectively.

Using equation (1) and (2) diffusion coefficient were calculated for grain boundary sliding, grain boundary diffusion and volume diffusion mechanisms. It is well known that diffusion coefficients vary exponentially with temperature; in the form of equation it can be written as [D = D0 exp(-Q/RT)] or [lnD = $\ln D_0$ –(Q/RT)]; where D_0 is frequency factor and Q is activation energy for a given mechanism. Using D values with respect to temperatures; plots of ln(D) versus 1/T were produced for four different regions, Fig. 6 shows representative plots for the region (250 ^{0}C- 450 ^{0}C). The slope of the curve is equal to Q/RT,the estimated values of Q (activation energies) have been tabulated in Table 1.

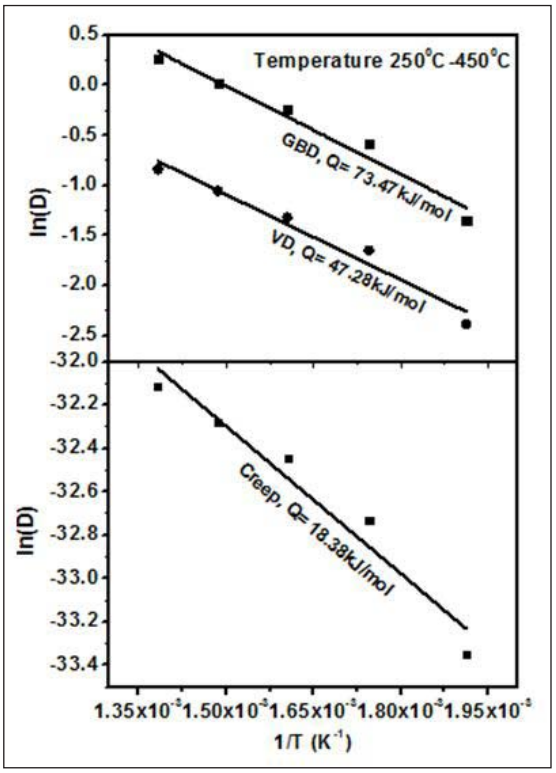

Fig. 6 : Arhenious plot for calculation of activation energies using creep and nonisothermal model

Table 1: Activation energies for grain boundary sliding (creep flow model), grain boundary diffusion and volume diffusion (non-isothermal model)

Temperature Range (^{0}C)	$Q_{\_GBS}$ (kJ/mol) Eq. No [1]	Q_GBD(kJ/mol) Eq. No [2]	Q_VD(kJ/mol) Eq. no.[2]
250 -450	18.83	73.47	47.28

Both equationsconfirm that low activation energies for first two regions, which are not attributed to any diffusion mechanism. Thus it could be attributed to the grain boundary sliding mechanism.

Conclusions

During initial period of shrinkage of mechanically alloyed CoFeNi HEA powder exhibits shrinkage at the range of 250 0C to 4500C. This shrinkage was analyzed through creep based models for grain boundary sliding and conventional non-isothermal sintering models. It shows very low activation energy compared to diffusional mechanisms; indicating possibility of operating grain boundary sliding assisted rotation phenomena. Once the rigid necks form, grain rotation stops and further shrinkage is possibility controlled by diffusional mechanisms.

References

[1] wadsworthJ., O. RuanoA., sherbyO. D, Deformation by grain boundary sliding and slip creep versus diffusional creep, The minerals, metals and materials. (1999).

[2] Langdon Terence G. Grain boundary sliding revisited: Developments in sliding over four decades.Journal of Materials Science 41.3 (2006) 597-609.

[3] Rachinger, W. A.. Relative grain translations in the plastic flow of aluminium. J. Inst. Metals, (1952)81.

[4] Lifshitz, I. M. (1963). On the theory of diffusion-

viscous flow of polycrystalline bodies. Soviet Physics JETP, 17, 909-920.

[5] Hellstern, E., Fecht, H. J., Garland, C., Johnson, W. L. (1989). In: McCandlish, L. E.,Polk, D. E., Siegel, R. W., Kear, B. H., eds.Multicomponent Ultrafine Microstructures. Vol. 132. Pittsburgh, PA: Mater. Res. Soc., 137–142.

[6] Liu Jianxin, and Randall M. German. Grain boundary sliding and component shape distortion during liquid-phase sintering. Metallurgical and Materials Transactions A 32.8 (2001): 2087-2095.

[7] Upmanyu, M., D. J. Srolovitz, A. E. Lobkovsky, J. A. Warren, and W. C. Carter. "Simultaneous grain boundary migration and grain rotation." ActaMaterialia 54, no. 7 (2006): 1707-1719.

[8] Kim, B.N., Hiraga, K., Morita, K., Yoshida, H., Sakka, Y. and Park, Y.J., 2013. Grain-boundary sliding model of pore shrinkage in late intermediate sintering stage under hydrostatic pressure. ActaMaterialia, 61(18), 6661-6669.

[9] Haslam A. J., D. Moldovan, V. Yamakov, D. Wolf, S. R. Phillpot, H. Gleiter. Stress-enhanced grain growth in a nanocrystalline material by molecular-dynamics simulation, Acta Mater. 51, no. 7 (2003) 2097-2112.

[10] Chun HwayHsuesh, Lutgard C. De Jonghe, particle rotation in early sintering, communications of the American ceramic society. (1984) C-215-C217.

[11] Olevsky E, Molinari A.Instabilit of sintering of porous bodies.Int J Plasticity (2000) 16.

[12] Cantor, B., Chang, I. T. H., Knight, P. & Vincent, A. J. B. Microstructural development in equiatomic multicomponent alloys. Mater. Sci. Eng. A 375, 213–218 (2004).

[13] Yeh, J. W. et al. Nanostructured high-entropy alloys with multiple principal elements: novel alloy design concepts and outcome. Adv. Eng. Mater. 6, 299–303 (2004).

[14] PickeringE.J., JonesN.G., High-entropy alloys: a critical assessment of theirfounding principles and future prospects, Int. Mater. Rev. 61 (2016) 183-202.

[15] Zhijun Wang et al. Nanoindentation characterized initial creep behavior of a high-entropy-based alloy CoFeNi. Intermetallics 53 (2014) 183-186.

[16] S. Praveen, B.S. Murty, R.S. Kottada, Phase evolution and densificationbehavior of nanocrystalline multicomponent high entropy alloys during spark plasma sintering, JOM 65 (2013) 1797-1804.

[17] PanigrahiB. B., GodkhindiM. M.Das, K.,MukundaP.G.,DabhadeV.V.,Ramakrishnan P., Sintering mechanisms of attrition milled titanium nano-powder, J. Mater Res. 20 (2005) 827-836.

[18] Langdon, Terence G. Grain boundary sliding as a deformation mechanism during creep. Philosophical Magazine 22.178 (1970): 689-700.

[19] Han, J., Senos, A. M. R., & Mantas, P. Q. Nonisothermal sintering of Mn doped ZnO. J. Eur. Ceram. Soc. 19, 1003-1006 (1999).

EFFECT OF MECHANICAL ALLOYING ON MECHANICAL PROPERTIES OF RHENIUM ADDED TUNGSTEN HEAVY ALLOYS

U. Ravi Kiran, M. Sankaranarayana, G. V. S. Nageswara Rao[#], T. K. Nandy

Defence Metallurgical Research Laboratory, Kanchanbagh, Hyderabad, India.
[#] National Institute of Technology, Warangal, India.

Abstract : The effect of mechanically alloyed tungsten-rhenium powder on the microstructure and mechanical properties of 89W-7Ni-3Fe-1Re heavy alloy was investigated. XRD analysis showed that high energy milling of tungsten-rhenium powders resulted in formation of BCC solid solution. The corresponding particle and the crystallite size of powders reduced after milling. Alloy with above mentioned composition was prepared by liquid phase sintering using both high energy milled (mechanically alloyed) and un-milled elemental powders. Grain size and contiguity of W particles of the alloy sintered by high energy milled powders were significantly lesser as compared to the alloy sintered with powders that were not subjected to high energy milling. The strength, ductility and impact toughness of milled alloy were relatively superior to those of the conventional alloy. The improvement in properties was attributed to finer grain and lower contiguity of the tungsten particles in the milled alloy. The results underline the beneficial influence of high energy milling on the microstructure and mechanical properties of liquid phase sintered heavy alloys.

Keywords: Mechanical alloying, tungsten heavy alloy, grain size, high energy milling.

1. INTRODUCTION

Tungsten heavy alloys mainly used in applications such as kinetic energy penetrators, radiation shields, counter weight balances, and vibration damping devices due to their high density and good mechanical properties [1-2]. However, because of high density much attention is paid towards processing of kinetic energy penetrators. A wide variety of alloying elements have been explored in order to improve the mechanical properties of these alloys. Research has been directed addition of alloying elements such as cobalt, tantalum, rhenium, molybdenum, manganese, chromium etc. In recent times rhenium alloying has received considerable attention. However, rhenium addition affects the dissolution issue in the microstructure because of its higher melting point (3182 °C). It leads deterioration of mechanical properties. Mechanical alloying is one way to improve the mechanical properties of these alloys [3]. Therefore, in the present study, mechanical alloying was performed on tungsten and rhenium powders using high energy planetary ball mill. A 89W-7Ni-1Fe-1Re alloy was fabricated by both conventional and mechanical alloying routes. The alloys were processed by cold iso-static pressing, liquid phase sintering, vacuum heat treatment and swaging. Mechanical properties were evaluated and correlated with underlying microstructure.

2. EXPERIMENTAL WORK

Milling of W-1%Re powders was performed for 5 hours using planetary ball mill using tungsten balls as grinding media. A ball-to-powder weight ratio of 5:1 and a 670 rpm speed were adopted. The milled W-1% Re powders were then mixed with nickel and iron powders in a ball mill (BPR: 1:1) for 48 hours. In order to compare, tungsten alloy blanks of 89W-7Ni-3Fe-

1Re (Wt.%) were prepared by both conventional and milling routes. A cold iso-static press of 200 MPa pressure was employed to obtain cylindrical blanks. The green compacts were subsequently sintered under hydrogen furnace at 1480°C for 2h followed by vacuum heat treated and oil quenched. Swaging was carried out in order to improve the mechanical properties. While the green density was determined by dimensional measurements, Archimedes principle was used to evaluate the density of sintered specimens. For the microstructural characterization scanning electron microscopy (Make: FEI, Quanta-400, Netherlands) was used. The microstructural measurements like grain size, W-W contiguity, dihedral angle, matrix volume fraction and connectivity were described elsewhere [4, 5]. The tensile specimens were tested at room temperature using universal tensile testing machine (INSTRON 5500R, UK). Charpy impact specimens were prepared and evaluation was carried out using impact testing machine. At least three specimens were tested for each condition. Fractography of broken tensile and impact specimens were carried out using Scanning electron microscope.

3. RESULTS

3.1. Density and Microstructure

The sintered densities of the alloys are shown in Fig. 1. The milled alloy displays higher sintered density as compared to conventional alloy. This is due to high energy milling causes repeated welding, fracturing and re-welding that facilitate uniform distribution powders [3].

Fig. 2 shows the microstructures of tungsten alloy consolidated by conventional and milling conditions. It can be seen, the milled alloy shows finer grain size as compared to the conventional alloy. Further, the grains are more rounded with minimum shape accommodation effect.

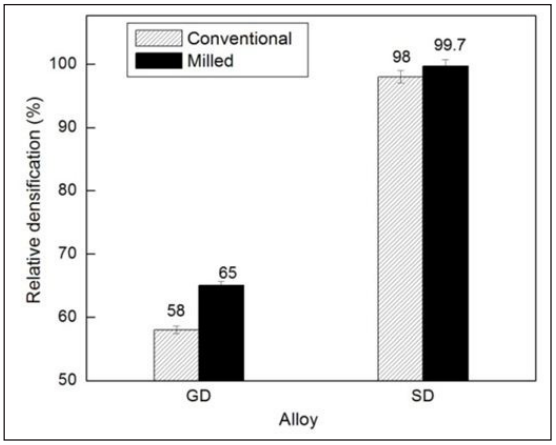

Fig.1. Relative densification of the alloys. GD: Green density, SD: Sintered density.

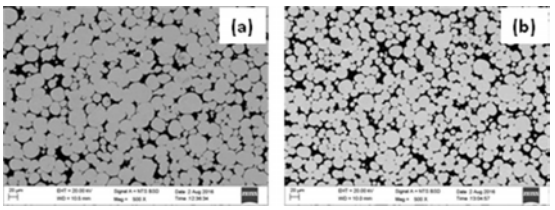

Fig. 2. Back scattered electron images of tungsten heavy alloys prepared from (a) conventional and (b) milled conditions.

The rounding of grains is due to decrease in Ostwald ripening process because of finer grain size. Moreover, the milled alloy exhibits more uniform distribution grains as compared conventional alloy. This is ascribed to initial high energy milling that ensures homogenous distribution of particles in the powder mix. Microstructural parameters are listed in Table 1.

Table 1. Microstructural parameters of tungsten heavy alloys.

Alloy	Tungsten grain size (μm)	Volume fraction of matrix (Pct)	Contiguity	Dihedral angle	Co-ordination number
Conventional	25±11	17±3	0.36±0.07	58±1	2.8±3
Milled	18±6	19±1	0.27±0.06	42±2	1.7±1

The milled alloy shows substantially reduced contiguity, which may be due to relatively more uniform microstructure in terms of W-particle size and their distribution. The effect of these microstructural parameters on mechanical properties is shown in the following sections.

3.3. Mechanical properties

Fig. 4 Show the tensile properties of alloys. In both heat treated and swaged conditions, the milled alloy exhibits higher yield and tensile strength as compared to conventional alloy.

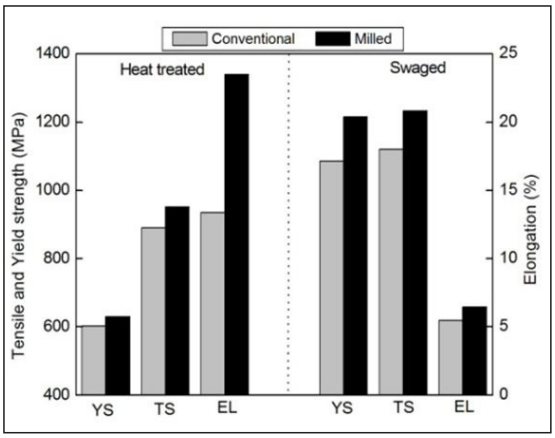

Fig. 4. Tensile properties of the alloys investigated.

The results are summarised in Table 2. The higher yield strength in the milled alloy is a result of finer grain size, which is in well agreement with classical Hall-Petch relationship.

Table 2. Mechanical properties of heavy alloys investigated.

Alloy	Sintered plus heat treated			Sintered plus heat treated plus swaged			
	Tensile strength (MPa)	Yield strength (MPa)	El (%)	Tensile strength (MPa)	Yield strength (MPa)	El (%)	Impact strength (J/cm^2)
Conventional	890±6	602±6	14±4	1121±5	1086	4±3	27±10
Milled	952±3	629±3	23±1	1232±2	1215	7±1	62 ±6

In spite of higher yield strength, the milled alloy show enhanced ductility values in comparison with conventional alloy. This is expected, because milled alloy attains low contiguity and more uniform microstructure. It can be seen from Table 1, that the significant decrease in contiguity of the milled alloy (0.27) as compared to conventional alloy (0.36). A relation between elongation and contiguity of heavy alloy is as follows [6]:

$$\varepsilon = \varepsilon_0 + kV_m(1 - C_{WW}) \quad (1)$$

where ε is the elongation to failure, ε_0 and k are non negative constants which have no explicit physical meaning, C_{ww} is the contiguity and V_m represents matrix volume fraction. As the contiguity goes up, % elongation comes down. Finally, the impact values of alloys processed by different routes are shown in Table 2. The milled alloy displays about two fold increase in impact toughness. The higher impact toughness may again be attributed to lower W-W contiguity and connectivity.

Fig. 5 shows the fractographs of tensile specimens in heat treated condition. Both conventional and milled alloys display predominant intergranular fracture mode. However, formation of continuous matrix networks all over the fractograph in the milled alloy implies higher ductility. These kind of features are related higher strength and ductility [7]. Further, the features are consistent with swaged fractographs (Fig. 6). In summary, it has been clearly shown in this study, that mechanical alloying of refractory metals prior sintering resulted improved mechanical properties.

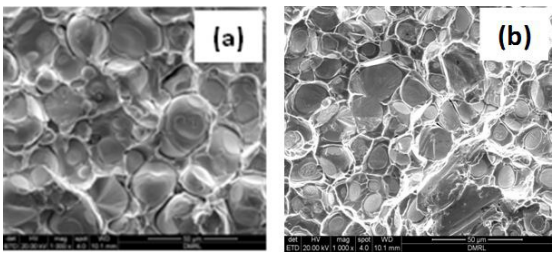

Fig.5. Fractographs of failed heat treated tensile specimens in: (a) conventional and (b) milled conditions.

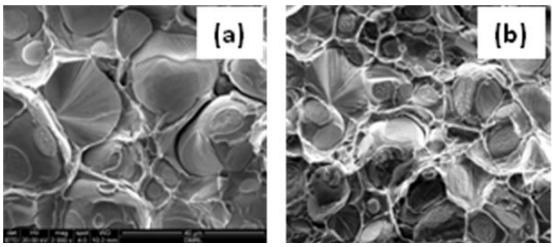

Fig.6. Fractographs of failed swaged tensile specimens in: (a) conventional and (b) milled conditions.

5. Conclusions

In the present study the effect of mechanical milling on microstructure and mechanical properties of liquid phase sintering has been studied. The important observations are summarized as follows:

1. Mechanical milling of tungsten and rhenium results in the formation of bcc W-Re rich solid solution.
2. Significant reduction in grain size and contiguity is observed in the milled alloy after liquid phase sintering.
3. The milled tungsten alloy exhibits higher strength, ductility and impact toughness as compared to the conventionally processed alloy.
4. Milling of refractory metals (W and Re in this case) prior to sintering is one way to homogenize the microstructure and thus, improve the mechanical properties of conventional tungsten heavy alloys.

Acknowledgements

Authors convey their sincere gratitude to Dr. S. V. Kamat, Distinguished Scientist & Director, DMRL for encouragement and kind permission to publish this work. Authors gratefully acknowledge the financial support provided by DRDO.

References

[1] S.R.Lampman, ASM Metals Hand book (1990).

[2] E. Ariel, J. Barta, P. Brandon, Powder Metall. Int. 5 (1973) 126.

[3] C. Suryanarayana, Prog. Mater. Sci. 46 (2001) 1-184.

[4] G.K. Williamson, W.H. Hall, Acta Mater. 1 (1953) 22.

[5] W.D. Cai, Rev. Part. Mater. 3 (1995) 71-132.

[6] R.M. German, liquid phase sintering, Plenum Press, NY (1985).

[7] U. Ravi Kiran, A. Panchal, M. Sankaranarayana, T.K. Nandy, Int.J.Refract.Met.Hard Mater. 37 (2013) 1-11.

INVESTIGATION OF THE WIRE-EDM CHARACTERISTICS ON CP-TITANIUM POWDER METALLURGY COMPONENTS - AN RSM APPROACH

Arunangsu Das [1*], Malobika Karanjai[2], Susenjit Sarkar[3], Goutam Sutradhar[3]

[1]Department of Mechanical Engineering, A.P.C. Ray Polytechnic, Jadavpur, Kolkata, West Bengal, India
[2]International Advanced Research Centre for Powder Metallurgy and New Materials (ARCI), Hyderabad, India
[3]Department of Mechanical Engineering, Jadavpur University, Kolkata, West Bengal, India

Abstract : The present work was undertaken to investigate and characterize the machining parameters (such as metal removal rate, surface roughness, etc.) of uni-axially pressed commercially pure (CP) Titanium sintered powder metallurgy components. Powder was uni-axially pressed at designated pressure of 840 MPa to form cylindrical samples and the green compacts were sintered at 0.001 mbar for about 4 hours with sintering temperature varying from 1350°C to 1450°C. The influence of the sintering temperature, pulse-on and pulse-off time at Wire-EDM on the MRR and surface roughness of the preforms has been investigated thoroughly. Experiments were conducted at different machining parameters in a CNC operated Wire-cut EDM. The MRR and surface roughness of the machined surface was measured and critically analysed.

Keywords: Titanium, Powder Metallurgy, Wire-EDM, Metal Removal Rate, Surface Roughness, Box-Behnken Design

Introduction

In the recent years, an increasing demand for Titanium alloys in bio-medical applications has been reported. It is non-toxic and bio-compatible, hence widely used as prosthetics, as well as dental implants. Since it is non-ferromagnetic, so patients with titanium implants can be easily examined with MRI. Due to its high tensile strength to density ratio, high corrosion resistance & good fatigue resistance, it is also widely used in aircrafts & high-cost automobiles. F.H. Froes et al. [1] reported that Titanium alloys offer improved performance in aerospace and terrestrial systems due to their excellent corrosion resistive bahaviour and outstanding mechanical properties. However, high cost of Titanium alloys compared to other competing materials, having similar properties, limits their widespread use. Powder metallurgy (PM) processes offer the possibility of decreasing the manufacturing costs.

Porous Ti-based alloys are being developed now-a-days as an alternative orthopedic implant material, as they can provide good biological adaptability through bone tissue in-growth into the porous network. Titanium is very difficult to cast, because it oxidizes easily at higher temperatures.The powder metallurgy technique easily transforms metallic powders into solids, with desirable porosity, using press and sinter methods. The use of the powder metallurgy in the biomedical area is advantageous for the production of prosthesis into near net shapes, with dense or controlled porosity. C.N. Elias et al. [2] reported that commercially pure Titanium (Cp-Ti) is the best bio-compatible metallic material, because its surface properties corroborate spontaneous build-up of a stable and inert oxide layer. They also concluded that several experiments have compared Cp-Ti to Ti-6Al-4V implants in rabit bones and it was found

that when twisted, Cp-Ti implants had higher removal torque values than Ti-6Al-4V screws with significantly higher bone contacts.

W. Chen et al. [3] investigated the die-pressing behavior of the CP-Ti and Ti-64 powders in the case of disk shape sintered products with three different aspect ratios, i.e., 0.5, 1, and 2. In the studied die-pressure range, an empirical powder compaction equation: $\ln (1/(1 - D)) = A\sqrt{P} + B$, (where A = a constant representing compressibility, B = Y-intercept), gave a linear relationship between the green density (D) and compaction die pressure (P), for both the as-received and milled Ti-64 powders. Ti-64 exhibited significantly higher sinterability than CP-Ti. The higher sinterability of Ti-64 powder is believed to be due to its larger specific surface area and the high diffusivity of V in β-Ti at the temperature of 1300°C, which facilitated the sintering process.

Titanium is very difficult to machine, through the conventional route. It is a poor conductor of heat. Heat, generated by the cutting action, does not evaporate quickly. Therefore, most of the heat gets concentrated on the cutting edge and tool face of the cutter. It has a strong alloying tendency with cutting tool materials at machining temperatures. This causes welding of chips at the cutting tool. Titanium has low modulus of elasticity. Its Young's modulus is 116 GPa compared to that of iron (211 GPa). This means that the work-piece tends to move away from the cutting tool under heavy cutting forces. Slender parts tend to deflect under tool pressure and this causes machine tool chatter and vibration leading to tolerance problems. Rigidity of the entire machining system is consequently very important, while machining titanium. Titanium's work-hardening characteristics are such that, while machining, a high shearing angle is formed. For reasons out-lined above, non-conventional machining process can be an alternative method for machining titanium.

Anish Kumar et al. [4, 5] developed a quadratic model for dimensional deviation to correlate the dominant machining process parameters: for example, pulse-on time, pulse-off time, peak current, spark voltage, wire feed, and wire tension, in the WEDM process of pure titanium (grade-2). It was observed by them that pulse-on time and peak current deteriorated the integrity of machined surfaces resulting in formation of deep, wide & overlapping craters, pockmarks, debris and micro cracks, formed due to high pulse-on time and peak current. D. S. Badkar et al. [6] investigated that, heat input (HI) plays an important role in deciding the tensile strength of the laser-hardened commercially pure titanium material. In case of Laser Transformation Hardening (LTH), as scanning speed increases, heat input decreases and vice-versa. Conversely, as laser power increases heat input increases and vice-versa. Scanning speed and laser power both have positive effect on all the responses investigated.

M. Manjaiah et al. [7] studied the optimization of surface roughness and metal removal rate (MRR) through wire electric discharge machining (WEDM) of TiNi Shape memory Alloys (SMA). They performed the analysis of means (ANOM) and analysis of variance (ANOVA) on signal to noise (S/N) ratio for determining the optimal parameter levels. The optimization process of Wire-EDM of TiNi SMA indicated that pulse duration significantly affected the material removal rate and surface roughness parameters of the machined samples. Discharge craters, micro cracks and recast layer were observed on the machined surface at large pulse duration. M.M. Rahaman et al. [8] developed an optimised model to analyse the effects of peak current,

pulse-on time and pulse-off time parameters in electric discharge machining (EDM) of Ti6Al4V alloy utilizing copper tungsten electrode. As peak current increased, surface roughness of the workpiece increased, likewise, surface roughness increased with pulse-on time. The optimum setting of pulse off time that generated minimum roughness, changed with peak ampere. The EDM parameters for optimum machining efficiency are 2A discharge current, 400 µs pulse on time and 232 µs pulse off time in the case of optimal surface finish.

Farnaz Nourbakhsh et al. [9] studied the influence of zinc-coated brass wire on the performance of WEDM as compared with high-speed brass. Compared to high-speed brass wire, zinc-coated brass wire resulted in smoother surface finish and higher cutting speed. Also, SEM photographs proved that uncoated wire produces a surface finish with more cracks, craters and melted drops. M. P. Garg et al. [10] studied the effect of process parameters on cutting rate in WEDM of Ti 6-2-4-2 alloy using Box-Behnken designs. They considered six control factors viz. spark gap set voltage (SV), pulse-on time (TON), pulse-off time (TOFF), peak current (IP), wire feed (WF) and wire tension (WT) at three levels. An empirical relation was obtained for cutting rate (CR) using regression analysis.

Till date no major work has been reported on the machining of CP-Titanium powder metallurgy products. CP-Ti is easily available as bars and rods, but manufacturing of bio-medical prosthesis, such as hip-joints or dental implants, requires lot of machining, which is very difficult, in case of titanium. So, it would have been beneficial, if a near-net shape component of hip-joint or dental implant can be made through powder metallurgy route, and thereafter, minor machining of the same component can easily be done through the non-conventional route. The objective of this study is to optimize the process parameters during formation of P/M parts (i.e., sintering temperature) and during Wire-EDM (i.e., pulse-on time and pulse-off time) in the context of dimensional accuracy such as metal removal rate (MRR), surface roughness, etc.

Experiment

Fabrication of P/M Samples

As received Titanium powder (average particle size of 325 mesh, 99% metals basis, Make: Alfa-Aesar) were used as the test material for fabrication through powder metallurgy technique. The metal powders were blended with a binder ACRAWAX (0.01 % by weight) in a drum with a tubular mixer (diameter 40 mm, height 35 mm), at a constant speed of 1500 rpm for 1 hour.

Fig. 1: Die and punch set to fabricate cylindrical preform

Afterwards the mixture of the Ti-particles and binder was poured into a high carbon high chromium steel cylindrical die having 30 mm height, 14.5 mm inner diameter and 90 mm outer diameter, as shown in Fig.1. After pouring, the powder mixture was pressed at 840 MPa pressure in a Universal testing machine (Capacity 400 kN, Model: KUT-40, Sl. No. 2K7/85) as shown in Fig. 2, for 5 min to obtain the green compacts.

Fig. 2 : Universal Testing Machine for preparing the green compacts (Courtesy ARCI, Hyderabad)

The green compacts were subsequently preheated at 400˚C in a nitrogen atmosphere to remove the binder ACRAWAX in a floor-stand quartz made tubular furnace (hot zone diameter 75 mm, hot zone length 150 mm and maximum temp 1000˚C). The samples were preheated to 400˚C with 5˚C/min heating rate, thereby holding at 400˚C for 2 hours and then cooled in a furnace under nitrogen atmosphere to remove the ACRAWAX completely from the samples.

The binder-free green compacts were later on sintered in an Electric Resistance Batch type Vacuum Furnace (working space dimensions: width-100 mm, length-300 mm & height-100 mm; Sl. No.CHB3-1.3./20H2) as shown in Fig. 3, upto a temperature of 1450˚C in 0.001mbar (7.6x10-4 Torr) vacuum to avoid oxidation. The sintering parameters are shown in Table 1.

Fig. 3 : Electric Resistance Batch-type Vacuum Furnace (Courtesy ARCI, Hyderabad)

Table 1: Sintering parameters

Operation	Temperature from	Temperature to	Duration
Heating	Ambient 30˚C	550˚C	55 min
Soaking	550˚C	550˚C	60 min
Heating	550˚C	1450˚C	80 min
Soaking	1450˚C	1450˚C	30 min
Furnace cooling	1450˚C	Ambient 30˚C	120 min

Experimentation Plan

The machining of the sintered PM samples were carried out on JOEMARS CNC Wire-cut EDM machine (Model: WT 355, Sl. No. 1050594) as shown in Fig. 4. Machining parameters (fixed and variable) of Wire-cut EDM are given Table 2.

Fig. 4: CNC Wire-cut EDM at MSME Tool Room, Kolkata

Table 2 : Machining parameters (fixed and variable) of Wire-cut EDM

Fixed Parameters	Value	Variable Parameters	Working Range	Value
Wire Electrode material	Brass wire of 0.25 mm dia	Open Circuit Voltage	0-15 V	8 V
Spark gap	0.05 mm	Arc On Voltage	1-19 V	5 V
Wire feed	9 m/min	Arc Off Voltage	8-50 V	8 V
Di-electric fluid	De-ionised water	Wire Tension	0-15 kg	10 kg
Workpiece material	CP-Ti P/M components	Water Pressure	0-7 kg / cm^2	6 kg / cm^2
Workpiece dia.	14 mm	Feed sensitivity	0-99 V	50 V
Workpiece thickness	7 mm	Servo Voltage	25-150 V	60V

During machining, the metal removal rate (MRR) of all the samples was measured. Surface roughness (R_a values) of the samples was also measured in a stylus-type profilometer Talysurf (Taylor Hobson Surtronic 3+) as shown in Fig.5.

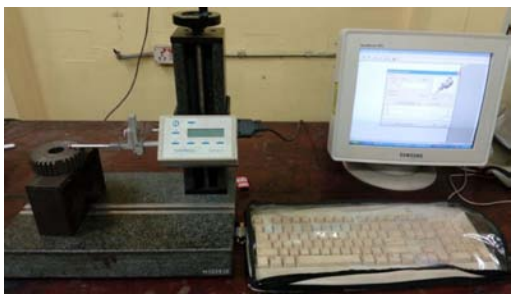

Fig. 5 : Taylor Hobson Surface Roughness Tester at Metrology Lab, JU

Design of experiments (DOE)

Response surface methodology or RSM is a combination of mathematical and statistical techniques, which is useful for modeling and analysis of problems, by which a response of interest is influenced by several variables and its objective is to optimize the response [11]. In this case we wish to find the levels of sintering temperature (x_1), pulse-on time (x_2) and pulse-off time(x_3) that minimize the surface roughness of the WEDM process, which can be expressed as:

$$y = f(x_1, x_2, x_3) + \varepsilon \quad (1)$$

where, y is the output or response and x_1, x_2, x_3 are the process or input variables influencing the output and ε represents the noise or error in the response y.

Box–Behnken designs are experimental designs for response surface methodology, formulated by George Box and Donald Behnken in the year 1960. In this case, each factor, or independent variable, is placed at one of the three equally spaced values, usually coded as -1, 0, +1. Box-behnken design has fewer design points, for this reason, they are less expensive to run than central composite designs with same number of factors.The design is sufficient to fit a quadratic model, that is, one containing squared terms and products of two factors, usually a second-order model utilized in RSM. The equation may be given as:

$$y = \beta_0 + \sum_{i=1}^{k} \beta_i x_i + \sum_{i=1}^{k} \beta_{ii} x_i^2 + \sum_{i<j} \beta_{ij} x_i x_j + \varepsilon \quad (2)$$

where x_1, x_2, x_3,…, xk are the input variable factors which influence the response y; β_0, β_{ii},….. β_{ij}, in which (i=1, 2, …, k), and (j=1,2, …, k) are the unknown parameters and ε is a random error, which is negligible for the present case. The different levels of the control variables, chosen for Box-Behnken Design have been illustrated in Table 3.

Table 3 : Levels of variables chosen for Box-Behnken Design

Parameters	Unit	Symbol	Level		
			Low	Medium	High
			-1	0	1
WEDM Pulse on time	μs	N	6	8	10
WEDM Pulse off time	μs	F	9	11	13
Sintering temperature	°C	T	1350	1400	1450

Based on the proposed 2nd order polynomial model, the effects of the process variables on the MRR and surface roughness were determined

by calculating the values using MINITAB-16 software, as shown in Table 4 and Table 5 respectively.

Table 4 : Box-Behnken Design layout and experimental results for Metal Removal Rate

Run Order	Coded Factors			Actual Factors			Actual Response	Predicted Response
	N	F	T	Pulse-on time (N)	Pulse-off time (F)	Sintering Temp. (T)	MRR (Actual) (mm^3/s)	MRR (Predicted) (mm^3/s)
1	-1	-1	0	6	9	1400	5.76	5.538
2	0	0	0	8	11	1400	7.996	7.42
3	1	0	1	10	11	1450	8.55	8.461
4	0	-1	1	8	9	1450	6.969	6.579
5	-1	1	0	6	13	1400	6.774	7.02
6	0	0	0	8	11	1400	7.15	7.42
7	-1	0	-1	6	11	1350	6.169	6.379
8	-1	0	1	6	11	1450	5.986	6.179
9	0	1	1	8	13	1450	7.551	8.061
10	0	1	-1	8	13	1350	9.049	8.26
11	1	-1	0	10	9	1400	7.674	7.82
12	0	-1	-1	8	9	1350	6.948	6.779
13	1	1	0	10	13	1400	9.903	9.301
14	1	0	-1	10	11	1350	7.688	8.66
15	0	0	0	8	11	1400	7.13	7.42

Table 5 : Box-Behnken Design layout and experimental results for Surface Roughness

Run Order	Coded Factors			Actual Factors			Actual Response	Predicted Response
	N	F	T	Pulse on time (N)	Pulse off time (F)	Sintering Temp. (T)	(Ra Value)	(Ra Value)
1	-1	-1	0	6	9	1400	2.41	2.5996
2	0	0	0	8	11	1400	2.64	2.7033
3	1	0	1	10	11	1450	2.85	2.7533
4	0	-1	1	8	9	1450	2.72	2.6496
5	-1	1	0	6	13	1400	2.72	2.4946
6	0	0	0	8	11	1400	2.75	2.7033
7	-1	0	-1	6	11	1350	2.77	2.6533
8	-1	0	1	6	11	1450	2.49	2.4408
9	0	1	1	8	13	1450	2.36	2.5446
10	0	1	-1	8	13	1350	2.7	2.7571
11	1	-1	0	10	9	1400	3.03	2.9121
12	0	-1	-1	8	9	1350	2.76	2.8621
13	1	1	0	10	13	1400	2.72	2.8071
14	1	0	-1	10	11	1350	3.04	2.9658
15	0	0	0	8	11	1400	2.59	2.7033

Results & Discussion

Developed Mathematical Model for Metal Removal Rate (MRR) and surface roughness (R_a)

The mathematical relationship relating the Metal Removal Rate (MRR) and the process variables under consideration, namely sintering temperature (T), pulse-on time (N) and pulse-off time (F), is obtained as follows:

$$MRR = 7.425 + 1.141N + 0.741F - 0.10T - 0.214N^2 + 0.317F^2 - 0.113T^2 + 0.304NF + 0.261NT - 0.38FT \quad (3)$$

And, the mathematical relationship relating the surface roughness (R_a) and the process variables, for example, sintering temperature (T), pulse-on time (N) and pulse-off time (F), is shown below:

$$R_a = 2.66 + 0.156N - 0.053F - 0.106T + 0.106N^2 - 0.046F^2 + 0.021T^2 - 0.155NF + 0.023NT - 0.075FT \quad (4)$$

Optimizing Parameters

Effects of sintering temperature (while formation of the P/M product) and pulse-on time & pulse-off time (while machining at Wire-cut EDM) on the metal removal rate (MRR) is indicated graphically in Figures 6 and 7 as surface plots. Fig. 6 indicates that for a fixed value of pulse-off time, metal removal rate (MRR) decreases as pulse-on time decreases & vice-versa and it remains more or less invariant with sintering temperature. From Fig. 7, we can infer that, for a given value of pulse-on time, MRR increases with increasing pulse-off time, but it remains approximately unchanged with sintering temperature. Hence, the best metal removal rate (MRR) is found to be related with highest pulse-on time and pulse-off time. Moreover, MRR is not significantly related to sintering temperature. A comparative study of the predicted response versus actual response is illustrated in Table 4.

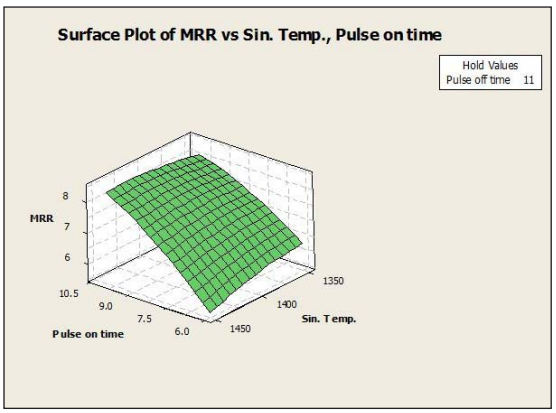

Fig. 6 : Surface Plot of MRR w.r.t.sintering temperature and pulse-on time

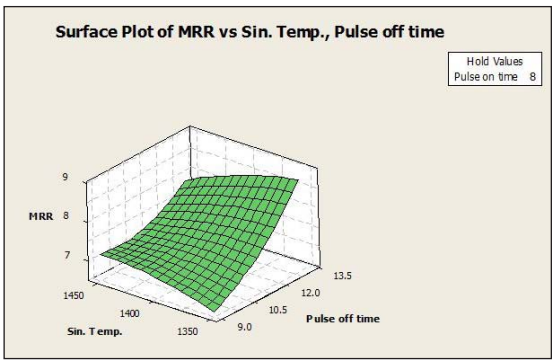

Fig. 7 : Surface Plot of MRR w.r.t.sintering temperature and pulse-off time

Moreover, the effects of sintering temperature, pulse-on time and pulse-off time on surface roughness (R_a value) is indicated graphically in Figures 8, and 9 as surface plots. Fig. 8 indicates that, for a fixed value of pulse-off time, surface roughness decreases as sintering temperature increases and pulse-on time decreases. In addition to that, for a given value of pulse-on time; an increasing pulse-off time and increasing sintering temperature, decreases the surface roughness (R_a) value, which is conclusive from Fig. 9. Hence, the best surface finish is found to be related with highest sintering temperature, highest pulse-off time and lowest pulse-on time. A comparative study of the predicted response versus actual response is illustrated in Table 5.

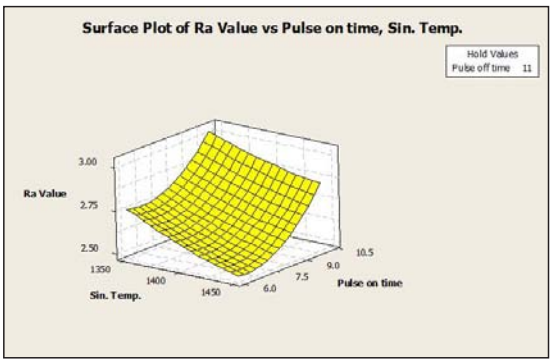

Fig. 8 : Surface Plot of Surface Roughness parameter (Ra value) w.r.t.sintering temperature and pulse-on time

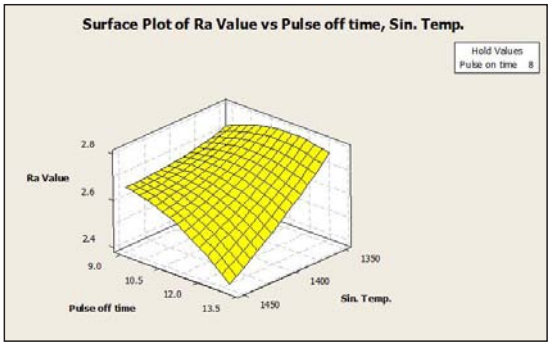

Fig. 9 : Surface Plot of Surface Roughness parameter (Ra value) w.r.t.sintering temperature and pulse-off time

Micro-structural Examination and XRD Analysis

After Wire-cut EDM, the samples were examined in a Scanning Electron Microscope (Make-JEOL, Sl. No.JSM-6360) at 500X and 1000X magnifications respectively, as shown in Fig. 10. The SEM images indicate certain craters (marked 1), pockmarks (marked 2), voids (marked 3) and micro-cracks (marked 4). These carters, pockmarks and micro-cracks have been formed due to the variation of spark voltage and pulse duration, whereas voids were present since the initial formation of the metal from Ti-powders. Voids are helpful in bio-materials for propagation of tissue growth inside the implants.

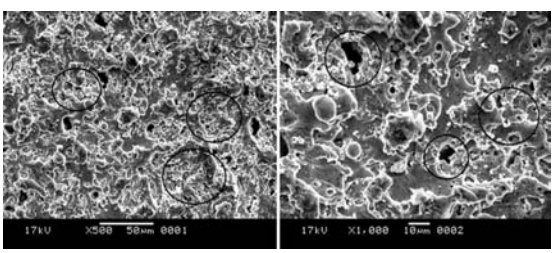

Fig. 10 : SEM micrograph at 500X and 1000X respectively of Cp-Ti P/M sample after WEDM at conditions of Run No.4 (i.e., pulse-on time=8 µs, pulse-off time=9 µs and Sintering temperature=1450°C)

X-Ray Diffraction analyser (Rigaku, Ultima III) using Cu (40 kV, 30 mA) radiation is used to study the phase transformation of Ti P/M samples during Wire-EDM. The XRD plots are shown in Fig. 11. The highest peak is at 2θ value 43.196°. Moreover, due to machining by brass electrode wire, elemental Copper (Cu) is observed at 2θ value 75.253°. Some titanium oxide is also formed at the machined surface, which resulted during machining at high temperature with a di-electric fluid like de-ionised water.

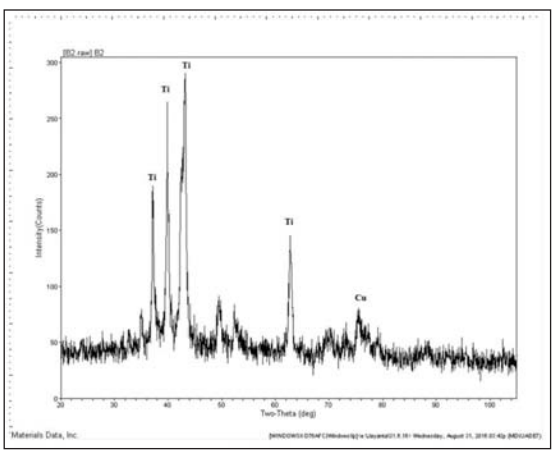

Fig. 11 : XRD analysis of Cp-Ti P/M sample after WEDM at conditions of Run No.4 (i.e., pulse-on time=8 µs, pulse-off time=9 µs and Sintering temperature=1450°C)

Conclusions

In the present research work, the quadratic models for Metal Removal Rate and Surface Roughness have been developed to correlate the dominant sintering and machining parameters such as sintering temperature, pulse-on time and pulse-off time in the WEDM process of commercially pure titanium powder metallurgy components. An experimention plan of the Box–Behnken Design based on Response Surface Methodology has been applied to perform the experiment. Machinability evaluation in the WEDM process has been analyzed according to the developed mathematical models to obtain the following conclusions:

1. Wire-cut EDM is an adequate technique to machine high strength temperature resistant commercially pure titanium with good surface finish and dimensional accuracy.

2. The obtained range of metal removal rate (MRR) of pure titanium powder metallurgy components lies within the range of 5.76mm3/sec to 9.903mm3/sec by Wire-EDM process. The maximum metal removal rate was achieved under the conditions of 10 µs pulse-on time, 13 µs pulse-off time and at a sintering temperature of 1400 °C.

3. The minimum surface roughness was achieved with the conditions of 8 µs pulse-on time, 13 µs pulse-off time and sintering temperature (used during the formation of CP-Titanium P/M components) of 1450 °C.The surface roughness (Ra) of pure titanium powder metallurgy components obtained lay in the range of 2.36 µm to 3.04 µm by Wire-cut EDM process.

Acknowledgements

Authors thankfully acknowledge the financial support provided by C.S.I.R., New Delhi under Major Research Project Grant [Sanction letter No. 22(0587) /12 / EMR-II dated 02.04.2012] without which this work could not be attempted.

References

[1] F.H. Froes and D. Eylon, Powder Metallurgy of Titanium Alloys, Int. Mater. Rev. 35 (1990)162

[2] C. N. Elias, J. H. C. Lima, R. Valiev, M. A. Meyers, Biomedical applications of titanium and its alloys, J. of the Min. Met. & Mat. Soc. 60 (2008) 46-49.

[3] W. Chen, Y. Yamamoto, W.H.Peter, M.B.Clark, S.D.Nunn, J.O.Kiggans, T.R.Muth, C.A.Blue, J.C.Williams, K. Akhtar, The investigation of die-pressing and sintering behaviour of ITP CP-Ti and Ti-6Al-4V powders, J. Alloys Compd. 541, Elsevier USA (2012) 440-447.

[4] A.Kumar, V.Kumar, J.Kumar, Prediction of Surface Roughness in Wire Electric Discharge Machining (WEDM) Process based on Response Surface Methodology, Int. J. Eng. Technol. 2(4), 708-719 (2012)

[5] A.Kumar, V.Kumar, J.Kumar, Multi-response optimization of process parameters based on response surface methodology for pure titanium using WEDM process, Int J Adv Manuf Technol 68 (2013) 2645–2668.

[6] D. S. Badkar, K. S. Pandey, G. Buvanashekaran, Development of RSM- and ANN-based models to predict and analyze the effects of process parameters of laser-hardened commercially pure titanium on heat input and tensile strength, Int J Adv Manuf Technol 65 (2013)1319–1338.

[7] M. Manjaiah, S. Narendranath, S. Basavarajappa, V. N. Gaitonde, Wire electric discharge machining characteristics of titanium nickel shapememory alloy, Trans. Nonferrous Met. Soc. China 24 (2014) 3201−3209.

[8] M.M. Rahman, Md. A. R. Khan, K. Kadirgama, M.A. Maleque, R. A. Bakar, Parametric Optimization in EDM of Ti-6Al-4V using Copper Tungsten Electrode and Positive Polarity: A Statistical Approach, Mathematical Methods and Techniques in Engineering and Environmental Science, 13th WSEAS Conference Proceedings (2011) 24-29.

[9] Farnaz Nourbakhsh, K. P. Rajurkar, A. P. Malshe, Jian Cao, Wire electro-discharge machining of titanium alloy, Proceedings of the First CIRP Conference on Biomanufacturing, Procedia CIRP 5 (2013)13 – 18.

[10] M.P. Garg, A. Jain, G.Bhushan, An Investigation of Wire Electric Discharge Machining of High Temperature Titanium Alloy, Proceedings of the 5th International & 26th All India Manufacturing Technology, Design and Research Conference (AIMTDR 2014) IIT Guwahati, Assam, India.

[11] D.C.Montgomery, Design and Analysis of Experiments, 7th edition, Wiley, India. 2009.

POWDER METALLURGICAL ROUTES TO MAKE PARTS FOR MAGNETIC APPLICATIONS

Kalathur Narasimhan

P2PTechnologies
Moorestown, NJ, U.S.A.

Abstract : Powder metallurgy has made great strides over the past 60 Years as a lower cost alternate to Stamping, forgings and machined parts. Iron powder, iron alloyed with Phosphorus, Silicon and stainless steel powders are used in soft magnetic applications. Although PM is a net shape process certain post sintering operations are necessary. The effect of these processing on magnetic properties is discussed in this manuscript. Permanent magnets processed by PM route are discussed as well for traction motors in hybrid vehicles.

Key words: Soft Magnets, Cold work, Annealing

Introduction:

Powder metal usage in automobiles is constantly increasing and is at about on the average 23 kilos/ vehicles in North America. The drive for replacing mechanical systems to electromagnetic systems continues to increase. Exhaust gas recirculation (EGR) uses Iron powder part for magnetic actuation to open and close the EGR valve, fuel pump actuation, armature for electronic control of rear wheel drive transmission, hydraulic rocker arm, antilock braking systems. Steering wheel sensor, flux return paths for disc drives, to name a few of the applications, Sensor usage is increasing and magnetic iron parts are used in these applications.

Number of publications on the properties of iron and iron alloys for magnetic applications is in the literature (Ref 1-6).

Magnetization Process:

Hysteresis loop describes the magnetic properties of both soft and hard magnetic materials (figure1). A sintered soft magnetic iron compact or neodymium iron boron permanent magnet is in a fully demagnetized condition, the domains in a grain is all randomly oriented with net magnetization of zero. On the application of field (see Fig2.) The domain wall moves in the direction of applied field and at full saturation domain wall is completely removed, Fig2. On applying a reverse field at a certain value of the reverse field domains is renucleated and is completely removed with increase in reverse field as shown in the third quadrant of hysteresis curve. Reversing the field again we travel through the third quadrant and at certain value in the fourth quadrant domain walls are renucleated and removed completely in the first quadrant. The field at which the domains nucleate depends on the anisotropy constant K1 which in the case of pure cubic iron is very small, 4.8×10^5 erg/cm^3 compared to > 550×10^7erg/ cm^3(ref5) for permanent magnets which are of hexagonal or tetragonal symmetry. The domains in cubic iron reverse easily at very low applied fields and the hysteresis loop below shows the remanent induction and coercive force are all small. In the case NdFeB magnets or samarium cobalt magnets both remanent induction and Coercive are very high. (Fig 1, definition of magnetic terms)

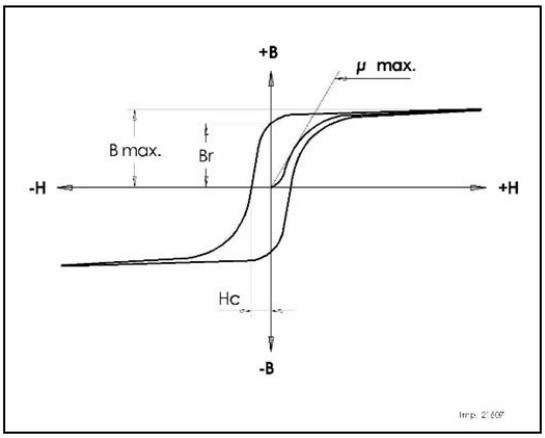

Fig. 1: μmax is maximum permeability is the tangent of the slope of the magnetization curve, Br is remnant induction at zero value of the applied field, B max is saturation induction often specified at a value of applied field, HC is the coercive force value of applied filed at zero induction.

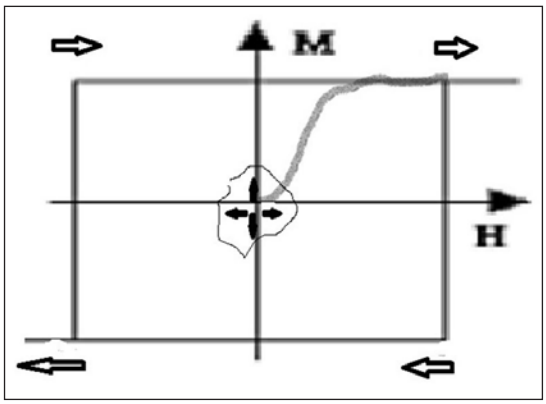

Fig. 2: Magnetization and demagnetization process in magnetic material

Soft magnetic materials have very low coercive field often less than 4Oe (Figure 3) and permanent magnets have as high as 13,000Oe(Figure 4).Rapid magnetization and demagnetization is possible with soft magnetic materials,a property used in transformers.

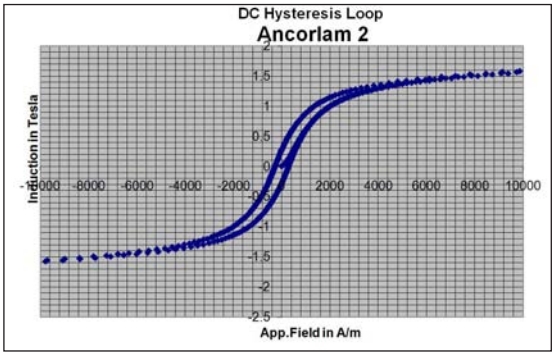

Fig. 3: Hysteresis loop of a soft magnetic material

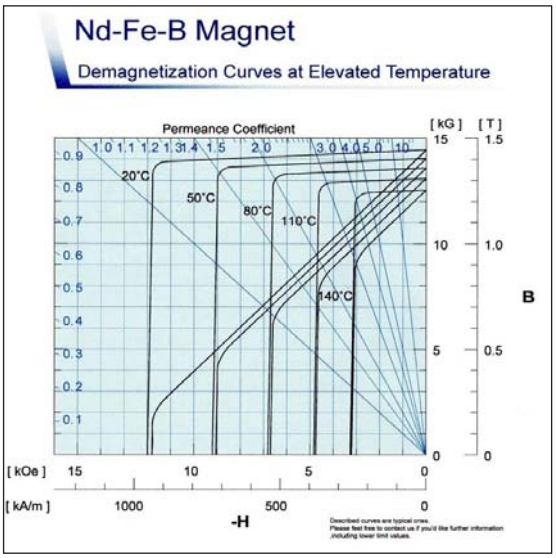

Fig. 4: Demagnetization (second quadrant of hysteresis loop) curves for Neodymium iron boron magnet. (Shi-etsu Chemicals, ref 7)

In any electromagnetic application, there is a magnetic field generated by electromagnet or by permanent magnet. The magnetic flux generated is conducted through a soft magnetic material to complete the direct current magnetic circuit using low carbon iron or by a powder metal processed compact made from powders of Fe or Fe-Si, or Fe-Ni or Fe-Co or by magnetic stainless steel (Ferritic stainless) powder. In A.C circuits lamination steel made from Fe-1Si

A familiar example of PM soft magnetic parts is in voice coil motors that areused in disk drives,(Figure 5.).

Magnets are attached to PM housing and combination with high energy magnets provide very fast access time for read write heads in disk drives.,

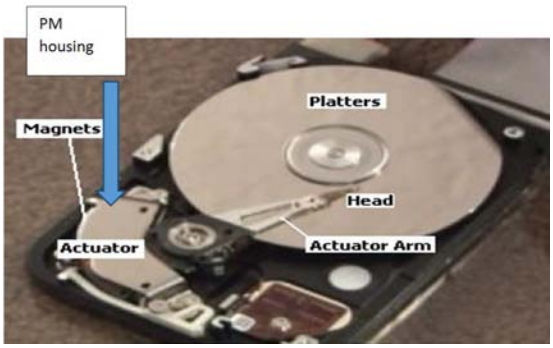

Fig. 5: Disk drive with PM housing and NdFeB magnets, ref 12

Soft magnetic Irons:

High purity water atomized iron powder is used for most applications although sponge iron powder is also used. Generally residual impurities are below 0.2% with carbon level of less than 0.02%.At these carbon levels compacts made pure iron powder like Ancorsteel 1000C after sintering in non-oxidizing atmosphere and cooling results in soft ferrite phase. Alloying with Ferro phosphorus to produce 0.45 and 0.80phosphorus in solution in iron improves the magnetic properties. Similarly, ferrosilicon is added to produce Fe-3%silicon.The addition of ferrosilicon requires high temperature sintering typically about 1200C or higher. Ferritic stainless powders are also used in magnetic applications by high temperature sintering for flux return paths. Permalloy 50Fe:50Ni is sintered product, requires careful processing. Magnetic properties of typical soft magnetic sintered compacts are shown in Table 1. (Ref 1, 10)

Table 1. Magnetic properties of soft magnetic sintered compacts. Included is Soft magnetic composite, AncoLam2, which is pressed and cured and not sintered,

Material	Density (g/cm³)	Hc (A/m)	Bm (T)	Br (T)	Max Permeability (μmax)	Tensile Strength MPa	Resistivity (μΩcm)
Iron	7.0	165	1.05	0.90	2,100	220	14
	7.2	145	1.20	1.10	2,900		12
Iron 0.45%P	7.0	145	1.15	0.90	2,600	405	21
	7.4	120	1.35	1.10	3,600		20
Iron 0.8% P	7.0	120	1.20	1.10	4,000	500	30
	7.4	105	1.35	1.30	5,000		28
Iron 3% Si	7.0	95	1.20	1.00	4,000	320	50
	7.4	70	1.40	1.20	6,000		48
50Ni:50 Fe	7.5	25	1.20	0.90	10,000	560	45
Ferritic Stainless	7.35	165	1.07	0.88	2,000	400	45
AncorLam2*	7.6	246	1.6	0.38	610	90**	>500

*Non Sintered, Pressed and cured, **TRS

Sintered iron powder and iron-phosphorus alloy powders compete favorably with low carbon steel for variety of applications, for circuits that are excited by permanent magnets, dc or low-frequency (< 10 Hz) pulsed current applications. Silicon-irons are suitable for circuits that are excited by slightly higher frequency alternating or pulsed current. 50Fe:50Ni materials are used in circuits that are excited by very low currents and for applications where a very quick response is needed. Fe-3Si and 50Ni-50Fe are also used in pulsed DC applications; the higher resistivity reduces the Eddy current heating Ferritic stainless steels are used for applications where magnetic properties are less important than good corrosion resistance

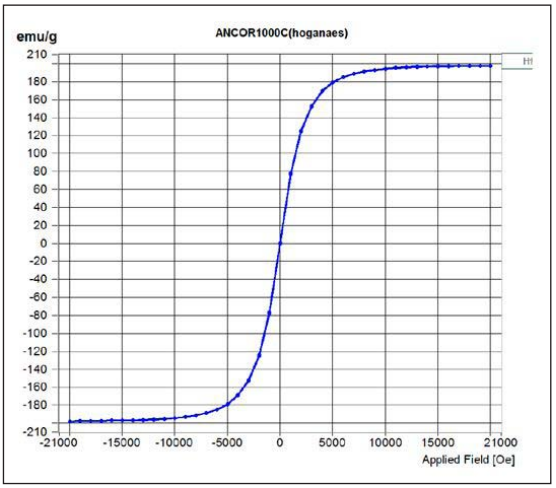

Fig. 6: Hysteresis loop on Ancorsteel 1000C powder. Courtesy of Malobika Karanjia of DRL.

Coercive force is 3.88Oe or 308kA/m^3 and saturation magnetization is 197.786 emu/gm. was measured on pure iron powder uncompacted using a vibrating sample magnetometer, Fig.6. The high coercive force observed is due to cold work induced in the powder in the crushing operation after annealing. Once the powder is compacted and cured coercive force drops to 2.0 Oe or 165kA/m^3. Sintered soft magnetic materials are often machined or tumbled to clean or calibrated by a restrike operation to achieve tolerances, these results in dislocations in the crystal lattice. These dislocations interfere with domain wall motion. The induction achieved at a given applied field will be lower after the post processing of sintered compacts due to these dislocations. To understand better this phenomenon, we need to understand the magnetization process. As discussed earlier. Initial magnetization process involves domain wall motion and rotation. In the presence of dislocations or strains, defects in general, additional field is required to move the domain walls past these defects. This results in lower values of induction for a given applied field. The severe the cold work the worst is the saturation. Annealing the compact is necessary. During annealing of strained material recovery normally occurs at about 600°C providing partial relief and between 600°C to 700°C recrystallization leading to stress free grains and above 700°C grains grow leading to easy movement of domain walls leading to increase in permeability. Extent of cold work will influence the time and temperature for recovery. Such a phenomenon has been reported on iron strained and annealed. Figure 7.

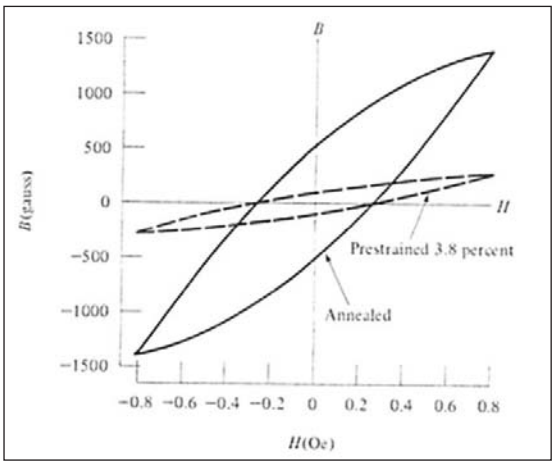

Fig 7: Effect of cold work on ironhysteresis (ref 8)

Work done by Hanejko et.al, Ref 9, is useful in assessing the temperature onset of recrystallization. They studied on iron powder pressed and heated at various temperatures, Figure 8. At about 1200°F or 650°C recovery and recrystallization begins withan increase in permeability.

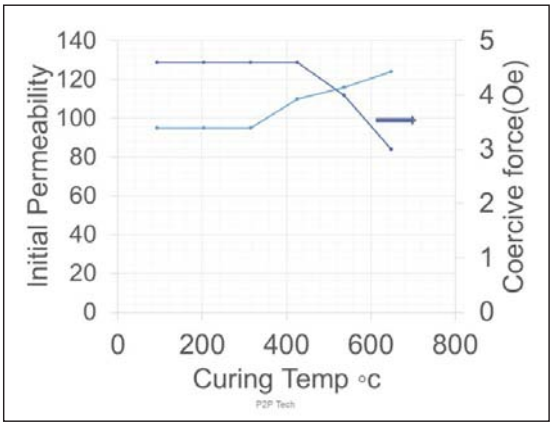

Fig. 8: Effect of annealing on permeability and coercive force of compacted iron. Ref 9

Narasimhan and Schade have shown that at about 800°C anneal, figure 9, is required to reduce core loss of Fe-3Si prealloyed powder compacted at 800MPa.

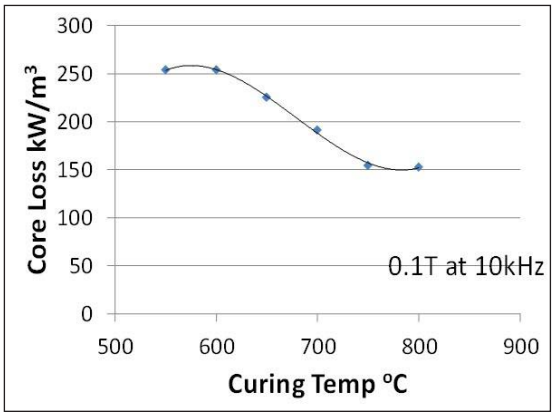

Fig. 9: Effect of curing temperature on Core loss of compacted Fe-3Si with an insulated coating on individual particles ref 10

Generally, recrystallization temperature is typically at 1/3 to 1/2 of the melting temperature (can be as high as 0.7 Tm in some alloys). The recrystallization temperature decreases as the cold work is increased. Below a "critical deformation", recrystallization does not occur. Donaldson and Hanejko, Ref 11, as shown in Table 2, the compacted parts at 7.15 g/cm^3 with Ancorsteel 45P (Trade name for Hoeganaes corporation Fe-0.45P powder), sintered at 1120°C, then sized to 7.20 g/cm^3. Themagnetic properties were tested as a function of time at 815 °C temperature. The results are shown in Figure 10. Longer time at temperature is helpful in recovering the magnetic properties.

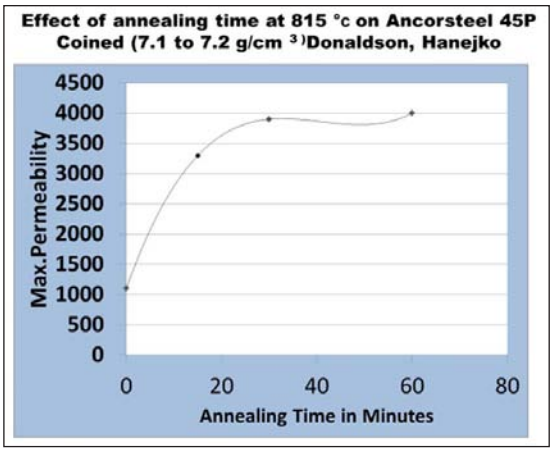

Fig. 10: Effect of annealing time on recovery in Fe-.45P sintered compacts, sized. (Ref 11)

Steam treatment of soft magnetic parts also affects the permeability and induction. The effect is not as severe as repressing. During steam treatment, generally at 550°C iron oxide is formed on the surface and parts have small growth. Interconnected pore closure and surface pore closure takes place and compressive stresses increase. The compressive stresses are likely to be responsible for the alteration in magnetic properties.

Table 2. Steam Treatment Effecton 45P at 7.2g/cm^3 Measured at 1195A/m Drive Field (Ref 11)

Condition	Max.Permeability	HC(A/m)	Induction(T)
As-Sintered	3250	125.0	1.306
SteamTreatment	2660	136.1	1.212

Shah and Samal studied effect of recovery on stainless steel sensors used in anti-locking braking system(ABS) applications (ref 12) as shown in Table 3.

Table 3. Effect of cold work and annealing on the magnetic properties of PM 410L (Ref 12)

Condition	Sintered		Repressed		Annealed	
Density, g/cm3	7.07		7.38		7.37	
Applied field, kA/m	1.19	1.99	1.19	1.99	1.19	1.99
Maximum Induction, Bm Tesla	1.052	1.114	0.422	0.629	1.115	1.181
Retentivity, Br, Tesla	0.716	0.724	0.267	0.371	0.783	0.792
Br/Bm	0.681	0.65	0.633	0.59	0.702	0.671
Coercive field, Hc, A/m	121	122.	595	712	127	129
Maximum permeability, μmax	2110	2100	280	280	2260	2270
1.Sintered in pusher furnace at 1260C (2300 F), 45 min, H2, dew point -35C (-31F), repressed at 690MPa, annealed at900C,45minutes, H2 dew point -35C						

More detail studies on cold work and recrystallization effects by varying time and temperature and using microscopy could lead to optimum annealing time and temperature for each post sintering step.

Summary

Powder metallurgical process is very effective in making parts that are used in electromagnetic applications. Fe, Fe-P, Fe-Si, Fe-Ni, Stainless steel powders are pressed and sintered to make these parts. Properties of these materials is presented. Major application for these parts are in D.C. and pulsed DC applications, mostly for magnetic flux paths in sensors, actuators, motors. Post sintering operations of soft magnetic parts results in cold work which require annealing. More research is needed in understanding the nature of cold work and optimal annealing temperatures.

References:

1. Kalathur S. Narasimhan" Magnetic Materials and properties for powder metallurgy part application's Hand book, volume7, Powder Metallurgy, 737-754, Edited by P. Samal and J. Newkirk, ASM International, MaterialsPark, Ohio 44073-002,2015

2. H. G. Rutz, F. G. Hanejko, and G. W. Ellis, "The Manufacture of Electromagnetic Components by the Powder Metallurgy Process", Advances in Powder Metallurgy and Particulate Materials 1997, 18-23. Metal Powders Industry Federation, Princeton, NJ.

3. C. Lall, Fundamentals of Magnetism, Chapter I, Soft Magnetism,1992, 1–27, Metal Powder Industries Federation,

4. M. J. Dugan, J. Morato, "Sintered Soft Magnetic Materials for Low-and High-Frequency Applications", Advances in Powder Metallurgy and Particulate Materials – 2004, 205-212,Metal Powders Industry Federation, Princeton, NJ,

5. Kalathur S. Narasimhan, Michael L. Marucci and Christopher Schade; "Advancements in Insulated Powder Composites for Soft Magnetic Applications Advances in Powder Metallurgy and Particulate materials, 2012, 1043-1050, MPIF, Princeton, NJ

6. Narasimhan, K. S, Kasputis, D.J. Lynn, J.C." Processing of Ferro-phosphorus containing mixes in low hydrogen atmospheres" Advances in Powder Metallurgy and Particulate Materials -2002, Vol.14, 132-137. MPIF Princeton, NJ

7. Shin-Etsu Magnetics, 909 Park Ave Blvd. Lombard, Illinois 60148, product brochure on Neo magnets.

8. B.D. Cullity, Introduction to Magnetic Materials, Addison-Wesley, 1972. 352

9. Fran Hanejko and George Ellis: U.S Patent 6635122 B2, October2003" Method of making and using annealable metal based insulated powder particles"

10. Kalathur S Narasimhan and Christopher Schade," Iron-Silicon water atomized powders for electromagnetic applications" Advances in Powder metallurgy and Particulate materials, Orlando,2014, 1917-1927; MPIF Princeton, NJ,

11. S. O. Shah, P. K. Samal, and E. Klar, "Properties of 410L PM Stainless Steel Antilock Brake Sensor Rings", SAE Paper No. 930449, SAE International Congress & Expo., (Detroit, Michigan), March 1993.

SYNTHESIS AND CHARACTERISATION OF COMPOSITE ELECTROLYTE MATERIAL FOR IT-SOFC

M. Gautam[1], A. Ahuja[1], J. Sharma[2], Amit Sinha[2*], A. Venkatasubramanian[1] and P. K. Sinha[2]

[1] School of Energy and Environment, Thapar University, Patiala, Punjab ,India
[2]Powder Metallurgy Division, Bhabha Atomic Research Centre, Navi Mumbai ,India

Abstract : Novel composite electrolyte materials based on gadolinium doped ceria (GDC,$Ce_{0.85}Gd_{0.15}O_{2-\delta}$) and x mol % gadolinium doped strontium cerate (SGO, $SrCe_{0.85}Gd_{0.15}O_{3-\delta}$) (x=10, 15 and 20) was developed for an intermediate temperature solid oxide fuel cell (IT-SOFC). The composite powders GDC-10SGO, GDC-15SGO and GDC-20SGO were synthesized through glycine-nitrate auto-combustion route that provides the desired phase right after combustion. The XRD pattern of as produced powder indicates two phases of GDC and SGO. Scanning electron microscopy (SEM) reveals the composites are denser than pure GDC. The variation in the total conductivity was explained for all composite electrolytes at the intermediate temperature range whereas activation energy for GDC-10SGO and GDC-15SGO samples was calculated in the temperature range of 450-800 °C.

Keywords: Composite electrolyte, Strontium cerate, activation energy, total conductivity

1. Introduction

Solid oxide fuel cell can directly convert chemical energy of fuel into electricity and operates at a higher temperature range of 800-1000°C. High temperature SOFCs are mostly used in stationary power generation but it has many drawbacks associated with the high operating temperature. Consequently, the recent research and development focuses on intermediate temperature solid oxide fuel cells (IT-SOFCs) in the operating temperature range of 600-800 °C [1]–[4].

Cathode, anode and electrolyte are the three mandatory components of a single SOFC. If the stack is considered then sealant and interconnect also play vital role. In SOFC, electrolyte is used for ions migration from cathode to anode. The important properties of the electrolyte material in SOFC are higher sintered density, higher ionic conductivity and negligible electronic conductivity. At intermediate temperature range, doped ceria based electrolyte material such as gadolinium doped ceria (GDC), samarium doped ceria (SDC) exhibit good ionic conductivity [5][6], [7]. These materials exhibit higher ionic conductivity at intermediate- lower temperature range of 500-800°C. However, these materials exhibit additional electronic conductivity at higher operating temperature due to reduction of Ce^{+4} into Ce^{+3} at anodic reduction condition. Hence there is a drop in open circuit voltage (OCV) accompanied by a diminished performance of fuel cells [8].

Rare earth doped barium cerate ($BaCeO_3$) has been widely investigated as electrolyte materials for their high ionic and protonic conductivity in the temperature range of 300-1000°C. For Gd doped $BaCeO_3$ electrolyte material, the reported ionic conductivity was 11 $mScm^{-1}$ and 16 $mScm^{-1}$ at 600 and 800 °C respectively [9].

Composite electrolyte materials exhibit protonic and ionic conductivity in the temperature range of 300- 800°C. To diminish the electronic conductivity and enhancing total conductivity, composite electrolyte material can be substitute for doped ceria and doped barium cerate based

electrolyte materials. In composite electrolyte materials, two phases are present in which one phase exhibits protonic conduction and second one provides ionic conduction. Hence overall conductivity can be maximized by using composite electrolyte materials [10]. Fig. 1 shows the working of the protonic (H^+) and oxygen ion (O^{2-}) conduction in composite materials.

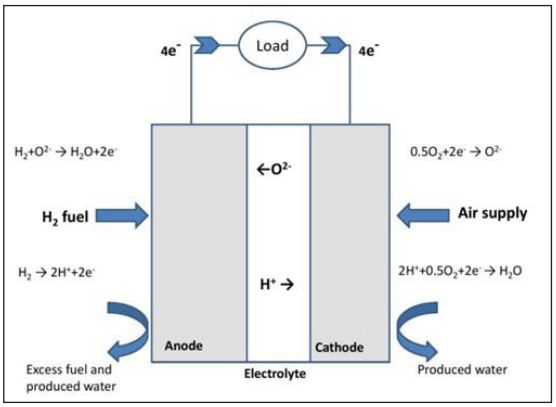

Fig. 1: Schematic diagram of SOFC based on composite electrolyte (reaction mechanism of protonic (H^+) and oxygen ion (O^{2-}) conduction through the composite electrolyte)

Composite electrolyte based on $Ce_{0.85}Sm_{0.15}O_{1.92}$ (SDC) - $BaCe_{0.83}Y_{0.17}O_{3-\delta}$(BCY) was reported by Bin Li [11] with good bulk conductivity at 800°C and the required activation energy was 0.83eV in the temperature range of 300-800 °C.

Rare earth doped $SrCeO_3$ is the class of electrolyte material which exhibit good protonic conductivity below 1000°C [12]. Yb doped $SrCeO_3$ based perrovskite electrolyte was reported by Paul Inge Dahl [13] in which proton conductivity was observed maximum of 5 $mScm^{-1}$ above 900°C. To eliminate the electronic conductivity and enhancing total conductivity (ionic and protonic), doped strontium cerate phase has been incorporated into the doped ceria phase. Predominantly, doped $SrCeO_3$ based electrolyte materials have not gathered attention in commercial market due to their indigent chemical stability and mechanical properties. Furthermore, doped strontium cerate materials exhibit protonic (H^+) conductivity at temperature range of 600-1000°C and it will be conducive for reducing electronic conductivity and enhancing total conductivity [14].

In this present investigation, we have developed a composite electrolyte materials consisting of GDC-SGO in which GDC phase was responsible for ionic conduction (O^{2-}) and SGO phase was responsible for protonic conduction (H^+). This compound can be a class of composite electrolyte material for intermediate temperature fuel cell for stationary power generation which is not reported yet.

2. Experimental work

2.1 Powder synthesis and preparation of samples

The composite powder having a nominal composition of (GDC, $Ce_{0.85}$ $Gd_{0.15}O_{2-\delta}$) and x mol % gadolinium doped strontium cerate (SGO, $SrxCe_{0.85}Gd_{0.15}O_{3-\delta}$) was produced through combustion process starting with reagent grade nitrate solutions of gadolinium, cerium, and strontium in the presence of glycine as fuel. The ratio of the fuel and nitrates was adjusted that lead to auto-combustion upon dehydration of the solution that resulted in production of white powder. To compare the effect of second phase (SGO) on the conductivity of composite electrolyte, pure GDC powder of similar composition was prepared utilising the same process starting from nitrate solutions of cerium and gadolinium. Different compositions for pure GDC15 and GDC-xSGO (x=10, 15, 20) composite electrolyte materials employed in experiment are shown in the table 1.

Table 1: Compositions for the present study

sample	Strontium nitrate (mol fraction, x)	Gadolinium nitrate (mol fraction)	Cerium nitrate (mol fraction)
GDC15	0	0.15	0.85
GDC-10SGO	0.10	0.15	0.85
GDC-15SGO	0.15	0.15	0.85
GDC-20SGO	0.20	0.15	0.85

2.2 Pellets preparation

Green pellets of electrolyte (GDC) and composite electrolytes (GDC-10SGO and GDC-15SGO) were prepared by uni-axial hydraulic pressing at 150Mpa using 15mm diameter tungsten die. Stearic acid and alcohol were used as lubricant and cleaning agent respectively. GDC green pellet was sintered at 1300°C for 4 h whereas GDC-10SGO and GDC-15SGO green pellets were sintered at 1550°C for 4 h with 2°Cm in^{-1} heating rate and 5°Cmin-1 cooling rate. For sintering, alumina plate was used as substrate. After sintering, sintered pellets were cleaned up with 400 grit emery papers for removing foreign dust particles. Sintered density and percentage shrinkage were evaluated for GDC15, GDC-10SGO and GDC-15SGO composite electrolyte pellets using Archimedes principle.

2.3 Characterization of samples

The phase identification of the powders was carried out using XRD [INEL, CPS 120] utilising CuKα radiation. Direct synthesized powders were used for XRD test for pure and composite electrolytes.

The particle size distribution of GDC, GDC-10SGO and GDC-15SGO composite powders was characterised using a particle size analyzer (PSA) [Zetasizer Nano ZS90]. Water was used as dispersant in PSA test. Laser diffraction technique employed in the PSA for calculating the particle size.

SEM [Zeiss EVO 40] was carried out on the sintered pellets for obtaining the morphology and microstructure. Before SEM, sintered pellets were cleaned up with alcohol for removing dust particles.

For electrical characterisation, platinum coating was applied on both sides of sintered pellets. Platinum coated pellets were baked at 950°C for 90 minutes. The electrical properties of the pure and composite electrolytes were carried out using an impedance analyzer [Solartron, Model 1260A] under air in the temperature range of 350 – 800°C and the frequency range was 0.1-10^5Hz. Z-view software was used to analyse the impedance data for all samples. The impedance data was collected during cooling in steps of 50°C.

Arrhenius equation used for evaluating activation energy for given temperature range, mathematically it can expressed by the relation

$$\sigma = \frac{\sigma_o}{T} \exp\left(-\frac{E_a}{kT}\right) \quad (1)$$

Where σ is the total conductivity, σo is the pre exponential factor, T is the temperature in Kelvin, k is the Boltzmann constant and Ea is the activation energy required for conduction of ions through electrolyte.

3. Results and discussion

3.1 Phase analysis

Fig. 2(a) and 2(b) show XRD patterns comparison for GDC15 pure and GDC-10SGO composite electrolyte powders. The pattern exhibits all the reflections corresponding to fluorite phase of $Ce_{0.85}Gd0.15O_{2-\delta}$ (ICDD PDF: 01-081-9326). The result suggests that desired phase could be obtained right after the combustion reaction. XRD pattern of the composite powders, which

shows the peaks corresponding to GDC phase as well as that of $SrCeO_3$ phase (ICDD PDF: 00-047-1689).

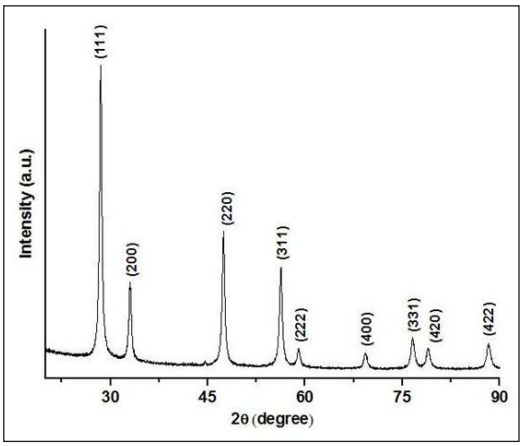

Fig. 2(a): XRD pattern of GDC electrolyte

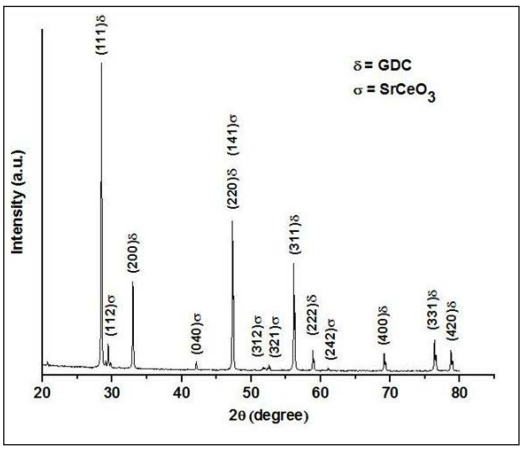

Fig. 2(b): XRD pattern of GDC-10SGO composite electrolyte

3.2 Particle size analysis

Average particle size distribution for GDC15 and GDC-10SGO composite electrolyte are shown in the figures 3. Particle size distribution suggest that, obtained synthesize powders were in the range of nanometres. The average particle size distribution for pure GDC and GDC-10SGO was 352 and 258nm respectively.

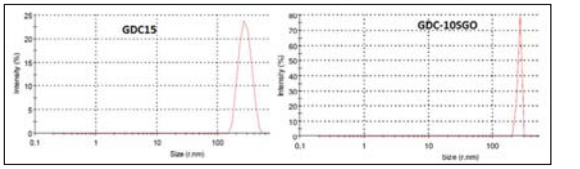

Fig. 3: Average particle size distribution by intensity for GDC15 pure and GDC-10SGO composite electrolyte powders

Sintered density as % theoretical density was evaluated using Archimedes route for GDC, GDC-10SGO and GDC-15SGO electrolyte materials. Evaluated sintered density was more than 95% of theoretical density for pure and composite electrolyte samples. S.D. as % of T.D. is listed in table 2. The sintered temperature for GDC15 was 1300°C whereas, for composite electrolytes, sintered temperature was 1550°C. Theoretical density for GDC and $SrCeO_3$ perovskite (ABO_3) were taken from the JCPDS file data form XRD as reference.

Table 2: Sintered density as % of theoretical density data

Sample	Sintered temperature	S.D. as % of T.D.
GDC15	1300	96.1
GDC-10SGO	1550	97.2
GDC-15SGO	1550	96.5

$T.D._{GDC}$ = 7.2 gm/cm^3 and $T.D._{SrCeO3}$=5.77 gm/cm^3

3.3 Microstructure analysis

SEM images for GDC15 and GDC-10SGO composite electrolyte are shown the Fig. 4(a) and 4(b). It reveals by SEM that composite electrolyte was highly dense than pure GDC15 electrolyte material. The average grain size was 10µm for the GDC-10SGO composite electrolyte.

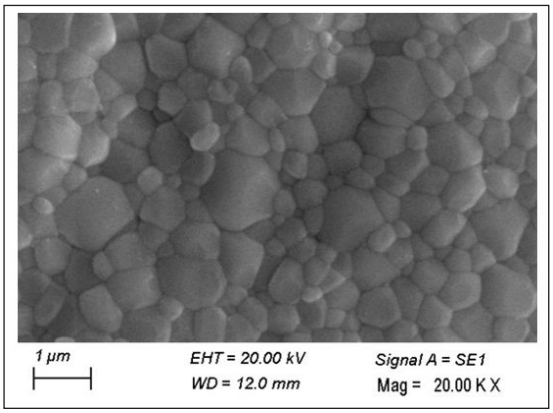

Fig. 4(a) Microstructure analysis of GDC

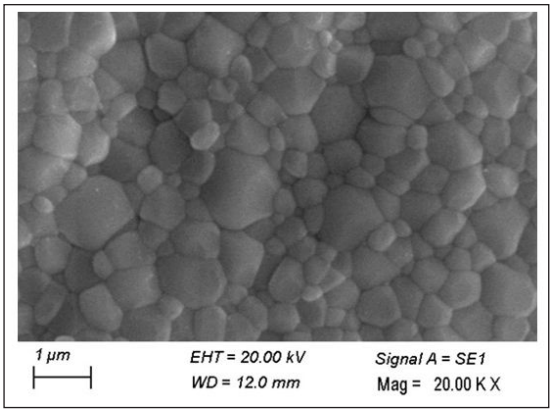

Fig. 4(b) Microstructure analysis of GDC-10SGO

3.4 Total conductivity measurements

The total conductivity comparison at different temperatures was extracted from the impedance data and is listed in the table 3.

Table 3: Total conductivity measurement for the GDC15, GDC-10SGO and GDC-15SGO at intermediate temperature range

Materials	Total conductivity ($mScm^{-1}$)			
	800 °C	750 °C	700 °C	650 °C
GDC15	38.4	32.1	25.6	19.1
GDC-10SGO	45.8	36.8	32.5	24.2
GDC-15SGO	44.9	34.6	24.4	15.6

In the temperature range of 400-800°C, it was observed that total conductivity of composite electrolyte was higher than pure GDC electrolyte material. The total conductivity at 800°C for GDC15 and GDC-15SGO was 38.49 mS cm^{-1} and 45 $mScm^{-1}$ respectively. Hence it may add that contribution of prtonic conduction in the composite electrolyte has been increased by adding SGO phase. GDC-SGO composite electrolyte exhibits ionic as well as protonic conduction in the temperature range of 400-800°C. Total conductivity of GDC-10SGO was higher than GDC15 in the intermediate temperature range.

Nyquist plot comparison for GDC15, GDC-10SGO and GDC-15SGO is shown in the Fig. 5. The impedance offered by pure (GDC15) and composite electrolytes was comparable at 650 °C.

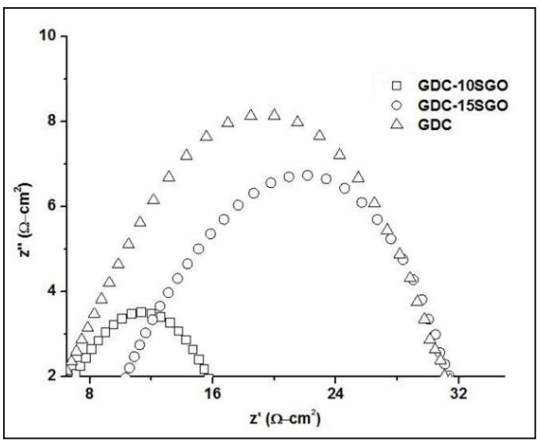

Fig. 5: Nyquist plot comparison for GDC15, GDC-10SGO and GDC-15SGO at 650 °C

Fig. 6 shows the impedance spectra offered by GDC, GDC-10SGO and GDC-15SGO composite electrolyte materials at 800 °C. It can reveal by the graph and impedance result that the impedance offered by the GDC-10SGO is lesser than GDC-15SGO.

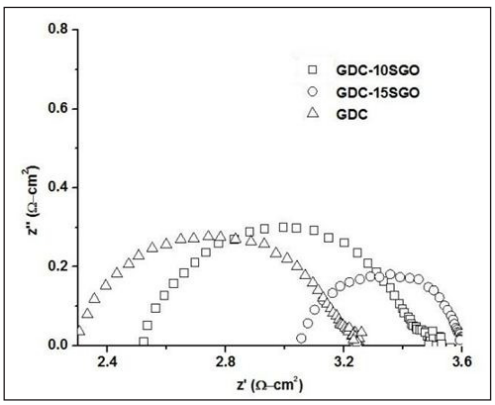

Fig. 6: Nyquist plot comparison for GDC, GDC-10SGO and GDC-15SGO at 800 °C

Activation energy (E_a) offered by the pure GDC15 and composite electrolyte materials were calculated using the Arrhenius equation in the temperature range of 450-800°C. The activation energy and conductivity comparison plot is shown in the Fig. 7 for GDC15, GDC-10SGO and GDC-15SGO in the temperature range of 450-800 °C.

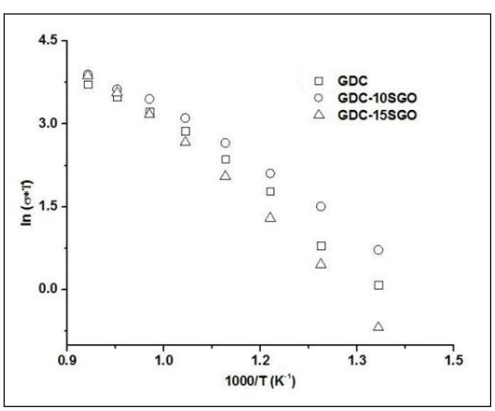

Fig. 7: Activation energy comparison for GDC15, GDC-10SGO and GDC-15SGO composite electrolyte materials in the temperature range of 450-800 °C.

The evaluated activation energy for the GDC15, GDC-10SGO and GDC-15SGO were 0.77, 0.61 and 0.86eV respectively.

4. Conclusions

In the present investigation, the novel composite electrolyte material GDC-SGO at different Sr mol % doping was studied. The processing route for produced powder was novel glycine-nitrate method and there were no intermediate step between powder synthesis and sintering such as calicantion. Desired phases for pure and composite powders obtained right after combustion synthesis. The effects of sintering temperature and presence of different quantity of second phase in the form of SGO in the composite electrolyte material have been studied.

Total conductivity of GDC-10SGO and GDC-15SGO was comparable at intermediate temperature range of 600-800°C. GDC-10SGO based composite electrolyte exhibited higher total conductivity and lesser activation energy as compared to pure GDC electrolyte and Ba10CG ($Ba_{0.1}Ce_{0.85}Gd_{0.15}O_{3-\delta}$) composite electrolyte material at 650°C [15]. Nano size powders were obtained right after combustion synthesis process. With increase in Sr mol % in GDC attributed to the reduction of particle sizes for composite electrolyte. With high concentration of Sr in the composite electrolyte was the reason for higher conductivity value at intermediate temperature range and it was revealed that at intermediate temperature range, GDC-SGO composite electrolyte exhibit good protonic conductivity.

Acknowledgement

The authors wish to thank, Dr. J. Kolte of IIT, Bombay for XRD analysis and Dr. P. K. Patro of Powder Metallurgy Division, BARC for SEM analysis.

References

[1] S. C. Singhal, "Solid oxide fuel cells for stationary, mobile, and military applications," Solid State Ionics, vol. 152–153, pp. 405–410, 2002.

[2] N. Laosiripojana, W. Wiyaratn, W. Kiatkittipong, A. Arpornwichanop, A. Soottitantawat, and S. Assabumrungrat, "Reviews on solid oxide fuel cell technology," Eng. J., vol. 13, no. 1, pp. 65–83, 2009.

[3] N. Q. Minh, "Solid oxide fuel cell technology - Features and applications," Solid State Ionics, vol. 174, no. 1–4, pp. 271–277, 2004.

[4] J. Huang, F. Xie, C. Wang, and Z. Mao, "Development of solid oxide fuel cell materials for intermediate-to-low temperature operation," Int. J. Hydrogen Energy, vol. 37, no. 1, pp. 877–883, 2012.

[5] K. Eguchi, T. Setoguchi, T. Inoue, and H. Arai, "Electrical properties of ceria-based oxides and their application to solid oxide fuel cells," Solid State Ionics, vol. 52, no. 1–3, pp. 165–172, 1992.

[6] N. Taniguchi, K. Hatoh, J. Niikura, T. Gamo, and H. Iwahara, "Proton conductive properties of gadolinium-doped barium cerates at high temperatures," Solid State Ionics, vol. 53–56, no. PART 2, pp. 998–1003, 1992.

[7] R. C. T. Slade and N. Singh, "Systematic examination of hydrogen ion conduction in rare-earth doped barium cerate ceramics," Solid State Ionics, vol. 46, no. 1–2, pp. 111–115, 1991.

[8] K. R. Reddy and K. Karan, "Sinterability, mechanical, microstructural, and electrical properties of gadolinium-doped ceria electrolyte for low-temperature solid oxide fuel cells," J. Electroceramics, vol. 15, no. 1, pp. 45–56, 2005.

[9] N. Bonanos, B. Ellis, K. S. Knight, and M. N. Mahmood, "Ionic conductivity of gadolinium-doped barium cerate perovskites," Solid State Ionics, vol. 35, no. 1–2, pp. 179–188, 1989.

[10] L. Malavasi, C. A. J. Fisher, and M. S. Islam, "Oxide-ion and proton conducting electrolyte materials for clean energy applications: structural and mechanistic features," Chem. Soc. Rev., vol. 39, no. 11, pp. 4370–4387, 2010.

[11] B. Li, S. Liu, X. Liu, S. Qi, J. Yu, H. Wang, and W. Su, "Electrical properties of SDC-BCY composite electrolytes for intermediate temperature solid oxide fuel cell," Int. J. Hydrogen Energy, vol. 39, no. 26, pp. 14376–14380, 2014.

[12] N. Bonanos, B. Ellis, and M. N. Mahmood, "Oxide ion conduction in ytterbium-doped strontium cerate," Solid State Ionics, vol. 28–30, no. PART 1, pp. 579–584, 1988.

[13] P. I. Dahl, R. Haugsrud, H. L. Lein, T. Grande, T. Norby, and M. A. Einarsrud, "Synthesis, densification and electrical properties of strontium cerate ceramics," J. Eur. Ceram. Soc., vol. 27, no. 16, pp. 4461–4471, 2007.

[14] J. H. Gu and L. He, "Preparation of Y-Doped Barium Cerate and Strontium Cerate Membranes," Key Eng. Mater., vol. 280–283, no. 2005, pp. 895–898, 2005.

[15] A. Venkatasubramanian, P. Gopalan, and T. R. S. Prasanna, "Synthesis and characterization of electrolytes based on BaO-CeO2-GdO1.5 system for Intermediate Temperature Solid Oxide Fuel Cells," Int. J. Hydrogen Energy, vol. 35, no. 10, pp. 4597–4605, 2010.

BANDGAP ENGINEERING IN NANOCRYSTALLINE SILICON POWDER BY MECHANICAL ALLOYING

Ankit Goyal and P R Soni

Department of Metallurgical and Materials Engineering, Malaviya National Institute of Technology, Jaipur, India

Abstract : In the present research, we have done bandgap engineering in nanocrystalline silicon powder using high energy ball milling. The solar grade (99.999% pure) nanocrystalline siliconpowder wasball milled in argon atmospherein an attrition mill for 1 h to 4 h to reduce crystallite size in it. The milled powders were then degassed, to remove entrapped gases ,in a vacuum oven at 200 ^{0}C in a vacuum of 10^{-2} torr for 1h. The as received and ball milled powders were then characterized to study their structural and optical properties.XRD spectra shows the cubic phase (FCC) particles with crystallite size in the nanometer range and decrease in crystallite size with increasing milling time. XRD results were confirmed by transmission electron microscopy. Raman spectroscopy shows sub-microcrystalline and nanocrystalline phases in the milled powder particles. Synchrotron XRF was used to determine purity of both the powders. UV-Vis spectroscopy was used to determine bandgap of the prepared powders using Taucformula from absorption spectra. The bandgap and the crystallite size in the silicon powder is found to be the function of milling hours. This establishes that high energy ball milling can tune bandgap in nanocrystalline silicon powder which have potential applications in the field of alternative energy sources.

Keywords: Nanocrystalline silicon,Powder, Mechanical alloying, Bandgap, Opto-electronics

Introduction

Bandgap in semiconductor materials is the most important property which is the cause of their extensive use in solar , LED and switching applications[1-3]. Although chemical routes are mostly used to synthesize semiconductor materialswith different bandgap [4-6], yet mechanical alloying is new upcoming technology to engineer the bandgap in semiconductor materials through size and composition variation[7-8]. Mechanical alloying provides a more uniform and easy method to engineer the bandgap of semiconductor materials which is a function of crystallite size though it is being used by very few scientists. CdZnS, CdSe, CdTeSe, CdPbS etc semiconductor materials have been synthesized by various scientists using mechanical alloying [9-11].

Silicon is an IV group element of the periodic table which has been attracting researchers for several years in the field of semiconductors (band gap 1.12eV) due to its large abundance. In recent years, nanotechnology allowed researchers to play with bandgap of silicon for opto-electronics and photovoltaic applications. However, the technology of mechanical alloying has still not been used to engineer the bandgap in the nanocrystalline silicon ,which can be used in the functionally graded solar cells.

In the present research work we have under taken the study of the effect of mechanical alloying on the bandgap in nano crystalline silicon powder to synthesize nanosilicon powder with different bandgaps.

Experimental

The solar grade nanocrystalline silicon powder of 5N purity(99.999%) was purchased from Hongwu International Group Ltd, China.The average particle size in the powder was <20 µm. The silicon powder was ball milled in argon atmosphere in an attrition mill for 1-4 h (1h, 2h, 3h, 4h) to decrease the crystallite size in it .Before milling , Impeller arms and inner surface of stainless steel vessel of the attrition mill were coated with tungsten carbide (WC) using thermal spraying technique. The balls used in milling was also of WC balls of 10mm dia were used as grinding media keeping ball to powder weight ratio of 10:1. The milled powders were then degassed, to remove entrapped gases , in an oven at 200^0C in a vacuum of 10^{-2} torr for 1h.

Synchrotron XRF beamline at 7 KeV was used to determine purity of as received and ball milled powders. XRD studies of these samples were carried out using P'analytical system diffractometer, using Cu Kα radiation (λ= 1.5406 Å) . Philips transmission electron microscope (TEM) was used to confirm the crystallite size in the as received and ball milled powders. Airix STR-500 Confocal Raman spectrophotometer, using solid state laser (532 nm) beam of 3 mW, was utilized for Raman analysis, to know the presence of crystalline and amorphous phases in powder particles. Perkin Elmer Lambda 750 UV-Vis spectrophotometer was used to obtain absorption spectra of silicon powders. Tauc formula was used to determine bandgap in the prepared powdersfrom the absorption spectra.

Results and Discussion

1. Structural Studies:

a) XRD :

Fig.1 shows X-ray diffraction (XRD) patterns of all the prepared samples. XRD patterns obtained were compared with a JCPDE standard database (ref 00-027-1402), which confirms the single phase silicon in all the cases. XRD patterns of silicon powders show crystalline phase with calculated h,k,l indices (1 1 1), (3 2 0), (2 2 0), (3 1 1), (4 0 0), (3 3 1) corresponding to the peak positions (2^0) at 28.576, 44.812, 47.427, 56.254, 69.370 and 76.523, respectively. XRD spectra shows FCC phase particles .

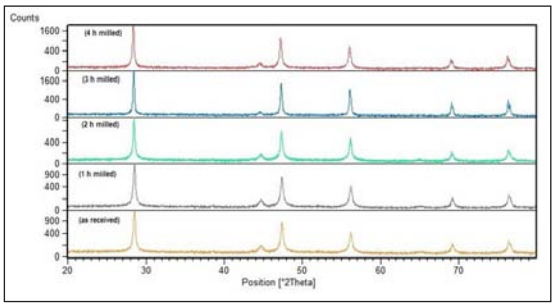

Fig.1 : XRD spectra of all the Si powder samples

The crystallite size was calculated using Deby-Scherrer's relationship [12] in all the powders and tabulated in the Table 1.

$$D = 0.94\,\lambda / B\cos\theta \qquad (1)$$

where, D is crystallite size, λ is wavelength of the X-rays used, B is full width at half maximum of the peak, and θ is corresponding Bragg's angle. Crystallite size in all the samples is in the nanometer range with the decreasing crystallite size with increase in the milling hours .

Decrease in crystallite size with the increase in the ball milling hours can be understood by the formation of shear bands , consisting of a dense network of dislocations, in the Si particles during the high energy milling . At certain dislocation density, due to thermoplastic instability, crystal disintegrates into the subgrains [13]. However, once an entirely nanocrystalline structure is achieved, the deformation becomes increasingly difficult as the nanocrystalline grains are

nearly dislocation free which requires very high stresses.

Table 1: Crystallite size with corresponding bandgap

S. No	Silicon powder	Crystallite size by Debye-Scherrer relationship (nm)	Crystallite size measured by TEM (nm)	Bandgap (eV)
1	As received	91	96	1.25
2	1 h milled	87	88	1.31
3	2 h milled	76	74	1.37
4	3 h milled	74	71	1.40
5	4 h milled	68	65	1.53

b) TEM:

Fig. 2 shows TEM images of all the prepared powder samples. Crystallite size measured by TEM using imageJ software was well in coherence with the results of XRD which confirms nano-crystalline silicon and reduction of crystallite size as a function of ball milling.

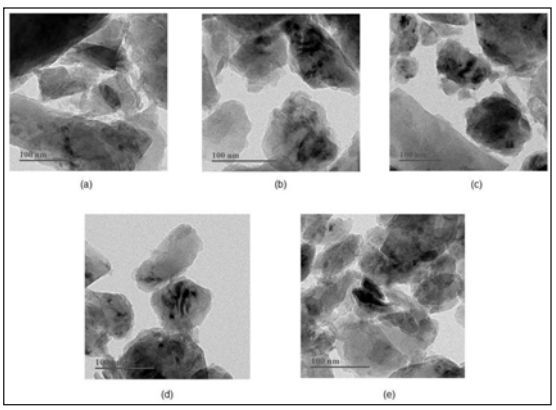

Fig 2: Transmission electron micrographs of a) as received b) 1 h milled c) 2 h milled d) 3 h milled e) 4 h milled Si powders

The grains and grain boundaries can be seen easily in all the micrographs. The micrographs of milled powders show micro plastic deformed particles with superimposed crystallites and overlapping grain boundaries because, in brittle materials, upon impact the respective powder particles wouldpenetrate the surface of an adjacent particle. The surface deformation could also be aided by the presence of preferentially active surface dislocation sources. With decreased critical shear stress for dislocation generation at the surface and enhanced mobility provided by somewhat elevated localtemperature [13] due to inter particle friction,could have lead to the diffusion bonding among the nanocrystallites.

c) Micro-Raman Spectroscopy

Fig.3 shows Raman spectra of the as received and ball milled silicon powder . The Raman spectra of 4 h milled powder shows an asymmetric peak so Gaussian deconvulation, using Levenberg–Marquardt algorithm [14], was done to know the peaks present as shown in Fig. 3 (b).

The Raman crystallinity is calculated as Xc given by [15]

$$Xc = (I_{510} + I_{520})/(I_{480} + I_{510} + I_{520}) \quad (2)$$

$$X_{amorphous} = 1 \square Xc \quad (3)$$

where I_i denotes an integrated intensity at i cm^{01}, and $(I_{510} + I_{520})$ is equal to the volume fraction of the crystalline phase.Raman spectroscopy confirms the crystalline nature of powders with no amorphous phase presence in the milled powders.

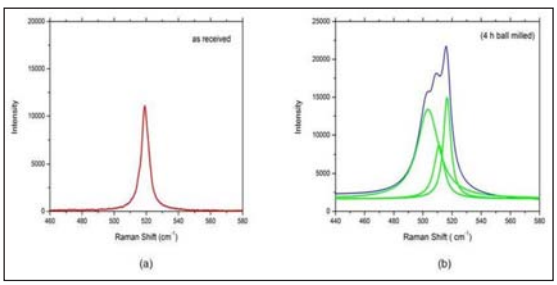

Fig. 3: Raman spectra of a) as received and b) 4 h milled Si powders with Gaussian deconvulation

2. Purity Confirmation

Synchrotron X-ray fluorescence (XRF) at 7 KeV energy was used to confirm the purity (to the level of ppm) in both as received and ball-milled silicon powders. It can be seen in Fig. 4 that ball milling didn't introduce any impurity in silicon powders making the technique reliable for use in the semiconductor research. The absence of impurity is the attribute of tungsten carbide coating on the impeller and inner surface of SS vessel of the attrition mill , and the use of tungsten carbide balls as grinding media which is harder material than silicon.

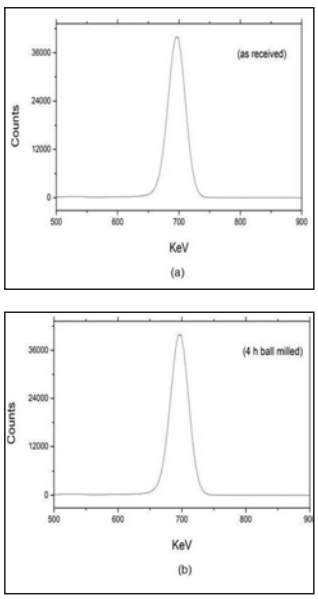

Fig. 4: XRF spectra of a) as received and b) 4 h milled Si powders

3. Band Gap Determination

UV-Vis spectroscopy was used to determine the bandgap in all the prepared powder samples using Tauc formula as in eq. 4 [16]. Absorption spectra of all the samples have been shown in the Fig. 5.

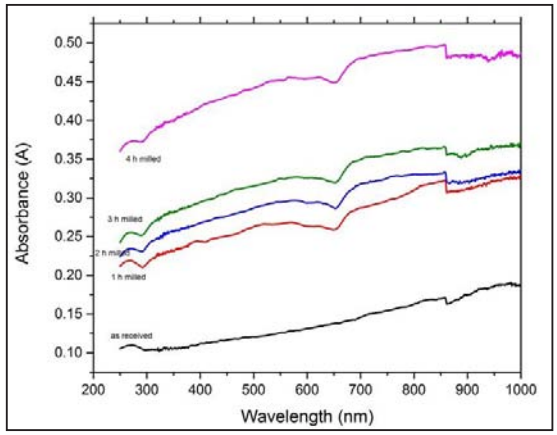

Fig.5 : Absorption spectra of all the Si powders

$$(\alpha h\square)^n = A\,(h\square - E_g) \quad (4)$$

Here, α is an absorption coefficient, Eg is bandgap and □ is frequency of incident is light. The value of n varies from ½ to 3 for different bandgap materials. In the case of silicon, which is an indirect bandgap semiconductor, the value of n is ½ [17].

The Tauc plots for all the powder samples are shown in Fig. 6. The bandgap values obtained, by extrapolating the Tauc plot, for the samples are shown in the Table 1. A material can absorb only those photons which have energy higher than of its bandgap. So the wavelength lesser than 1000 nm, 946 nm, 905 nm, 885 nm and 805 nm can be absorbed by as received, 1 h milled, 2 h milled , 3 h milled and 4 h milled silicon powders, respectively. This group of wavelengths represents near-IR range in the solar spectrum, thus these bandgap engineered silicon powders may be more effective in absorptionof the same .

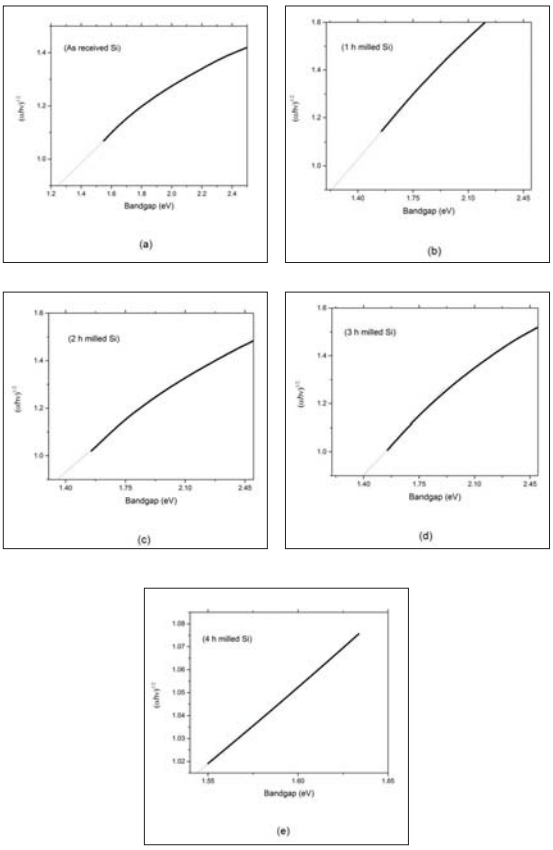

Fig. 6: Tauc plot of a) As received ; b) 1 h milled ; c) 2 h milled ; d) 3 h milled ; e) 4 h milled silicon powders

Fig. 7 shows variation in bandgap and nanocrystallite size with milling hours in Si powder samples .It can be seen that decrease in crystallite size and increase in bandgap are function of milling hours.. As the milling hours increases, the crystallite size decreases and the bandgap increases respectively, though non-linearly. It has already been studied and established that crystallite size and bandgap of material is inversely proportional to each other [17] .The non-linear decrease in crystallite size is due to the presence of tensile stresses generated during high energy ball milling and indirect nature of bandgap in silicon as phonon excitations are also involved in valence to conduction band transitions in indirect semiconductors.

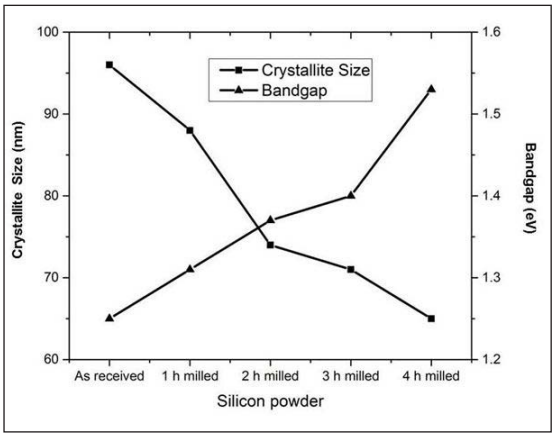

Fig.7 : Variation in bandgap and nanocrystallite size with milling hours in Si powder samples

Conclusions

High energy ball milling can be used to decrease the crystallite size with associated increase in bandgap in the nanocrystalline silicon powder. These silicon powders with tuned bandgaps may find potential applications in the field of alternative energy sources.

Acknowledgements

Authors are thankful to Beamline-16, Raja Ramanna Centre for Advanced Technology, Indore, India for providing the facility of synchrotron XRF for the studies.

References

1. B. G. Yacobi, Semiconductor Materials: An Introduction to Basic Principles, ISBN: 978-0-306-47361-6 (Print) 978-0-306-47942-7 (Online) (2003) Chapter 5

2. Sagadevan Suresh, Semiconductor Nanomaterials, Methods and Applications: A Review, Nanoscience and Nanotechnology, 2013; 3(3): 62-74 , doi:10.5923/j.nn.20130303.06

3. A. V. Shah, H. Schade,M. Vanecek, J. Meier, E. Vallat-Sauvain, N. Wyrsch, U. Kroll, C. Droz, J. Bailat, Thin-film silicon solar cell technology, Progress in Photovoltaics, Volume 12, Issue 2-3 2004, 113–142

4. Tito Trindade, Paul O'Brien , Nigel L. Pickett, Nanocrystalline Semiconductors: Synthesis, Properties, and Perspectives, Chem. Mater., 2001, 13 (11), 3843–3858

5. C. N. R. Rao, Chemical Routes to Nanocrystals, Nanowires and Nanotubes, Int. J. Nanosci., 04, 811 (2005). DOI: http://dx.doi.org/10.1142/S0219581X05003747

6. David J. Norris, Alexander L. Efros, Steven C. Erwin, Doped Nanocrystals, Science, 2008, Vol. 319, Issue 5871, 1776-1779

7. P. G. McCormick, T. Tsuzuki, J. S. Robinson, J. Ding, Nanopowders Synthesized by Mechanochemical Processing, Advanced Materials, Volume 13, Issue 12-13, 2001, 1008–1010

8. J.L. Guimarães, M. Abbate, S.B. Betim, M.C.M. Alves, Preparation and characterization of TiO2 and V2O5 nanoparticles produced by ball-milling, Journal of Alloys and Compounds Volume 352, Issues 1–2, 2003, 16–20

9. Qi Zhang,1 Huihui Zhang,1 Limin Liu,1 Shaohua Li,2 James B. Murowchick,2 Clarissa Wisner,3 Nickolas Leventis,3 Zhonghua Peng,2,* and Guolong Tan1, Preparation of Ternary Cd1-xZnxS Nanocrystals with Tunable Ultraviolet Absorption by Mechanical Alloying, Electron. Mater. Lett., Vol. 11, No. 2 (2015), 187-192.

10. G. L. Tan, R. H. Liu,Preparation of pure CdSe nanocrystals through mechanical alloying,Journal of Nanoparticle Research, Volume 12, Issue 2,(2010) 605–614

11. Guo-Long Tan1, Limin Liu1, and WeibingWu,Mid-IR bandgap engineering of CdxPb1−xS nanocrystals by mechanochemical reaction, AIP Advances 4, 067107 (2014); doi: 10.1063/1.4881878

12. Ankit Goyal1*, Vinay Sharma1, Abhishek Sharma1, Ravi Agarwal1, K.B. Sharma1,2, S.L. Kothari1,3,synthesis, structural and optical study of cds nanoparticles doped with different concentration of cu,J. Nano- Electron. Phys. 3 (2011) No1, 254-259

13. P.R.Soni, Mechanical Alloying: Fundamentals and Applications, Cambridge International Science Publishing,(2000).

14. D.W. Marquardt,An Algorithm for Least-Squares Estimation of Nonlinear Parameters, J. Soc. Ind. Appl. Math. 11 (2) (1963) 431.

15. H.-S. Hwang, M.-G. Park, H. Ruh, H.-U. Yu, Bull.Investigations on Microcrystalline Silicon Films for Solar Cell Application, Korean Chem. Soc. 31 (2010) 2909–2912.

16. Fangda Yuan, Zhengcao Li*, Tianci Zhang, Wei Miao and Zhengjun Zhang,Enhanced light absorption of amorphous siliconthin film by substrate control and ion irradiation,Nanoscale Research Letters 2014, 9:173

17. R.E. Marotti, P. Giorgi, G. Machado, E.A. Dalchiele,Crystallite size dependence of band gap energy for electrodeposited ZnO grown at different temperatures,Solar Energy Materials and Solar CellsVolume 90, Issue 15, (2006), 2356–2361

FABRICATION OF THERMOELECTRIC GENERATOR FOR HIGH TEMPERATURE APPLICATION USING UNICOUPLES MADE FROM p-TYPE AND n-TYPE β-IRON DISILICIDE

Rohit Garbade[1], Vaishali Poddar[1], Narendra Dhokey[1], Sandeep Butee[1], Deep Prakash[2], Ram Purohit[2]

[1]Department of Metallurgy and Materials Science, College of Engineering, Pune, India
[2]Powder Metallurgy Division, Bhabha Atomic Research Centre, Navi Mumbai, India

Abstract : Thermoelectric materials, which convert heat into electrical energy, are the energy resources of the future. Amongst the thermoelectric materials, β-$FeSi_2$ is emerging as an alternative promising high temperature semiconductor useful for temperature from 600-900˚C. In the current work, elemental powders of electrolytic Iron (98.9% purity, 400mesh), Silicon (98.5% purity, 200mesh), Manganese (99.00% purity, for p– type semiconductor) or Cobalt (99.50% purity, for n– type semiconductor) have been mechanically alloyed in Attritor mill for 6 hours in argon atmosphere (400 rpm, SS 304 balls of 6mm diameter, BPR = 10:1). Agglomeration of the powder was observed. Attritor milled powder then was sieved under 75 micron sieve to get more fine powder for further process. Attritor milled powder was Hot press sintered (HPS) to make unicouples of p-type and n-type by optimizing temperature, pressure and holding period to get densified compact. Subsequent pendulum annealing at 800˚C for 12 hours in vacuum was done to get substantial amount of β-$FeSi_2$ phase formation. Phase transition during the process was investigated using XRD, SEM and EDS. These unicouples were then connected electrically in series and thermally in parallel by silver plating to make the Thermo-electric generator circuit. Voltage across the circuit was determined.

Keywords: Thermoelectric generator, β-Iron Disilicide, Hot press sintering

1.1 Introduction

The increasing interest in bulk semiconducting Iron Disilicide, β-$FeSi_2$ is due to its wide scope of applications like in thermoelectric generator, photovoltaic and optical fiber communications [1,2]. Iron Disilicide (β-$FeSi_2$) is one of the members of thermoelectric family which is having good thermoelectric conversion capability within 500 K -1200 K [3]. In this work, mechanical alloying was carried by Attritor milling (AM) in the atmosphere of Argon gas. Composition of iron and silicon system was taken according to Stoichiometry. For p type powder Mn was used as additive and for n type powder Co was used asadditive. The variation of these additives was also carried out to evaluate different properties. Fine grain size provide short diffusion path to enhance phase transformation and phase homogenization[4]. Then it was followed by hot press sintering (Model: TSN – 25/8, Make: KEJETHERM, Capacity: 25 KVA, Tonnage: 8 tons) (HPS) and unicouple of p type and n type were prepared. . In HPS, the phase homogenization advantage is carried one step ahead to the desired phase transformation by applying high temperature and high pressure simultaneously. It thus provides thermodynamic conditions (high temperature, high pressure) required for densification of sample during hot compaction itself. Optimization of process parameters (viz. time, temperature, pressure) in HPS to obtain maximum density was carried out. The hot pressed pellets were annealed in tubular furnace (Maximum Temperature: ~ 1100°C, Vacuum: 10-5 mbar) under vacuum. Further

by joining this unicouples a TEG circuit was prepared by selecting proper substrate material.

1.2 Experimental procedure

As received Si (98.5% purity, 200 mesh) was sieved to get the fine silicon powder. Then it was milled for 10 h in attritor milling to make it finer. Further elemental powders of iron (99.9% purity, 200 mesh) and milled silicon have been mechanically alloyed for 6 h by using milling route high-energy Attritor ball-mill (water cooled SS 304 vial, 400 rpm, 6mm Φ SS 304 balls, BPR= 10:1, Ar atmosphere).The stoichiometric composition for the various combination of powders is given in table 1 and 2. Following these tables variation in weight percent of powders was tried.

Table 1: Charge Calculation for p-type powder

Element	Atomic Weight	Atom fraction	Weight fraction	100 grams
Fe	56	0.3067	0.461	46.033
Mn	55	0.0267	0.039	3.931
Si	28	0.67	0.500	50.036
$Fe_{0.92}Mn_{0.08}Si_2$	111.92			100.000

Table 2: Charge Calculation for n-type powder

Element	Atomic Weight	Atom fraction	Weight fraction	100 grams
Fe	56	0.3167	0.474	47.436
Co	59	0.0167	0.026	2.630
Si	28	0.67	0.500	49.933
$Fe_{0.95}Co_{0.05}Si_2$	111.88			100.000

The agglomeration of Fe powder was observed after the milling, so the powder was sieved under the sieve size of 75 microns to get the agglomerated free fine powder.The milled powder was then hot pressed in HPSunder vacuum atmosphere. Graphite dies for unicouple were designed tojoin p type and n type powder during the hot press cycle itself. Variations in the parameters like Temperature, Pressure and Holding time were carried out to get the most densified unicouple. Around 90% of the theoretical density was observed for temperature 1100°C pressure 25 MPa and holding time 6 min. The unicouples were subsequently sintered at 800°C for nearly 6 h in vacuum of 10^{-5} mbar and furnace cooled to room temperature. They were again sintered at 800°C for nearly 6 h in vacuum of 10^{-5} mbar and furnace cooled to room temperature. The sintered samples were then characterized using XRD and SEM - EDS. The amount of β-$FeSi_2$ phase formation got enhanced due to the thermal cycling treatment. The degree of alloying and phase transformation during milling and sintering were investigated using X-ray diffraction (XRD) analysis which was carried out using Cu Kα radiation. Further, SEM and EDS were performed on the sintered samples to observe the microstructure and identify the phases formed.

Seebeck apparatus was setup to calculate the seebeck coefficient and thermal resistance for the materials. Copper rod was used as heating source; it was kept inside muffle furnace. Silver foil 1 was kept over the glass wool above the copper rod on which specimen was placed. On both ends of the sample silver paste was applied. Silver foil 2 was kept on upper surface of the sample. Refractory block was kept as an insulator above silver foil 2. Thermocouple 2 was inserted through this block to measure temperature of cold end. Thermocouple 1 was kept in contact with copper rod to measure temperature of hot end. Potential difference across hot end and cold end was measured. The readings were taken at an interval of 10°C. Voltage was measured for all these temperatures. As seen in fig.1, the sample was kept at the position slightly shifted away from the central heating zone of the furnace to have temperature difference across the thickness of the sample.

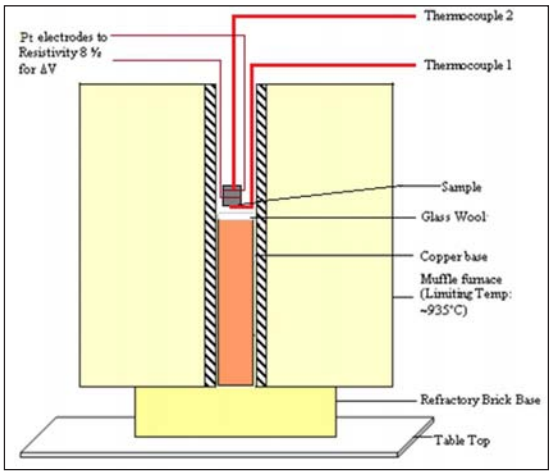

Fig. 1: Seebeck set up

After characterization the unicouples were arranged to make the thermoelectric generator (TEG). The substrate material used was synthanio sheets and alumina sheets for high temperature application. The unicouples were then arranged thermally in parallel and electrically in series in the synthanio sheets according to p type and n type arrangement. Silver paste and silver plate were used to join the unicouples to complete the circuit. For diffusing the silver paste with the unicouple the silver plate was coiled with the unicouple tightly in a clamp and was heated in a muffle furnace at 800°C for 1 h. Alumina sheets were kept on both sides i.e. top and bottom of the unicouple for more support and to act as hot end and cold end of the TEG.

Results and Discussions:

With reference to earlier studies [5], the milled powder was characterized and was observed that the particle size range squeezes from around 0.04 - 74µm to 0.04 - 30 µm. The XRD analysis showed peaks of □-FeSi after milling stage. Similarly, in that study DSC analysis was carried out in which shift in reaction temperatures to the lower values was observed compared to the equilibrium values[6].

The study of phase formation was carried by XRD analysis. Various additive variations were tried along with reference to the previous studies[7-10]. Both Hot pressed pellets (HPS) as well as sintered pellets (HT) were tested for p type and n type. The XRD analysis is shown in figures 2 and 3. Phase formationcan be seen from the XRD data. These results are in alignment with the SEM – EDS analysis. Agglomeration at few locations and tendency to attend lowestenergy configuration by reacting with intact particles might have resulted in phase formationduring milling. The pellets were hot pressed sintered and annealed at an optimized heat treatment cycle.

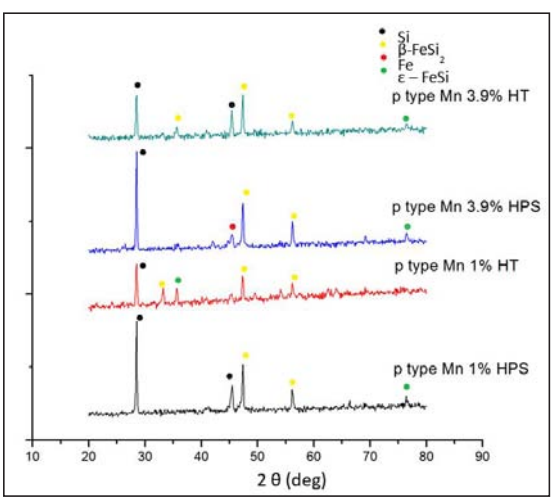

Fig.2: XRD analysis of p-type pellets (here % represent wt % of p type additive)

High intensity peak of Siwas observed in HPS pellets. Small peaks of β $FeSi_2$ was also observed due to the reactions α-Fe_2Si_5 + ε - FeS→ β-$FeSi_2$ and ε-FeSi+Si→ β-$FeSi_2$. Both the orthorhombic β-FeSi2 and cubic ε –FeSiphases can be observed,

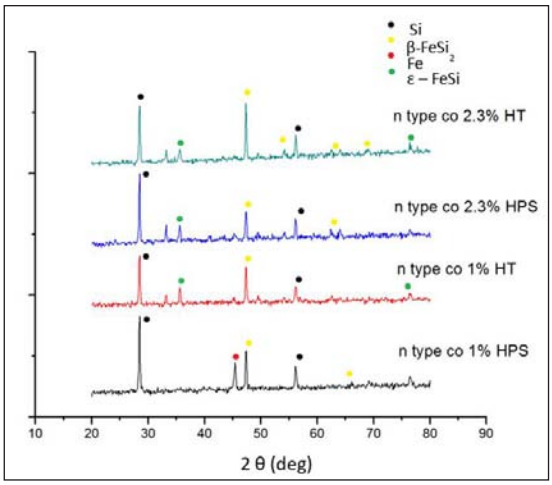

Fig.3: XRD analysis of n-type pellets (here % represent wt % of n type additive)

which suggest that α and ε phases are partially transformed to β phaseaccording reaction $\alpha\text{-}Fe_2Si_5 + \varepsilon\text{-}FeSi \rightarrow \beta\text{-}FeSi_2$. Above 986°C, metallic $\alpha\text{-}Fe_2Si_5$ and ε-FeSiphases are stable; hence those phases may have formed. The analysis was nearly same for p-typeand n-type pellets. The specimen were subjected to sintering at 800°C for 6 h under vacuum of around 10-5 mbar and it was observed that almost all ε – FeSi phase got utilized in β-phase formation. Though unreacted Si was still observed.

SEM – EDS:

Results from XRD reports were confirmed through SEM-EDS analysis. All the pellets with different additive variations were examined. Fig.4 shows microstructure of all the pellets.

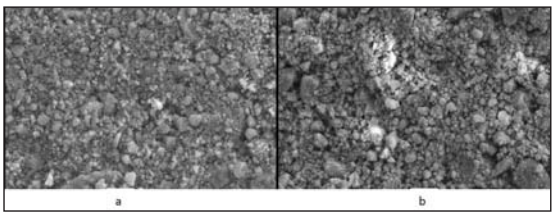

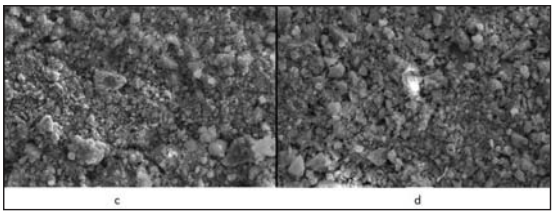

Fig.4 : SEM-EDS analysis of a). p-type 3.9wt %, b). n-type 2.3wt %, c). p-type 1wt %, d). n-type 1wt %

The EDS analysis of the powder showed the presence of $\beta\text{-}FeSi_2$ phase in the heat treated samples. This observation was also in alignment with the XRD data as discussed earlier.

Seebeck Coefficient

The Seebeck set up was designed so as to achieve ΔT not more than 10°C. The in house set up showed the temperature difference variation as in fig. 5. The analysis showed that the temperature difference was low. However, the temperature difference starts increasing beyond 975K. The temperature difference was found to be 19K at 1037K. Further, slow heating rate at higher temperature may be helpful to reduce the temperature difference.

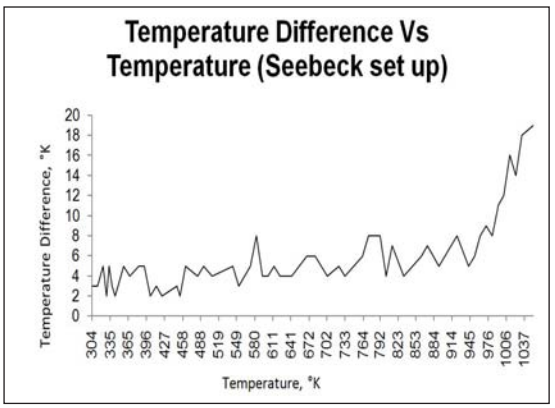

Fig. 5: Temperature difference across the sample with respect to the increasing temperature

Seebeck data for p-type sample is shown in fig. 6. It shows maximum value of 58.9 μV/°C at around 970K (697°C). For n-type sample (fig. 7) the maximum value was -33 μV/°C at around 873K (600°C).

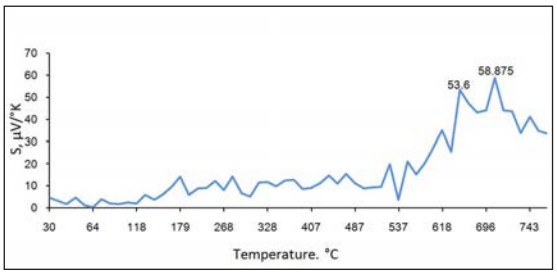

Fig. 6: Seebeck Coefficient of p-type sample with respect to temperature

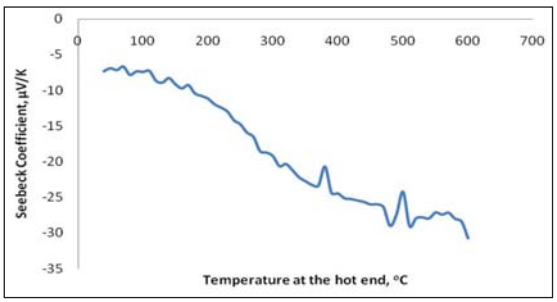

Fig. 7 : Seebeck Coefficient of n-type sample with respect to temperature

TEG Circuit

Fig.8 : TEG circuit made from unicouples (p and n type legs)

The circuit formation work is going on and the voltage related data will soon be included.

Conclusions:

- The HPS and HT pellets show β-$FeSi_2$ phase formation. For p-type 3.9 wt% Mn is recommended and for n-type 2.3 wt% Co is recommended on the basis of XRD results.
- β-$FeSi_2$ phase formation is achieved in less time (nearly 30 h) compared to other defined process routes[4, 11, 12].
- Seebeck coefficient for p-type pellet was around 58.9 μV/°C at around 970K (697°C). For n-type sample (fig. 7) the maximum value was -33 μV/°C at around 873K (600°C)

Acknowledgement:

This work was supported by the Bhabha Research in Nuclear Sciences (No. 2013/36/53-BRNS/2467), Navi Mumbai, Maharashtra, India.

References:

[1] HilaalAlam, Seeram Ramakrishna, "A review on the enhancement of figure of merit from bulk to nano-thermoelectric materials", Nano Energy, Vol. 2 (2013), 190-212.

[2] D.Z. Chi, "Semiconducting beta-phase $FeSi_2$ for light emitting diode applications: Recent developments, challenges, and solutions", Thin Solid Films, Vol. 537 (2013), 1–22

[3] Hao Wu, Bing Hu, Nianjun Tian, Qiguang Zheng, 'Preparation of β-$FeSi_2$ thermoelectric material by laser sintering', Materials Letters, Vol. 65 (2011), 2877-2879.

[4] C. Suryanarayana, "Mechanical alloying and milling", Progress in Materials Science, Vol. 46 (2001), 119-184.

[5] V. S. Poddar, N. B. Dhokey, R. R. Garbade, S. P. Butee, Deep Prakash, R. D. Purohit, "Rapid production of Iron Disilicide thermoelectric

material by Hot Press SinteringRoute", Materials Science in Semiconductor Processing, Under review.

[6] ASM Handbook, Alloy Phase Diagram, Vol. 3 (1992), 860-861.

[7] Isamu Yamauchi, Takashi Okarnoto, Hajime Ohata, ItsuoOhnaka, " β-phase transformation and thermoelectric power in $FeSi_2$ and Fe_2Si_5 based alloys containing small amounts of Cu", Journal of Alloys and Compounds, 260 (1997), 162-171.

[8] Mikio Ito, Hiroshi Nagai, Tomoyuki Tada, Shigeru Katsuyama and Kazuhiko Majima, "Effects of Oxide Dispersion on Thermoelectric Properties of β-$FeSi_2$", 20th International Conference on Thermoelectrics (2001)

[9] Mikio Ito, Hiroshi Nagai, Etsushioda, Shigeru Katsuyama, and Kazuhiko Majima, " Effects of P doping on the thermoelectric properties of β-$FeSi_2$", Journal of Appllied Physics, 2138 (2002), 90-91.

[10] Kiatgamolchai S, Parinyataramas J, Nilpairach S, Thueploy A, Wanichsampan J, Min G. "Thermoelectric properties of β-$fesi_2$ prepared by the mechanical alloying technique and pressureless sintering", Journal of Metallurgica, Vol.12, 2006, 119-127.

[11] Soon-Chul Ur, Il-Ho Kim, "Phase transformation and thermoelectric properties of n-type $Fe_{0.98}Co_{0.02}Si_2$ processed by mechanical alloying", Materials Letters 57 (2002), 543– 551.

[12]Qiu Yue, Hong-lie S., Yu-gang Y., Kai-hua W., "Fabrication and thermoelectric properties of β-$FeSi_2$ prepared by mechanical alloying", Transactions of Non-ferrous Metals Society of China 17(2007), 618-621.

SYNTHESIS AND CHARACTERISATION OF TITANIUM OXYCARBIDE BASED CERAMICS

Amit Sinha[1*], John T.S. Irvine[2] and P K Sinha[1]

[1]Powder Metallurgy Division, Materials Group, Bhabha Atomic Research Centre, Navi Mumbai, India
[2]School of Chemistry, University of St Andrews, North Haugh, St Andrews, UK

Abstract : Titanium oxycarbide is a solid solution of titanium monoxide (TiO) and titanium carbide (TiC) with general formula TiOxC1-x where oxygen and carbon occupy the octahedral interstitial sites in a fcc titanium lattice. In the present investigation, titanium oxycarbide has been used as a possible anode material for intermediate temperature solid oxide fuel cells (IT-SOFC). Titanium oxycarbide samples were prepared by reaction-sintering of TiO and TiC powders under vacuum at elevated temperatures. The phase purity and stability of oxycarbide powders have been studied under oxidizing as well as reducing environments. The compatibility of titanium oxycarbide with different intermediate-temperature electrolyte materials (YSZ, LSGM and GDC) was studied. The functional properties of oxycarbide based anode were investigated by studying the electrochemical performance of planar cells using GDC based electrolyte.

Keywords: Titanium oxycarbide, titanium monoxide, IT-SOFC, anode, XRD

1. Introduction

Solid Oxide Fuel cells (SOFCs) have emerged as one of the most promising technologies for the power source of future. The commercialization of SOFC is based on the development of economically competitive systems that in turn is governed by continuous innovation of materials development and optimisation of fabrication processes that lead to enhanced lifetime and reduced operating cost. The state-of-the art SOFC, till date, utilize rare-earth based ceramic materials for electrode and electrolyte systems. The commercialisation of SOFC would depend on the cost of rare-earth based raw materials. Hence, there is an urgent need to develop alternate materials that are free from rare-earths. The aim of the present investigation was, therefore, the development of rare-earth free anode material for IT-SOFC. The previous work in our laboratory indicated that titanium oxycarbide based material possesses a very high electronic conductivity. Hence titanium oxycarbide based system was selected in this study as a candidate rare-earth free electrode material for IT-SOFC [1,2].

Titanium oxycarbide attracts significant technological interests as it exhibits a combination of metallic and covalent/ionic character which is reflected by its physical properties like high electronic conductivity, high melting point, high hardness etc [1]. Titanium oxycarbide can be visualized as a solid solution of titanium carbide (TiC) and titanium monoxide (TiO) having the same face-centred cubic (FCC) rock-salt structure of TiC. In the present investigation, oxycarbide powders were prepared by solid state reaction of titanium carbide (TiC) and titanium monoxide (TiO). Titanium oxycarbide was envisaged as possible anode material for intermediate-temperature solid oxide fuel cell (IT-SOFC). The compatibility of titanium oxycarbide with intermediate-temperature electrolyte materials (GDC, LSGM and YSZ) was studied. The electrochemical properties of planar cells using employing titanium oxycarbide as anode material were also investigated.

2. Experimental

TiC (Alpha Aesar, 99.9% purity, average particle size: 2 µm) and TiO (Aldrich, 99.5 % purity; -325 mesh size) powders were mixed in a planetary ball mill (Fritsch Pulverisette 7) under acetone media using zirconia balls. The powder mixtures were dried under ambient conditions and subsequently compacted into green pellets of 13 mm diameter using a uniaxial hydraulic press at a pressure of 150 MPa. The green compacts were reaction-sintered under vacuum at a temperature of 1500 ^{0}C for 5 h.

The phase purity of the starting titanium carbide and monoxide as well as the reaction-sintered oxycarbide samples was studied through X-ray diffraction (XRD) using CuKα radiation (PANalytical X'accelerator). The lattice parameters of titanium oxycarbide powders were determined using Rietveld refinement of the XRD data. The morphology of the TiOxC1-x powders was studied through SEM as well as by transmission electron microscopy (TEM, JEOL JEM-2011). The stability of TiOxC1-x powders under oxidising environment was studied by carrying out thermo-gravimetric analysis (TGA) in a thermo-gravimetric analyser (NETZSCH TG 209) under flowing air from ambient temperature to 900 ^{o}C. The stability of oxycarbide samples under reducing environment was studied by subjecting the TiOxC1-x powders to a prolonged heat treatment under Ar+5%H2 environment at 900 ^{o}C for 18 h followed by analysis of phases of the heat treated samples through XRD. The formation mechanism of oxycarbide from the starting mixture of titanium carbide and monoxide was studied by heating the mixture under reducing environment at different temperatures.

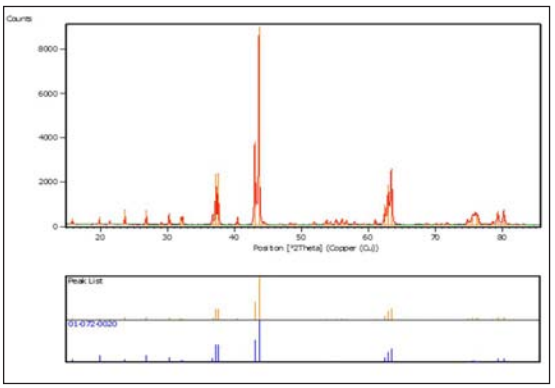

Fig. 1a: XRD pattern of titanium monoxide powder

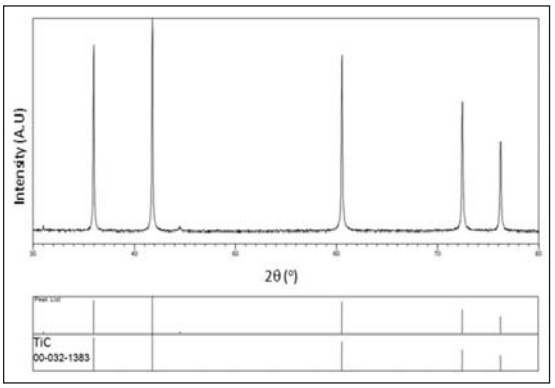

Fig. 1b: XRD pattern of titanium carbide powder

To study the interaction of titanium oxycarbide with common electrolyte materials for IT-SOFC ($Ce_{0.9}Gd_{0.1}O_{3-\delta}$ (GDC), Sr and Mg doped $LaGaO_3$ (LSGM) and 8 mol% yttria stabilized zirconia (8YSZ)], oxycarbide powders were mixed with electrolyte powders in equal weight ratio and compacted into green compacts of 14 mm diameter using a hydraulic press. The compacts were subjected to a heat-treatment at 900°C for 18 h under flowing 5% H_2 +Ar gas. After the heat treatment, the phase analyses of the mixtures were carried out through XRD.

The electrochemical performance of titanium oxycarbide as anode material was studied

in a planar fuel cell utilizing $Ce_{0.9}Gd_{0.1}O_{3-\delta}$ as electrolyte and $La_{0.8}Sr_{0.2}Co_{0.2}Fe_{0.8}O_{3-\delta}$ as cathode material The electrochemical characterization of the button fuel cell was conducted with humidified hydrogen (3 % H_2O) as fuel and ambient air as oxidant. The open circuit voltage of the cell was recorded in the temperature range of 400 – 800 °C and the current –voltage (I-V) measurements were made at different temperatures utilizing a SOLARTRON electrochemical test station. A constant fuel flow rate was used during the measurements. During the electrochemical characterisation, impedance spectra were recorded under open circuit voltage (OCV) conditions using a Solatron 1260 frequency response analyser coupled with a 1287 electrochemical interface within a frequency range of 1Mz to 0.1Hz.

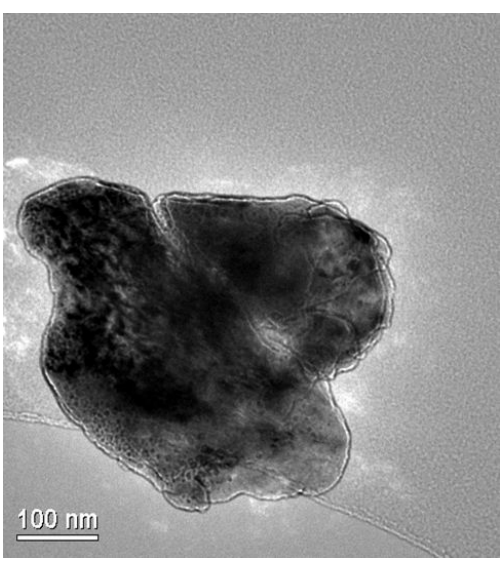

Fig. 2. TEM micrograph of TiO powder

3. Results and Discussion

The XRD pattern of titanium monoxide (TiO) is shown in Fig. 1a, which exhibits the monoclinic symmetry of the phase. Fig. 1b exhibits the XRD pattern of TiC powder which crystallizes in rack-salt (B1) symmetry. The particle morphology of TiO powder was studied through TEM. The TEM micrograph of TiO powder is shown in Fig. 2. The calculated average particle size of TiO powder was found to be 350 nm.

To study the phase transformation of TiO, the starting TiO powder was heated under reducing environment at different temperatures. It was observed that monoclinic polymorph of TiO transformed into cubic polymorph at 1000 °C. The XRD results of the TiO-TiC mixture after heat treatment of TiO-TiC mixture at different temperatures under reducing environment indicates that the reaction between TiO and TiC starts at a temperature more than 1200 °C to form titanium oxycarbide phase.

The XRD patterns of titanium oxycarbide powders with different carbon contents, exhibit phase pure titanium oxycarbide phase and can be indexed to cubic rocksalt structure in Fm-3m space group (No 225). The XRD patterns were refined through Rietveld analysis to determine the lattice parameters of the oxycarbide powders. Lattice parameters of titanium oxycarbide powders of this present investigation calculated after Rietveld refinement along with the lattice parameters of oxycarbide from JCPDF database. From the variation of lattice parameters of TiO_xC_{1-x} as a function of oxygen content, it can be observed that the introduction of oxygen in the lattice of carbon in TiC rocksalt structure leads to a gradual decrease in lattice parameter till almost half of carbon is being substituted by oxygen. The further substitution of carbon by oxygen leads to a sharp reduction of lattice parameter. The non-linear change in slope in the plot of lattice parameter vs. the oxygen content in TiO_xC_{1-x} may be attributed to the formation of point defects in TiO_xC_{1-x} in the form of vacancies both in metal and non-metal sub-lattices.

The TEM and HRTEM micrographs of $TiO_{0.2}C_{0.8}$ powder are shown in Figure 3a and 3b. The Fast Fourier Transform (FFT) analysis of the HRTEM image (Figure 3b inset) indicates the formation of cubic crystal lattice in $TiO_{0.2}C_{0.8}$. The TGA results of oxycarbide powders conducted under flowing air indicated that all the oxycarbide samples were stable in air up to 350 °C. The mode of non-isothermal oxidation of titanium oxy-carbide powders was found to depend on the carbon content in the powder while the onset temperature of oxidation has been found to be independent of carbon content.

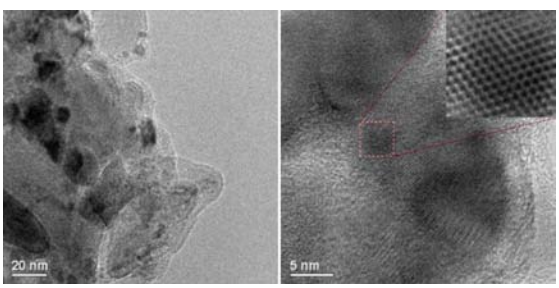

Fig. 3. TEM photomicrograph of $TiO_{0.2}C_{0.8}$ powder; (b) High resolution TEM (HRTEM) of $TiO_{0.2}C_{0.8}$ powder

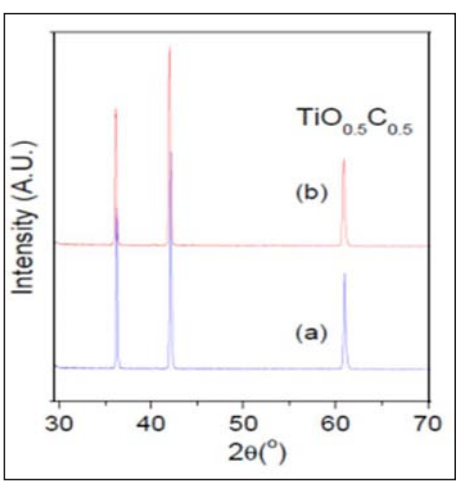

Fig. 4. XRD patterns of (a) as synthesized $TiO_{0.5}C_{0.5}$ powder and (b) the powder obtained after heat treatment at 900 °C for 18 h in Ar+5% H_2

Fig. 4 shows the XRD pattern of $TiO_{0.5}C_{0.5}$ powder heat treated at 900 °C for 18 h under Ar+5 %H_2 environment (Fig. 4b). The pattern is identical to the pattern of the starting powder (Fig. 4a) which suggests that the powder is stable under reducing environment at 900 °C.

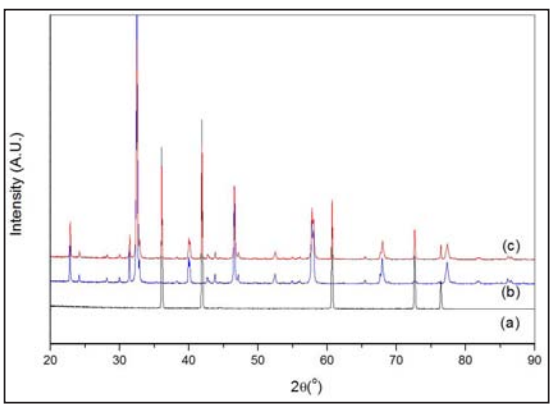

Fig. 5: XRD patterns of (a) as synthesised $TiO_{0.2}C_{0.8}$ powder; (b) LSGM powder; (c) $TiO_{0.2}C_{0.8}$ and LSGM powder mixture after heating at 900 °C for 18 h in 5% H_2

The interaction study of titanium oxycarbide with common electrolyte materials for IT-SOFC (GDC, LSGM and 8YSZ) indicated that there is no interaction of titanium oxycarbide with any of the electrolyte studied under reducing environment at 900°C. A representative XRD pattern is shown in Figure 5 for interaction study between oxycarbide and LSGM powder that shows that there is no interaction between the two powders at 900°C. The results of the electrochemical characterisation of oxycarbide based anode in GDC electrolyte supported SOFC indicated an appreciable peak power density of more than 130 mW/cm^2 at an operating temperature of 700°C. A further increase in power density was achieved by utilizing GDC thin film as an electrolyte that reduces the internal resistance originating from the electrolyte.

4. Conclusions

Titanium oxycarbide was studied as an alternative anode material for intermediate-temperature solid oxide fuel cell (IT-SOFC). Phase pure titanium oxycarbide powders were prepared by reaction-sintering of TiO and TiC powders under vacuum at a temperature of 1500°C. Titanium oxycarbide was found to be stable under reducing environment. The material is chemically compatible with the common electrolyte materials that exhibit better ionic conductivity in the intermediate temperature fuel cell applications. The electrochemical performance of titanium oxycarbide based anode in IT-SOFC single cell utilising GDC electrolyte indicates that oxycarbide is a novel rare earth free electrode for fuel cell application.

References

[1] Amit Sinha, D. N. Miller and J.T. S. Irvine, J. Mater. Chem. A, 4 (2016) 11117.

[2] D.N. Miller, A. K. Azad, H. Delpouve, L.Quazuguel, J. Zhou, Amit Sinha, P. Wormald and J.T. S. Irvine, J. Mater. Chem. A, 4 (2016) 5730.

THE EFFECT OF pH ON SYNTHESIS OF NANO-CRYSTALLINE MAGNESIUM ALUMINATE SPINEL POWDER BY THE Sol-Gel PROCESS

Bhavin Kumar[1, 2], C. Jariwala[1], H.N Panchal [2]

[1]Fusion Reactor Materials Development and Characterization Division. Institute for Plasma Research, GIDC Electronics. Estate, Gandhinagar, Gujarat, India
[2]Department of Metallurgical and Materials Engineering, Faculty of Technology and Engineering kalabhavan, M.S University of Baroda, Gujarat, India

Abstract : Magnesium aluminate ($MgAl_2O_4$) is of immense technological importance due to its mechanical strength at elevated temperature. Further, it possesses excellent thermal shock resistance, good optical, low coefficient of expansion value at elevated temperature, high resistance to chemical degradation. Due to these desirable properties, the $MgAl_2O_4$ is used as refractories, transparent armor, and nanofillers as reinforcement in ceramic pigments, humidity sensors and in development of RF windows. In order to obtain high purity, nano sizes, and non-agglomerated $MgAl_2O_4$ spinel powder the various processing techniques have been processed such as Precipitation route, Aerosol method, Citric-nitric route, Sol-Gel method, Spray drying, Freeze drying . The synthesis of $MgAl_2O_4$ nanopowder with Sol-gel method is adopted widely because of its ability to control the particle size and morphology through systematic monitoring of reaction parameters. In this present study, $MgAl_2O_4$ nanopowder is produced by Sol-Gel process and the effect of pH process parameters is attempted with various stirring time. The obtained $MgAl_2O_4$ nano powder was further calcined at high temperature in Muffle furnace and was subjected to X-Ray diffraction (XRD), Scanning electron microscope (SEM) for structural and morphological characterization. The optimized sol gel process produce the $MgAl_2O_4$ powder of varied crystalline size ranging from 34-104 nm.

Keywords: Sol-Gel, Nano crystalline, Magnesium Aluminate, Ceramic

Introduction:

Nano materials of $MgAl_2O_4$ with crystal sizes of about few nanometers have drawn significant among researchers around the world due to their unique properties. It has excellent thermal stability as it does not undergo any phase transformation up to its melting point. High structural stability at elevated temperature makes them a very promising material for use as refractory material. It is also known as a high performance ceramic material for structural applications because of its unique ability to develop high strength at both elevated and normal temperature. They also possess high strength, improved ductility/toughness, reduced elastic modulus. The extraordinary physical properties of nano materials are due to their relatively high volume fraction of grain boundaries. Nano materials have huge application potential is the field of sensors, structural ceramics, magnetic materials, fuel cells, refractories, transparent armor and nanofillers as reinforcement in ceramic pigments, humidity sensors and in RF windows, etc. [1, 2]. where conventional microcrystalline materials fail to achieve desired combination of physical properties.

The synthesis of $MgAl_2O_4$ with specific characteristics such as chemical homogeneity, high purity, low particle size and uniform size distribution depends considerably on preparation methods. As such, $MgAl_2O_4$ has been synthesized by various methods such as sol–gel,

solid state, spray drying, co-precipitation, and freeze-drying. However, most of these methods are either complex or expensive which lower preparation of the nano-sized materials in a large scale as compared to the combustion or sol–gel synthesis. Moreover, other disadvantages are the necessity of high temperature, inhomogeneity, and low surface area of the nano-sized products [3]. Therefore, In this present study, The sol-gel process has been used for the synthesis $MgAl_2O_4$ due to its unique ability to precisely control the particle size, size distribution, and morphology through systematic monitoring of reaction parameters for processing.

Experimental Procedure:

The $MgAl_2O_4$ nano particles were synthesized by sol gel method, followed by calcination of gel at various high temperatures. In this work, the precursor used were Aluminum Nitrate Nona-Hydrate [Al $(NO_3)_3$. $9H_2O$], Magnesium Nitrate Hexa-Hydrate [Mg $(NO_3)_2$. $6H_2O$] and Ammonium Hydroxide [NH_4OH]. The calculated amount of [Al $(NO_3)_3$. $9H_2O$], [Mg $(NO_3)_2$. $6H_2O$] was taken with molar ratio 2:1. This prepared solution was mixed slowly into the de-ionized water with continuous stirring for 1 hour. The mixture was stirred for 1 hour ensuring the uniform mixing to form a transparent solution. The Ammonium Hydroxide [NH_4OH] was slowly added drop wise under continuous stirring thereby varying the pH value of the solution from 1, 2 and 3. The solution with different pH values (1, 2 and 3) are continuous stirred for different time interval (24 hr, 48hr, 72hr, and 96hr). The obtained solution with different pH value and various stirring time were then taken in Petri dish and dried in hot air oven at 110°C for 48 hr and further heat treated at different high temperature (500°C, 1000°C, 1000°C) in a Muffle furnace at the rate of 0.6 0 C/ min. The calcined sample was then ground to pre and post heat treatment to produce fine powder. The process flow chart for the preparation of $MgAl_2O_4$ powder is shown in Fig. 1. The crystal size of calcined powder and phase formed after calcination were identified by using X-Ray diffraction (XRD). In addition, surface morphology of calcined powder was characterized by Scanning electron microscope (SEM)

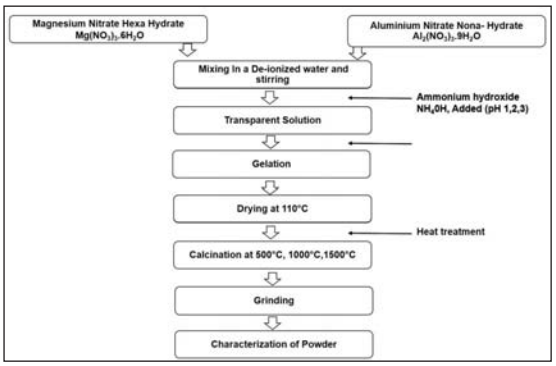

Fig. 1: Typical flowchart of the preparation of nano size Magnesium Aluminate

Result and Discussion:

X-Ray Diffraction (XRD) Analysis

The XRD patterns of samples processed at various temperatures are shown in Fig. 2 The structural analysis was done by XRD for obtained $MgAl_2O_4$ powder which shows the typical $MgAl_2O_4$ peaks confirmed the presence of $MgAl_2O_4$ phase in a powder. The powder processed at 500°C shows very low intensity and broad peaks due to amorphous like nature of obtained powder (Fig. 2 A(a)). Whereas, an increase in heat treatment temperature from 500°C to 1500°C show an enhancement of peak intensity, narrow and sharp peak were observe which suggest the crystallization of $MgAl_2O_4$ powder (Fig. 2 (b) and (c)).

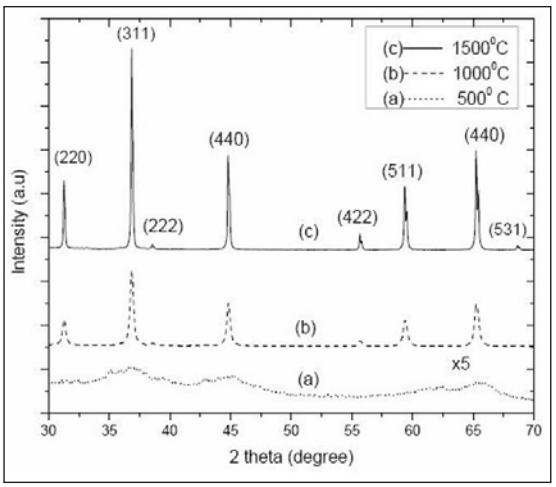

Fig. 2: XRD of $MgAl_2O_4$ powder processed at (a) 500°C (Data amplified with factor of 5), (b) 1000°C, (c) 1500°C and (B) The crystalline size as a function of pH and stirring time

The crystalline size of the synthesized powder was calculated by Debye-Scherer formula for the three pH value powders (Fig. 3). The crystalline size was found to be varying in the range of 34-104 nm for the different pH values 1, 2 and 3 is obtained. The graph shows the increase in the crystalline size value with increase pH value

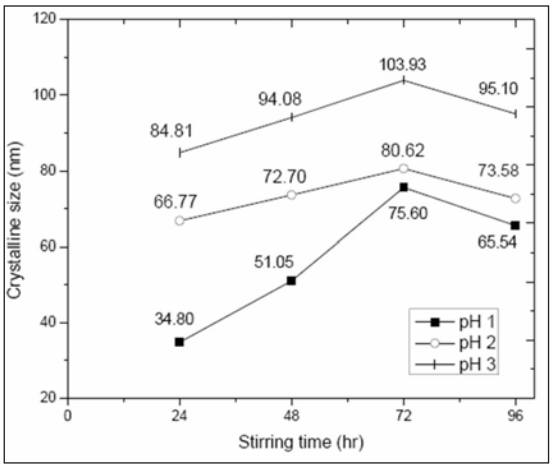

Fig. 3: The crystalline size as a function of pH and stirring time

from 1 to 3. Further increase in stirring time also increase crystalline size for all pH value upto 72 Hr. The further increase in stirring time (i.e. 96 Hr) leads to reduction of crystalline size for all pH value. This trend shows importance of stirring time with respect to pH value (1, 2, and 3).

Scanning Electron Microscope (SEM):

The surface morphology study obtained by SEM (Fig. 4 A) shows the agglomerate particle due to the high temperature given to the prepared powder

The (Fig. 4 B) shows the typical nano-sized powder structure with the uneven sized nanospherical balls

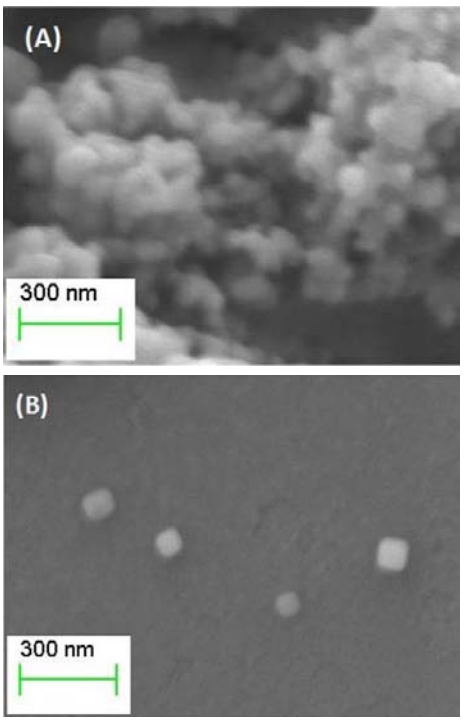

Fig. 4: Scanning electron micrographs of powder calcined at 1500° (A) Agglomerate particle (B) Uneven sized nanospherical balls

Conclusions:

- The crystalline nanosize $MgAl_2O_4$ spinel powder was successfully synthesized by Sol-Gel process. The pH process parameter was optimized to produce a powder with a crystalline size of 34 nm-105 which shows that the lowest pH value has the lowest crystalline size and favor for the formation of pure powder.
- The optimum pH with stirring time is taken for the formation of $MgAl_2O_4$ powder.
- The detail XRD measurement confirmed the crystalline nature and nano-sized of the processed powders. While SEM analysis shows the typical nano-sized particles along with agglomerated particles were present in $MgAl_2O_4$ spinel powder.

References:

1. R. Sarkar, Refractory application of magnesium aluminate spinel, Interceram. Refrect. Man. (2011), 11-14
2. F. Tavangarian and R. Emadi, Journal of Alloys and Compounds, 489(2010), 600-604
3. M. Kantinaskar and M. Chatterjee, Jouranl of the American Ceramic Society, 88(1), (2015), 38-44

INVESTIGATIONS OF POLING PARAMETERS ON PIEZOELECTRIC PROPERTIES OF LEAD LANTHANUM ZIRCONATE TITANATE CERAMICS

N.N. Wathore, C.M. Lonkar, S. Premkumar

Armament Research and Development Establishment, Pune, India

Abstract : Aim of the poling is to align maximum ferroelectric domains in one direction by optimizing poling parameters such as poling field, poling temperature and time to induce maximum piezoelectric properties in the ceramic. Effect of these parameters on Lead Lanthanum Zirconate Titanate (PLZT) ceramics was investigated through evaluation of piezoelectric charge coefficient (d_{33}). XRD analysis shows the polycrystalline nature of the sintered samples having co-existence of ferroelectric tetragonal (F_T) and ferroelectric rhombohedral (F_R) phases. SEM micrograph shows the compact microstructure of the samples. PLZT composition was synthesized by powder route and compacts were sintered at 1280°C for 1 hr. Curie temperature of 200°C was observed for this composition. Ferroelectric analysis shown square P-E hysteresis behavior. The inter-dependency among the poling parameters was observed and hence simultaneous variation in parameters was necessary to obtain maximum d_{33}. However, extent of poling was observed to be highly influenced by temperature compared to poling field and time. At optimized poling temperature of 100°C comparatively lesser poling filed and time were required to obtain maximum value of d_{33}. Piezoelectric coefficient of 453 x 10^{-12} C/N was obtained at poling field and temperature of 1.5 kV/mm and 100°C applied for 15 minutes.

Key word: Poling, PLZT, piezoelectric charge coefficient (d_{33}), ferroelectric domains

Introduction

Piezoelectric ceramics in as sintered condition does not posses piezoelectric properties due to random orientation of ferroelectric domains. Application of poling field causes domain reorientation in the applied field direction [1-3].The 180° domain get switched along the poling field easily but switching of non-180° domains, only with poling field, is difficult [4] and requires the simultaneous assistance of temperature and time to maximize the effect of poling [5]. Earlier researchers tried to optimize the poling parameters for different ceramic compositions and observed that the values of the poling parameters depend upon the ceramic composition [6]. Hence, detailed understanding on effect of poling parameters and their inter-dependency in domain switching mechanism and hence its influence on piezoelectric properties is necessary. Kounga et.al. studied the effect of fields and temperatures on piezoelectric properties of $Pb_{0.99}(Zr_{.045}Ti_{0.47}(Ni_{0.33}Sb_{0.67})_{0.08})O_3$ ceramic composition. They switched off the heating and reduced the oil bath temperature to room temperature, naturally, once the desired field was reached [7]. They reported the threshold field of 150 V/mm below which complete poling is not possible for any value of the temperature. Some researchers reported the effect of poling temperature and interaction between other poling parameters, particularly, on dielectric constant [8,9], remanant polarization [10] and displacement of actuator in shear mode [11]. [Sayer et. al.] studied the effect of poling parameters on piezoelectric coupling coefficient (k_p) of PZT system. They noticed the ease of domain reorientation with temperature and

poling field and hence takes lesser time to reach the saturation indicated by the dependence of k_p values [12]. Batal et.al. investigated effect of poling parameters on dielectric properties measured at various frequencies [13]. Above studies were aimed to investigate the effect of field or temperature on dielectric constant and hysteric behavior. To have a clear understanding of inter-dependency of all the three poling parameters: poling field, poling temperature and poling time, simultaneously on piezoelectric charge coefficient (d_{33}) is indispensible which has not been carried out so far, to the knowledge of the authors.

Present article discusses systematically, in detail, the simultaneous effect of poling field, temperature and time on d_{33} of $Pb_{0.94}La_{0.04}(Zr_{0.52}Ti_{0.48})O_3$ ceramic system and their optimization for achieving maximum d_{33}. It also discusses about the possible correlation between poling parameters and their effects on d_{33}.

Experiment

The raw materials PbO, La_2O_3, ZrO_2 and TiO_2 with purity over 99 % were used in the powder form to synthesize $Pb_{(1-x)}La_{(2/3)x}(Zr_{0.52}Ti_{0.48})O_3$ with x = 0.06 (PLZT). The grinding and homogenization of the powders were performed in roller mill with zirconia grinding media for 24 hr with water medium.

Further it was calcined at 1000°C for 4 hr and wet milled. Samples in the form of discs were pressed by double acting hydraulic press (Make-GMT) at 110 Mpa and subsequently sintered at 1280 °C in lead rich atmosphere for 1 hr in a closed alumina crucible. Sintered discs of diameter 25mm were lapped to 1.2 mm and further silver electrodes were applied on flat surfaces. Poling was carried between 0.5 -2.5 kV/mm poling field, using high field DC power supply (Make- Glassman) and heated in silicon oil bath between 60°C to120°C for 15 to 60 min. Poled samples were evaluated at 100 Hz for piezoelectric constant (d33) using Piezo d_{33} meter (Berlincourt-Model CPDT-3300). Samples were analyzed for phase formations using X-Ray Diffractometer, D8 Advance (Make-Bruker AXS GmbH). Microstructure analysis was carried out using FESEM, Quanta 2000 (Make-Carl Zeiss). Phase transition behavior was investigated through temperature dependence of dielectric constant, measured using LCR HiTESTER (HIOKI 3532 , Japan). Ferroelectric analysis was reported using TF 2000 analyzer.

Result and Discussion

Fig. 1 shows X ray diffraction pattern for sintered PLZT ceramics for 2θ position from 20-70° recorded by D8 Advance X-ray diffractrometer (Bruker AXS GmbH, Germany) using Cu Kα (λ=1.54Ǎ) radiation. Pattern shows polycrystalline nature having single perovskite phase indicated by the peaks indexed and particularly intense peak for (110). However, splitting in the peak intensity for triplet (200), (210) and (211) indicated the coexistence of ferroelectric tetragonal (F_T) and ferroelectric rhombohedral (F_R) phases [14].

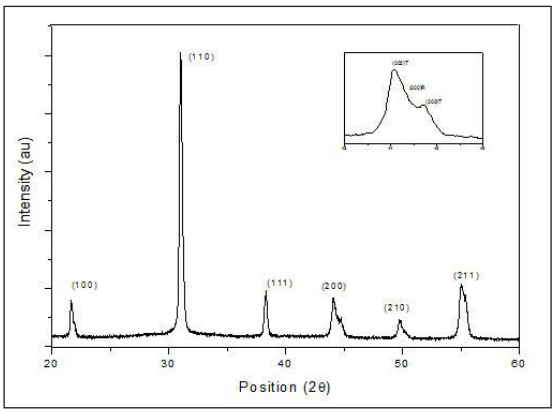

Fig. 1. XRD pattern of PLZT

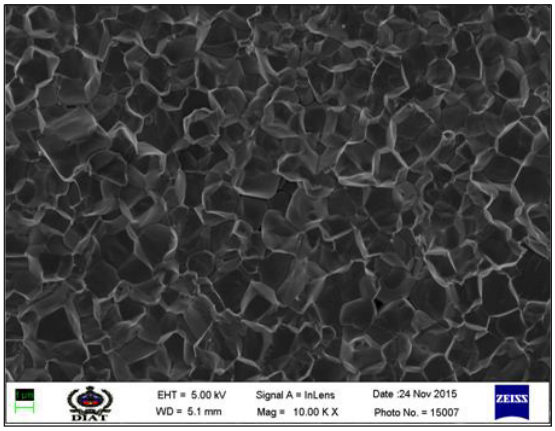

Fig. 2: SEM of PLZT ceramics sintered at 1280° C

Fig. 2 shows the surface morphology of fractured sintered sample recorded by Scanning Electron Microscope. Average grain size of about 1.5 µm was observed in this sintering condition. Compact microstructure with polygonal shaped grains accompanied by minimal porosity was observed indicating the complete grain growth at the chosen sintering temperature [15,16].

Fig. 3(a) shows temperature dependence of dielectric constant (K^T_3) and dielectric loss (tan δ) evaluated at 1 kHz from room temperature to 250° C. K^T_3 increases gradually with temperature, attains maximum value at ferroelectric to paraelectric phase transition temperature (Tc= 200 °C) and further decreases. Broader dielectric maximum was observed in the vicinity of phase transition temperature. This indicates the diffused phase transition which is due to the increased heterogeneity in the lattice arose because of random occupation of A site by La^{3+} and Pb^{2+} ions and B site by Zr^{4+} and Ti^{4+} ions which are having different ionic radii [17]. Around 90°C, an anamoly in the dielectric constant and tanδ designated by T_{RT} was observed which is attributed to rhombohedral to tetragonal phase transition [18,19].. Further rise in tanδ at higher temperature may due to the generation of space charge polarization in the ceramic materials [20] and rapid increase at high temperatures is because of increase in electrical conductivity of the material [21].

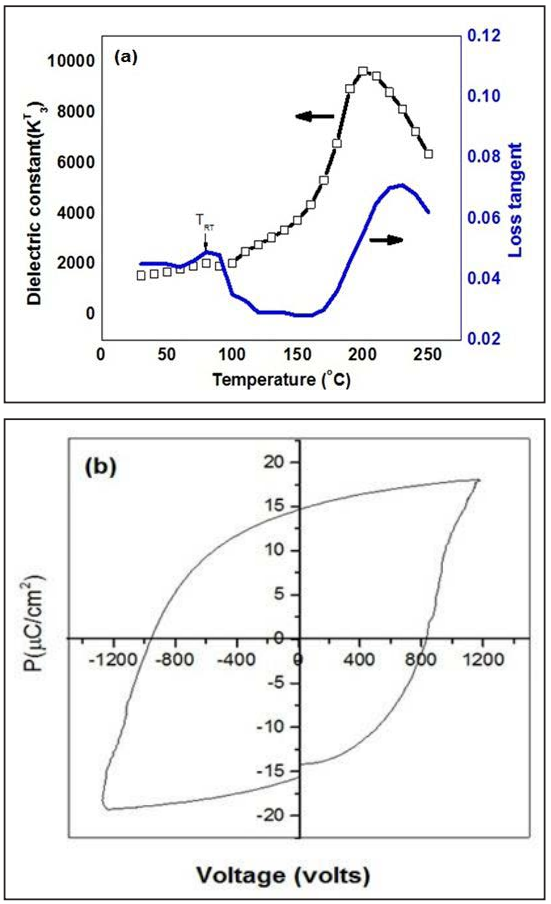

Fig. 3 : (a) Dielectric constant and dielectric loss as a function of temperature and (b) P-E hysteresis loop of PLZT

Fig. 3 (b) shows P-E hysteretic behavior of PLZT ceramics evaluated at room temperature.The coercive field E_c and remanent polarization P_r of 950V/mm and 14.7 µc/cm² were observed respectively. It shows the square hysteresis loop with comparatively lesser coercive field as

typically observed in soft ferroelectrics which indicates a domain switching can be achieved relatively at lower electric field.

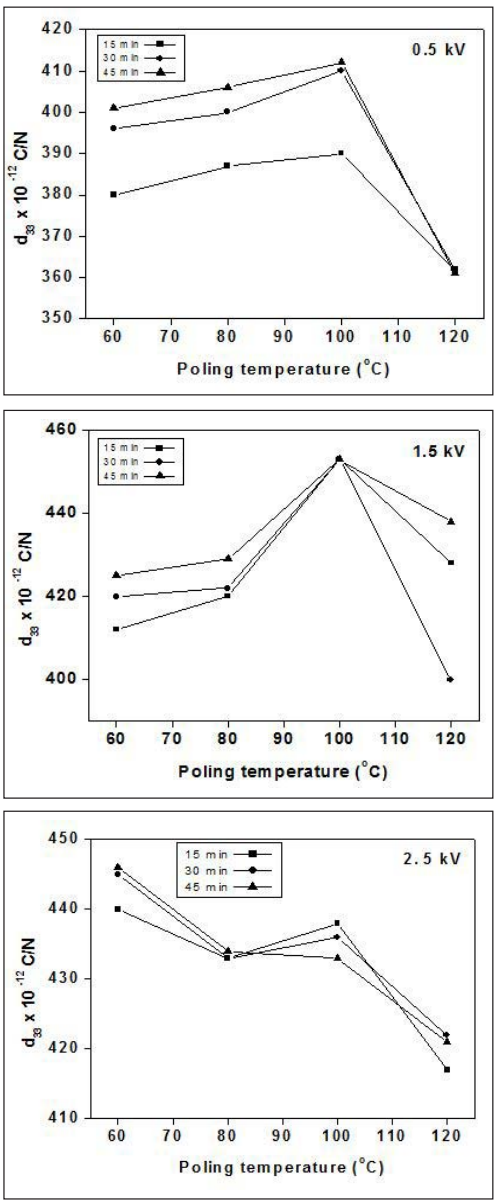

Fig. 4 Effect of poling temperature and poling time on d_{33} at a) 0.5 kV b) 1.5 kV c) 2.5 kV poling field

Fig. 4 (a-c) shows the effect of poling temperature and poling time on d33 at constant poling field applied between 0.5 kV/mm to 2.5 kV/mm. For poling field of 0.5 kV/mm (Fig. 4a) and 1.5 kV/mm (Fig. 4b), value of d_{33} increased gradually till 100°C and further decreased sharply. Rise in d_{33} with the temperature is attributed to the de-pinning of domains which leads to increased domain mobility [22] thereby easily aligning them along the poling field. The domains remains approximately in locked condition even after removal of field, thereby inducing permanent polarization in the material, since PZT materials facilitate essential permanent dimensional changes [23,24]. Such effect can be attained till the optimum value of temperature and beyond that conductivity increases and minimizes the effect of poling field [25]. As shown in Fig. 5c, for higher poling field of 2.5 kV/mm, d_{33} reached to 434 x 10 -12 C/N at lower temperature of 60 °C and further decreases as the temperature increases. In general, the alignment of domain with the poling field took place favorably till it reaches the optimum value which resulted in improved d_{33}. Further effect of the poling field is arrested because of shielding by space charges which are accumulated near the electrodes and increased conductivity [26]. The highest value of d_{33} of 453 x 10^{-12} C/N was observed at poling field of 1.5 kV/mm and temperature of 100°C indicating a suitable poling parameters for this composition. The optimized poling field for PLZT ceramics is about two times that of Ec as shown in Fig. 3(b) [27]. Moreover, the maximum piezoelectric properties appear near rhombohedral to tetragonal phase transition temperature was observed as shown in Fig. 3(a). Although, the effect of poling field and temperature was observed to be predominant till optimum values i.e. 1.5 kV and 100°C (Fig. 4a &b), poling time played vital crossing these

values. Increase in poling time enhances the piezoelectric coefficient at lower electric fields whereas it decreases at higher field. As shown in Fig. 4(c), d_{33} values decreased gradually at extended poling time to 45 minutes. This is in accordance with the observations of Koval et. al. wherein they noticed degradation of properties at poling fields beyond the optimum value applied for larger times [28].

Conclusion

PLZT composition sintered at 1280°C shows the presence of F_T and F_R pervoskite phases with compact microstructure having polygonal grains. Curie temperature evaluated from temperature dependent dielectric behavior was 200°C and coercive field of 950 V/mm was observed from P-E hysteresis studies. Samples were poled at different parameters such as poling field between 0.5 to 2.5 kV/mm and poling temperature of 60°C to 120°C for 15 - 45 minutes of poling time to investigate their effects to induce maximum piezoelectric charge coefficient (d_{33}) in the ceramic. The inter-dependency among the poling parameters was noticed from d_{33} values obtained and hence it was concluded that simultaneous variation in parameters was necessary to obtain maximum d_{33}. The extent of dipole alignment during poling was observed to be highly influenced by temperature and poling field compared to poling time. Maximum piezoelectric coefficient of 453 x 10^{-12} C/N for this composition was achieved at optimum condition of poling temperature and electric field of 100°C and 1.5 kV/mm respectively with comparatively lesser poling time.

References:

1. E Subbarao, V. Shrikanth, W. Cao, L. Cross, Ferroelectrics 145, 271 (1993)
2. T. Kamel, H. With, Euro. Cer. Soc. 28(9), 1827 (2008)
3. S. Chu, T. Chen, I. Tsai, Mater. Lett. 58, 752 (2004)
4. J. Jones, B. Iverson, K. Bowman, Amer. Cer. Soc. 90(8), 2297 (2007).
5. T. Kamel, F.Kools, G. With, Euro. Cer. Soc. 27(6), 2471 (2007).
6. P. Pulpan, L. Rusin, J. Erhart, Jpn. Appl. Phy.47,7953(2008)
7. Kounga, T. Granzow, E. Aulbach, M. Hinterstin, J. Rodel, Appl. Phys. 104, 24116 (2008)
8. Y. Takahiro, K. Masako,S. Norikazu, Mater. Sci. : Mater. in Electr. 11, 425 (2000)
9. S. Eslinger, P. Neumeister, A. Schonecker, Cera. Sci. and Tech. 4 (4), 213 (2013)
10. M. Nicolai, S. Eblinger, A. Schonecker, Electroceramics 32(2),180 (2014)
11. C.Cheng, S.Chen, S. Young, Y. Su, Y. Lin, Sensor and Actuator A, 126, 386 (2006)
12. M. Sayer, B. Judd, K. Asal, E. Prasad, Can. Cer. Soc. 50, 23 (1981)
13. M. Batal, F. Sroujy, S. Orfali, Inter. J. of Advn. Res. in Physical Sci. 2(10), 19 (2015)
14. A. Boutarfaia, C. Boudaren, A. Mousser, S. E. Bouaoud, Cer. Inn. 21, 391-394 (1995)
15. M. Chen, X. Yao, L. Zhang, Ceram. Int. 28, 201–207 (2002)
16. C. M. Lonkar, D. K. Kharat, H. H. Kumar, S. Prasad, K. Balasubramanian, J. Mater. Sci. Mater. Electron, 24 (1), 411-417 (2013).
17. A. Kumar, S. K. Mishra, Adv. Mat. Lett. 5(8), 479-484 (2014).
18. Y. Yamashita, Y. Hosono, K. Harada, N. Yasuda, IEEE trans. ultrasonics, ferroelectrics, and frequency control, 49(2002), 184-192.
19. N. Vittayakorn, G. Rujijanagul, X. Tan, M. A. Marquardt, D. P. Cann, J. Appl. Phys. 96, 5103 (2004)
20. R. Dixit, Inter. J. of Emerg. Tech. And Adv. Engg. 4(3), 385 (2014)

21. R. Zachariasz, D. Bochenek, Euro. Phy, 88, 296 (2015).

22. T. Kamel, G. With, Euro. Cer. Soc. 28(9), 1827 (2008)

23. R. Tohra, S. Beeby, N. White, IEEE transaction on ultrosonic, ferroelectric and frequency control" 52 (2005) 3010-3016.

24. N. Wathore, C. Lonkar, S. Kolhe, H. Kumar, A. Singh, Trans. Of Pow. Meta. Assoc. Of India 39, 46 (2013)

25. V. Parvanova, M. Nadolisky, Bulg. J. Phy. 32, 45 (2005).

26. S. Ikegamy, I. Ueda. T. Nagata, Accoustic Soc. of Amer. 50(4) 1060 (1971)

27. A. Kumar, V. V. Prasad, K. C. Raju, A. R. James, Euro. Phys, J.B. 88, 287 (2015).

28. V. Koval, J. Briancin, Key Engg. Mate. 193(1), 41 (1997)